REOLOGIA EXTENSIONAL E MAGNETIZAÇÃO DE EMULSÕES DILUÍDAS DE FERROFLUIDOS

Arthur Leite Guilherme

Dissertação de Mestrado

Ciências Mecânicas

UNIVERSIDADE DE BRASÍLIA

Faculdade de Tecnologia

Departamento de Engenharia Mecânica

UNIVERSIDADE DE BRASÍLIA
FACULDADE DE TECNOLOGIA
DEPARTAMENTO DE ENGENHARIA MECÂNICA

REOLOGIA EXTENSIONAL E MAGNETIZAÇÃO DE EMULSÕES DILUÍDAS DE FERROFLUIDOS

Arthur Leite Guilherme

Orientador: Dr. Taygoara Felamingo de Oliveira (LEA/ENM/UnB)

DISSERTAÇÃO DE MESTRADO

PUBLICAÇÃO: ENM.DM - XXX.XXX

BRASÍLIA/DF: 14 de agosto de 2023

UNIVERSIDADE DE BRASÍLIA
FACULDADE DE TECNOLOGIA
DEPARTAMENTO DE ENGENHARIA MECÂNICA

Reologia extensional e magnetização de emulsões diluídas de ferrofluidos

Arthur Leite Guilherme

DISSERTAÇÃO DE MESTRADO SUBMETIDA AO DEPARTAMENTO DE ENGENHARIA MECÂNICA DA FACULDADE DE TECNOLOGIA DA UNIVERSIDADE DE BRASÍLIA COMO PARTE DOS REQUISITOS PARCIAIS PARA A OBTENÇÃO DO GRAU DE MESTRE EM CIÊNCIAS MECÂNICAS.

APROVADA POR:

Dr. Taygoara Felamingo de Oliveira (LEA/ENM/UnB)
(Orientador)

Dr. Mário Benjamim Baptista de Siqueira (LEA/ENM/UnB)
(Examinador Interno)

Dr. Yuri Dumaresq Sobral (MAT/IE/UNB)
(Examinador Interno)

Dr. Roney Leon Thompson (COPPE/UFRJ)
(Examinador Externo)

BRASÍLIA/DF, 31 DE AGOSTO DE 2023.

FICHA CATALOGRÁFICA

Guilherme, A. L.
Reologia extensional e magnetização de emulsões diluídas de ferrofluidos
[Distrito Federal] 2023.
xxiv, 69p. (ENM/FT/UnB), Mestre, Ciências Mecânicas, 2023.
Dissertação de Mestrado - Universidade de Brasília.
Faculdade de Tecnologia.
Departamento de Engenharia Mecânica.
Palavras-chave:
1. Gota de ferrofluido
2. Reologia extensional
3. Magnetização da emulsão
4. Ruptura de gota
I. ENM/FT/UnB
II. Título (série)

REFERÊNCIA BIBLIOGRÁFICA

Guilherme, A. L. (2023). Reologia extensional e magnetização de emulsões diluídas de ferrofluidos. Dissertação de Mestrado, Publicação ENM.DM - XXX.XXX, Departamento de Engenharia Mecânica, Universidade de Brasília, Brasília, Distrito Federal, xxiv, 69p.

CESSÃO DE DIREITOS

NOME DO AUTOR: Arthur Leite Guilherme.

TÍTULO DA DISSERTAÇÃO DE MESTRADO: Reologia extensional e magnetização de emulsões diluídas de ferrofluidos.

GRAU / ANO: MESTRE / 2023

Arthur Leite Guilherme

Dedico esta dissertação a todas as brasileiras e brasileiros.

Agradecimentos

Primeiramente, gostaria de agradecer a toda minha família, a qual construiu meu caráter e moldou quem eu sou. Em especial, agradeço à minha mãe, Márcia, que me alimentou com comida, amor e esperança. Mesmo nos momentos mais difíceis, me ofereceu conforto e coragem, que me possibilitaram chegar até aqui. À meu pai, José, que me ofereceu orientação e suporte durante toda minha jornada, de vida e acadêmica. À minha irmã e irmãos, Bárbara, Caio e David, os quais compartilho do prazer de pertencer à essa família. À meus avós, Maria Eufrásia e Luiz, que faleceu durante esse processo, pelo apoio incondicional ao longo de minha vida.

Agradeço à minha amada companheira, Clara, que esteve do meu lado em toda essa jornada, dia após dia, mesmo nos momentos em que precisamos estar à distância. Ouviu e ouve todos os meus medos e sonhos, e me retribue sempre com carinho, compreensão, apoio e amor. Tenho certeza de que faremos o possível e o impossível para realizarmos nossos sonhos juntos.

Agradeço a todos os meus amigos, que me ofereceram tempos de distração e lazer ao longo dessa jornada.

Agradeço a todos os profissionais de educação os quais cruzaram meu caminho e que me forneceram educação, conhecimento e cultura, desde os tempos de ensino fundamental ao ensino superior. À todos os professores do Departamento de Engenharia de Energias Renováveis da Universidade Federal da Paraíba, que participaram de minha graduação. Em especial, prof. Gilberto Moreira, que me deu a oportunidade de dar meus primeiros passos como cientista e me incentivou a sonhar alto.

Agradeço a todos os professores e profissionais do Departamento de Engenharia Mecânica da Universidade de Brasília, pelo conhecimento oferecido ao longo do mestrado. Em especial, agradeço ao prof. Taygoara, o qual tive a sorte de ter como meu orientador. Excelente como pesquisador e virtuoso como pessoa, Taygoara me orientou com excelência, presencial e remotamente, me possibilitou dar meus primeiros grandes passos como pesquisador e me inspira profundamente na carreira de professor e pesquisador.

Agradeço aos pesquisadores Lucas Cunha e Ivan Siqueira, colegas de meu grupo de pesquisa, e ao prof. Roney Thompson, que contribuíram ativamente para a excelência do estudo que trago nesse trabalho. Lucas foi também quem me introduziu com bastante

paciência, junto com prof. Taygoara, nessa área de pesquisa. Por isso, meus sinceros agradecimentos. Agradeço também ao pesquisador Rodrigo Abdo, membro do grupo, pela ajuda e orientação nessa jornada. Agradeço aos demais colegas do grupo de pesquisa e da universidade.

Agradeço ao Estado Federal Brasileiro pela possibilidade de obter estudos avançados de forma gratuita. Por fim, agradeço ao Conselho Nacional de Desenvolvimento Científico e Tecnológico (CNPq) pelo suporte financeiro concedido através da bolsa nº 131422/2021-9.

"Ela é magnética!
Ela é magnética!"
Adelita - Jorge Ben

Abstract

Title: Extensional rheology and magnetization of dilute ferrofluid emulsions
Author: Arthur Leite Guilherme
Supervisor: Dr. Taygoara Felamingo de Oliveira (LEA/ENM/UnB)
Graduate Program in Mechanical Sciences
Brasília, 2023

This work presents an investigation of the effects of external uniform magnetic fields on the rheology and magnetization of dilute ferrofluid emulsions subjected to planar extensional flows. To this end, we performed three-dimensional numerical simulations of a single superparamagnetic ferrofluid droplet suspended in a nonmagnetizable viscous fluid. This system corresponds to the emulsion's microstructural unit. The full incompressible Navier-Stokes equations for a biphase system with the addition of the magnetic term are solved using a projection method. The interface problem is addressed with the Level-Set method. We find that the droplet's configuration and magnetization depend on the external field intensity and direction. Macroscopically, the droplet contribution to the bulk stress state is anisotropic. The two extensional viscosities associated with the normal stresses of the emulsion either remain constant or increase with the field intensity; the only exception occurs when the field direction is perpendicular to the extension plane, in which the second extensional viscosity decreases. When the external field is not aligned with the flow main directions, the droplet tilts in the flow and the droplet magnetization points no longer in the external field direction. At the emulsion level, this results in internal torques that lead to a nonsymmetric stress tensor. In order to account for these unexpected shear components and fully characterize the extensional rheology, we introduce new extensional material functions such as shear and rotational viscosity coefficients. We also analyze the conditions for droplet breakup. We find that the external field either induces or prevents the breakup depending on the field direction. The subcritical deformations in the plane formed by the extension and field directions vary linearly with the critical extension rate, regardless of the field direction. Overall, this study provides new insights into applications for field-controlled smart materials and precise manipulation of ferrofluid droplets.

Keywords: Ferrofluid droplet; Extensional rheology; Emulsion magnetization; Droplet breakup

Resumo

Título: Reologia extensional e magnetização de emulsões diluídas de ferrofluidos
Autor: Arthur Leite Guilherme
Orientador: Dr. Taygoara Felamingo de Oliveira (LEA/ENM/UnB)
Programa de Pós Graduação em Ciências Mecânicas
Brasília, 31 de agosto de 2023

Este trabalho apresenta uma investigação dos efeitos de campos magnéticos uniformes na reologia e magnetização de emulsões diluídas de ferrofluido sujeitas a escoamentos extensional planar. Para isso, realizamos simulações numéricas tridimensionais de uma única gota de ferrofluido superparamagnético suspensa em um fluido viscoso não magnetizável. Este sistema corresponde à unidade microestrutural da emulsão. As equações de Navier-Stokes incompressíveis para um sistema bifásico, com a adição do termo magnético, são resolvidas usando um método de projeção. O problema de interface é tratado com o método Level-Set. Nós encontramos que a configuração e magnetização da gota dependem da intensidade e direção do campo externo. Macroscopicamente, a contribuição da gota para o estado de tensões da emulsão é anisotrópica. As duas viscosidades extensionais associadas às tensões normais da emulsão permanecem constantes ou aumentam com a intensidade do campo; a única exceção ocorre quando a direção do campo é perpendicular ao plano de extensão, em que a segunda viscosidade extensional diminui. Quando o campo externo não está alinhado com as direções principais do escoamento, a gota se inclina com relação ao escoamento e a magnetização da gota não aponta mais na direção do campo externo. Na escala da emulsão, isso resulta em torques internos que levam a um tensor de tensões não simétrico. Para levar em conta esses componentes de cisalhamento inesperados e caracterizar completamente a reologia extensional, nós introduzimos novas funções materiais extensionais, como os coeficientes de viscosidade de cisalhamento e de rotação. Nós também analisamos as condições para ruptura de gota. O campo externo induz ou impede a quebra da gota, dependendo da direção do campo. As deformações subcríticas no plano formado pelas direções de extensão e do campo varia linearmente com a taxa de extensão crítica, independentemente da direção do campo. No geral, este estudo fornece novas informações para aplicações de materiais inteligentes controlados por campos externos e manipulação precisa de gotas de ferrofluido.

Palavras-chaves: Gota de ferrofluido; Reologia extensional; Magnetização da emulsão; Ruptura de gota.

Summary

List of Figures

List of Tables

List of abbreviations and acronyms

ENO Essentialy nonoscillatory

LS Level-Set

MAC Marker-and-cell

SSP Strong stability preserving

VoF Volume-of-fluid

WENO Weighted essentialy nonoscillatory

List of Symbols

Latin letters

Symbol	*Description*
a, $\boldsymbol{A}$	Initial droplet radius, and Coefficient matrix
$a_{i,j,k}$, $b_{i,j,k}$,...	Linear coefficients
B, $\boldsymbol{B}$	Minor semi-axis length in the xy plane, and Magnetic induction field
$C_{i,j,k}$, Ca, Ca_c	Cell grid (i, j, k), Capillary number, Critical capillary number
Ca_s, Ca_p	Subcritical capillary number, Postcritical capillary number
Ca_{mag}, $Ca^{\star}_{mag}$	Magnetic capillary number, Magnetic capillary number for oblate shape
D, D_{ij}, $D_{s;ij}$	Deformation parameters. ij indicates the plane the deformation is evaluated. s subscript refers to the subcritical deformation.
$\boldsymbol{d}$, $\boldsymbol{D}$	Minimum distance to the interface, and Rate-of-strain tensor
e, $\hat{\boldsymbol{e}}_{\boldsymbol{x}}$, $\hat{\boldsymbol{e}}_{\boldsymbol{y}}$, $\hat{\boldsymbol{e}}_{\boldsymbol{z}}$	Width of control volume, and coordinate unit normal vectors (x, y, and z)
$F(\boldsymbol{x})$	Arbitrary function of space
$\boldsymbol{F}$, $\boldsymbol{F_c}$, $\boldsymbol{F_m}$	Sum of capillary and force terms, Capillary force, and Magnetic force
h, $\mathcal{H}(\phi)$, $\mathcal{H}_{\varepsilon}(\phi)$, H_{in}	grid spacing size, Heaviside function, Smoothed Heaviside function, and Magnetic field intensity inside the droplet
$\boldsymbol{h}$, $\boldsymbol{H}$, $\boldsymbol{H_0}$	RHS of the linear system, Magnetic field, and Applied magnetic field
$\boldsymbol{I}$	identity tensor
i, j, k, l, m, n	Subscript indices
k	Droplet demagnetizing factor
l_c, L, L_x, L_y, L_z	Characteristic length, Semi-major axis in the xy plane, and Semi-axis length in the x, y, and z direction

$\boldsymbol{m_d}$, $\boldsymbol{M}$, $\boldsymbol{M_d}$, $\langle \boldsymbol{M} \rangle$ Droplet magnetic moment, Magnetization field, Droplet magnetization, and Emulsion magnetization

$\hat{\boldsymbol{n}}$ Normal unit vector pointing outward the droplet surface

p, p_r Pressure field, and Polar radius

q Auxiliary pressure field

R, Re Coefficient of determination, and Reynolds number

S, S_x, S_y, S_z Surface region of integration, and Domain length in x, y, and z directions

$\boldsymbol{S^d}$ Symmetric part of the droplet stress

t, t_c Time, and Characteristic time

U_c, $\boldsymbol{u}$, $\boldsymbol{u}^\star$, $\boldsymbol{u}_\infty$ Characteristic velocity, Velocity field, Provisional velocity field, and Velocity at infinity (Boundary condition)

$u_{i,j}$, $v_{i,j}$ Generic vector field components in a two-dimensional problem

$u_{i,j,k}$, $v_{i,j,k}$, $w_{i,j,k}$ Discretized velocity components in the three-dimensional grid.

V, V_d Domain volume, and Volume of the droplet

$\boldsymbol{W^d}$ Skew-symmetric part of the droplet stress

x, y, z Coordinate directions

$\boldsymbol{x}$, $\boldsymbol{x_\Gamma}$ Position vector, and Nearest interface location

Greek letters

$\alpha_{l,m,n}$ Parameter in numerical volume integral

$\eta(\boldsymbol{x})$, $\eta_\varepsilon(\phi)$ Shear viscosity as a function of space, Smoothed shear viscosity

η, η_c, η_d, η_e, η_N Shear viscosity, Continuous-phase shear viscosity, Dispersed-phase shear viscosity, Emulsion shear viscosity, and Shear viscosity of a generic Newtonian fluid

η_{ext}, η_{cross} Planar extensional viscosity, and Second extensional viscosity

η_p, η_2 Droplet contribution to the planar extensional viscosity, and Droplet contribution to the second extensional viscosity

η_s, η_r Droplet contribution to the shear viscosity in the xy plane in extensional motion, and Droplet contribution to the rotational viscosity in the xy plane in extensional motion

θ, θ_{mag} Angle between semi-major axis L and the x direction, and Angle between the bulk emulsion magnetization and the applied magnetic field

κ Local mean curvature

λ Dispersed-to-continuous phase shear viscosity ratio

μ_0, μ_c, μ_d Permeability of free space, Permeability of the continuous phase, and Permeability of the dispersed phase

$\boldsymbol{\chi}$ Vorticity field

β Volume fraction of the dispersed phase

ρ Fluid density

σ, $\boldsymbol{\sigma}$, $\boldsymbol{\sigma^d}$ Interfacial tension between the phases, Stress tensor, Dispersed phase contribution to the stress/particle stress/droplet stress

$\boldsymbol{\sigma_t^d}$, $\boldsymbol{\sigma_c^d}$ Traction and compression terms of the droplet stress

τ, τ_{mag} Ficticious time of the reinitialization method, and Field-induced internal torque in the ferrofluid emulsion

ϕ, ϕ_0, Φ Level-Set/Signed distance function, Initial Leve-Set function for the reinitialization method, and Generic scalar field

χ Ferrofluid magnetic susceptibility

ψ, Ψ, $\Psi_\varepsilon(\phi)$ Magnetic potential field, Generic scalar or component of a vector, Smoothed version of a physical property

Ω, Ω^-, Ω^+ Domain whole region/Individual cell grid domain, Region inside the droplet, and Region outside the droplet

γ, Γ Parameter in the reinitialization method, and Interface region

$\delta(\phi)$, $\delta_\varepsilon(\phi)$, $\hat{\delta}(\boldsymbol{x})$ One-dimensional Delta function, Smoothed one-dimensional Delta function, and spatial Delta function

Δt, Δx, Δy, Δz Time step, and Grid spacing in x, y, and z direction

ΔCa, Δf Ca step, and Stress jump at the interface

ε Interface thicnkess. When as a subscript it indicates the variable is smoothed in the interface

$\dot{\varepsilon}$ Extensional-rate

ζ, $\zeta(\boldsymbol{x})$, $\zeta_\varepsilon(\phi)$ Dispersed-to-continuous phase permeability ratio, Nondimensional permeability, and Smoothed nondimensional permeability

Other symbols

∇	Nabla operator
$sgn(\phi)$	Sign function
$\mathcal{L}(\phi, \phi_0)$	Term in the reinitialization equation

1 Introduction

Fluids with tunable physical properties are a special class of smart materials. Ferrofluid emulsions are tunable fluids that respond actively to the application of magnetic fields, making them promising materials in a number of practical applications. In the following chapter, we give the reader the definitions and the literature background concerning studies on the mechanical and magnetic behavior of ferrofluid emulsions. At the end of the chapter, we enlighten the importance of the present work not only on the mechanical and magnetic description of such material but on the peculiar behavior observed in its stress state when it is subjected to external magnetic fields and planar extensional flows.

1.1 Ferrofluid emulsion: a smart material

Emulsions are microstructured liquids formed by stable mixtures of two immiscible viscous fluids. They are ubiquitous in nature and present in many industrial applications, such as the food industry, oil recovery, and pharmaceuticals (GRACE, 1982). Their microstructure is locally a biphase system where small droplets of one liquid (dispersed phase) are dispersed in the other (continuous phase). In general, they are formed by dispersion of oil-in-water (O/W), or water-in-oil (W/O). Macroscopically, the mixture can be regarded as a homogeneous liquid, provided that the length scale of the observation is much larger than the distance between the droplets. Fig. 1.1 shows a schematic representation of an emulsion for distinct length scales.

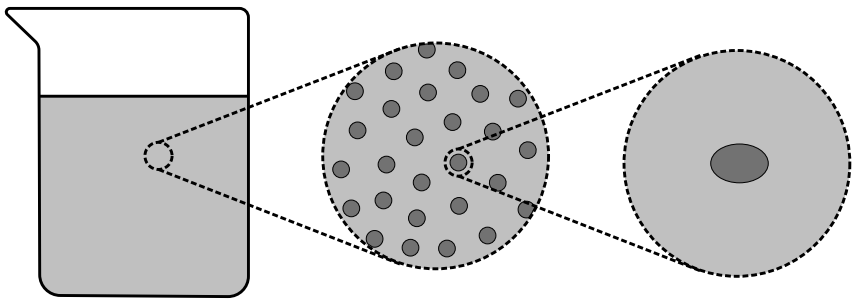

Figure 1.1 – Representation of an emulsion in different length scales. From a homogeneous material to the microstructure formed by the repetition of a single droplet-continuous phase system.

In terms of material properties, an emulsion presents non-Newtonian behavior,

such as strain-rate dependent viscosity, viscoelasticity, and thixotropy (SCHOWALTER; CHAFFEY; BRENNER, 1968; BARTHÉS-BIESEL; ACRIVOS, 1973). These complex features occur even when the emulsion is composed of Newtonian fluids and is dilute, i.e., when the concentration of the dispersed phase is small, from which the inter-droplet hydrodynamic interactions are negligible. In such a case, the rheological properties of the emulsion can be inferred considering a single droplet biphase system of corresponding constituents and volume fraction, and measuring the interfacial tension contribution to the system stress state when submitted to standard rheometric flows, i.e., steady simple shear, steady extensional, and small amplitude oscillatory shear or extensional flow (BATCHELOR, 1970).

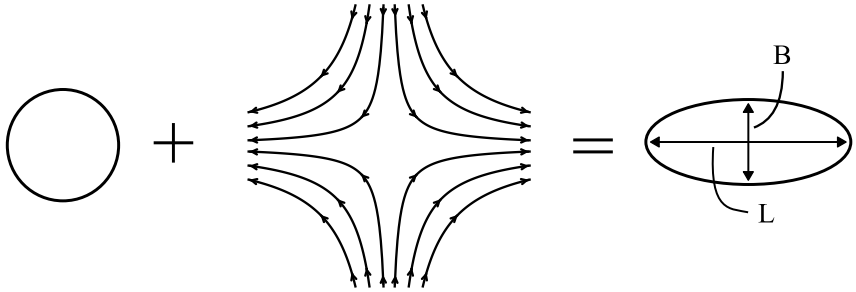

Figure 1.2 – Representative sketch of the deformation of a single droplet subjected to external planar extensional flow. L corresponds to the length of the major semi-axis, and B to the minor semi-axis length.

When a single suspended droplet undergoes a steady straining motion, the flow-induced viscous stresses on the droplet surface tend to distort the droplet, and the interfacial tension between the phases acts in a way to retain its spherical shape. In the case where these forces are balanced, the droplet attains an equilibrium prolate ellipsoidal shape (TAYLOR, 1934). Moreover, if the straining motion corresponds to an extensional flow, which is irrotational, the droplet's major axis remains aligned with the flow's extension direction, as depicted in Fig. 1.2.

In a planar extensional flow experiment, the response of a material is commonly characterized by two coefficients: the planar extensional viscosity, η_{ext}, and the second (or cross) extensional viscosity, η_{cross} (PETRIE, 2006). They are associated with the material normal stresses through

$$\eta_{ext} = \frac{(\sigma_{xx} - \sigma_{yy})}{\dot{\varepsilon}}, \quad \text{and} \quad \eta_{cross} = \frac{(\sigma_{zz} - \sigma_{yy})}{\dot{\varepsilon}},$$

where $\dot{\varepsilon}$ is the rate of extension, $\boldsymbol{\sigma}$ is the material stress tensor, and the subscripts indicate its components. While the first refers to the material resistance to be continuously stretched/compressed in the xy plane, the second refers to the material resistance to prevent continuous deformation in the z direction. For a Newtonian fluid, these two coefficients are constants and related to the shear viscosity, η_N, through $\eta_{ext} = 4\eta_N$ and $\eta_{cross} = 2\eta_N$, so that a simple shear experiment is sufficient to obtain both shear and extensional viscosities. For dilute emulsions, however, this does not hold true, so an extensional experiment is

needed. This is because for suspended droplets a net difference between the normal stresses occurs due to the extra stress promoted by the anisotropic distribution of normal stress jump at the interface as the droplet departs from its spherical to an ellipsoidal shape.

As the flow at the droplet scale is a low-Reynolds number flow, for a given set of the biphase system parameters such as shear viscosity ratio between the phases, interfacial tension, and droplet size, the droplet configuration, and the corresponding emulsion viscosities, are functions only of $\dot{\varepsilon}$. This is not the case, however, when the droplet is a polarizable media, such as ferrofluids. In this case, the droplet's configuration can be changed by the presence of external magnetic fields.

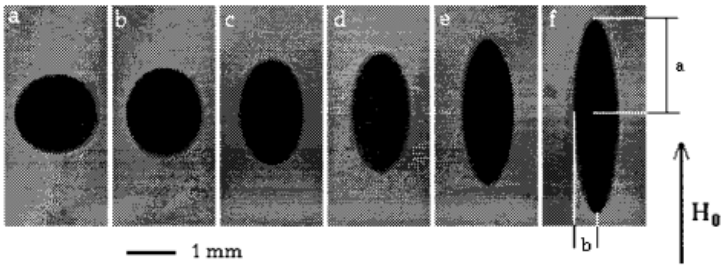

Figure 1.3 – Shape deformation of a ferrofluid droplet suspended in a quiescent liquid and subjected to uniform magnetic fields. The magnetic field intensity increases from left (a) to right (f). Adapted from (FLAMENT *et al.*, 1996).

Ferrofluids are colloidal solutions consisting of magnetic particles homogeneously dispersed in a carrier fluid, such as oil or water. The particles are single-domain ferri or ferromagnetic solid materials, meaning they have permanent magnetic properties (ROSENSWEIG, 2013). When the ferrofluid is subjected to a magnetic field, the particles undergo rotation in the direction of the magnetic field due to the arising torques. As long as the magnetic torques overcome the random Brownian motion, the ferrofluid achieves a net magnetization, $\boldsymbol{M}$. Ferrofluids have strong magnetization properties. A ferrofluid is said to be *superparamagnetic* when the magnetization always points in the direction of the magnetic field, in the way that $\boldsymbol{M} = \chi(H)\boldsymbol{H}$, where $\boldsymbol{H}$ is the magnetic field. The magnetic susceptibility, χ, generally follows Langevin dynamics, characterized by a linear regime (constant χ) in low fields followed by a saturation region as long as the field reaches strong values. An emulsion with a ferrofluid as the dispersed phase is called a ferrofluid emulsion. Ferrofluid emulsions have been synthesized since the end of the last century with the addition of dispersing agents to ensure stability, as did, for example, in the work of Bibette (1993).

Interfaces between phases with different magnetic susceptibilities have another source of stress jump when submitted to external magnetic fields, the magnetic one (CUNHA *et al.*, 2020). These magnetic stresses acting on the interface stretch the droplet in the field direction [see Fig. 1.3]. For these reasons, the extensional viscosities of a ferrofluid emulsion are functions not only of the $\dot{\varepsilon}$, but also of the applied magnetic field, so that $\eta_{ext} = \eta_{ext}(\dot{\varepsilon}, \boldsymbol{H_0})$, and $\eta_{cross} = \eta_{cross}(\dot{\varepsilon}, \boldsymbol{H_0})$. Directly due to the stress

jump term, and indirectly due to the changing in the droplet configuration caused by the magnetic-induced distortion.

The ferrofluid emulsion's rheology can be controlled by means of external magnetic fields, so it is a magnetorheological fluid. Magnetorheological fluids are attractive materials for several areas (TORRES-DÍAZ; RINALDI, 2014). In the automotive industry, these fluids can improve the operation of devices such as dampers, batteries, valves, and brakes (YANG *et al.*, 2020; ESHGARF; NADOOSHAN; RAISI, 2022). In microfluidic systems, they can be used for mixing, pumping, and separating target particles from heterogeneous mixtures (YANG *et al.*, 2016). Ferrofluid emulsions are also present in biomedical applications, where they can be used to deliver drugs to specific body locations by controlling the magnetic field (LIU; LI; LAM, 2018); or be used as a contrast agent for *In Vivo* Magnetic Resonance Imaging, taking advantage of its magneto-optical properties (AHMED *et al.*, 2013; YERIN; BELYKH, 2021). In all these cases, knowing about mechanical behavior of the ferrofluid emulsion is of fundamental importance. In some of them, knowledge about emulsion magnetic behavior is also very important. There are, however, unanswered questions about their mechanical and magnetic behavior. One of these questions is how ferrofluid emulsions are magnetized in extensional flows. Another is how the extensional rheology of such emulsions is affected by the presence of external magnetic fields.

1.2 Previous works

The study on the dynamics of suspended droplets and on the mechanical behavior of emulsions was founded with the G. I. Taylor works in the 1930s (TAYLOR, 1932; TAYLOR, 1934). In 1932, Taylor studied theoretically the rheology of emulsions formed by undeformed droplets and found that the shear viscosity of the emulsion is given by $\eta_e = \eta_c[1 + 2.5\beta(\lambda + 0.4)/(\lambda + 0.1)]$, where β is the volume fraction of the dispersed phase, and λ is the ratio between the shear viscosities of the dispersed phase, η_d, and that of the continuous phase, η_c. This result is valid for low volume fractions ($\beta < 5\%$) and low Ca, which measures the flow strength compared to the interfacial tension. In 1934, Taylor studied experimentally the deformation and breakup of suspended droplets subjected to simple shear and planar extensional flows. For this, the author created the four-roll mill apparatus, which is capable of generating a stagnation point planar extensional flow with a steady strain rate. Taylor found that if the interfacial tension is large enough the droplet reaches a steady prolate ellipsoidal shape. In the limits of small deformations, the deformation D (see Fig. 1.2) varies linearly with Ca. If Ca is high enough, the droplet subjected to planar extension continuously deforms until it breaks up into many daughter droplets. The distortion is significantly more pronounced in the planar extension than in simple shear. For this reason, the extensional flow is said to be strong.

Since the works of Taylor, many experimental and analytical studies were conducted

to analyze the dynamics and breakup of viscous droplets in extensional flows (BARTHES-BIESEL; ACRIVOS, 1973; ACRIVOS; LO, 1978; GRACE, 1982; BENTLEY; LEAL, 1986; HSU; LEAL, 2009), and the extensional rheology (OLDROYD, 1953; SCHOWALTER; CHAFFEY; BRENNER, 1968; BARTHÉS-BIESEL; ACRIVOS, 1973). Bentley and Leal (1986) used an improved computer-controlled version of the four-roll mill apparatus to systematically study the deformation and breakup of viscous droplets covering a wide range of λ. Their results are valuable until today. This work was later proceeded by Hsu and Leal (2009) who analyzed the case of $\lambda = 1$. The theoretical analysis of the cited works on droplet dynamics and extensional rheology contributed to the prediction of the dynamics and emulsion mechanical behavior, but are restricted to nearly spherical, or slender droplet shapes.

With the growing development of computers and numerical methods in the last decades, numerical simulation becomes an important tool for the study of emulsions, as it eliminates any restriction on droplet shapes and is able to detail the important physical quantities distribution over the system and droplet surface. Since then, the problem of emulsions has been studied through numerical methods. Kennedy, Pozrikidis and Skalak (1994) analyzed the deformation of droplets and shear rheology of dilute emulsions using a boundary integral formulation. Loewenberg and Hinch (1996) and Oliveira and Cunha (2015) used similar methods to analyze the rheology of concentrated emulsions respectively in simple shear and oscillatory shear. Li and Sarkar (2005) analyzed the oscillatory extensional rheology of dilute emulsions using a front-tracking method. Park *et al.* (2019) used a Taylor analogy numerical method to analyze the droplet dynamics in planar extensional flow.

The field-induced distortion of ferrofluid droplets in an otherwise quiescent liquid has also been studied in the last decades through experimental and numerical methods. Its understanding is already well-established (FLAMENT *et al.*, 1996; AFKHAMI *et al.*, 2010). The dynamics of ferrofluid droplets under the simultaneous action of external magnetic fields and hydrodynamics flows, however, is yet to be fully understood. The first study in this regard was presented by Jesus, Roma and Ceniceros (2018), who analyzed the behavior of superparamagnetic ferrofluid droplets in simple shear flows when uniform magnetic fields are externally applied in the velocity gradient direction. The work of Jesus, Roma and Ceniceros (2018) was quickly followed by other similar studies in simple shear (HASSAN; ZHANG; WANG, 2018; CAPOBIANCHI; LAPPA; OLIVEIRA, 2018; CUNHA *et al.*, 2018; CUNHA *et al.*, 2020; ISHIDA; MATSUNAGA, 2020; CAPOBIANCHI *et al.*, 2021; ABICALIL *et al.*, 2021). Despite the differences in formulation and numerical methods, these studies confirmed that, when subjected to both flow and uniform magnetic fields, the ferrofluid droplets assume ellipsoidal shapes (when the droplet is not lead to breakup), but this time they can also assume oblate shapes, instead of prolate. The shape and orientation angle with respect to the flow are determined by a balance between viscous, magnetic, and capillary forces at the interface that in turn depends on the direction and

intensity of the external magnetic field, so they can be controlled. In like manner, Cunha *et al.* (2018), and other authors, studied the conditions for ferrofluid droplet breakup in simple shear and found that the magnetic field can either induce or prevent breakup (CUNHA *et al.*, 2018; MAJIDI *et al.*, 2022; ISHIDA *et al.*, 2022).

Numerical studies on dilute emulsion rheology, in which can be assumed there are no interdroplet hydrodynamic or magnetic interactions, generally use the *particle stress* formulation of Batchelor (1970), that extrapolates the extra stress caused by the presence of one droplet to the bulk emulsion stress tensor (KENNEDY; POZRIKIDIS; SKALAK, 1994; LI; SARKAR, 2005). While the particle stress of regular viscous droplets is a function of the viscosity difference and interfacial tension between the phases, an emulsion formed by ferrofluid droplets experiences additional compression due to the magnetic permeability difference between the phases. Following the procedure of Batchelor (1970), Cunha *et al.* (2020) introduced a new formulation for the particle stress of ferrofluid droplets in suspension, which takes advantage of the Level-Set formulation for the interface problem. Shortly after, Ishida and Matsunaga (2020) and Capobianchi *et al.* (2021) presented similar procedures. These three works, in addition to the ferrofluid droplet dynamics analysis, studied the shear rheology through their new particle stress formulation. Essentially, they showed that external magnetic fields can effectively tune the shear viscosity and normal stress coefficients. Moreover, they showed that depending on the orientation of the external magnetic field, the magnetization of the system has an angle with the external field, meaning that internal magnetic torques are induced in the ferrofluid emulsion. As a consequence, the particle stress becomes nonsymmetric. The lack of symmetry in the stress tensor of ferrofluid emulsions requires the introduction of additional material functions, such as the rotational viscosity of Cunha *et al.* (2020).

We observe from the state-of-the-art that there is a growing interest in understanding the ferrofluid droplet dynamics and mechanical behavior of ferrofluid emulsions. The great majority of them, however, focused on simple shear, whether with respect to ferrofluid droplet dynamics and breakup or with respect to rheology. Recently, Abdo *et al.* (2023) studied the ferrofluid droplet dynamics and ferrofluid emulsion rheology on oscillatory shear. To the best of our knowledge, there are no studies regarding the effects of magnetic fields in either ferrofluid droplet dynamics, breakup, or rheology, in extensional flows. Mandal *et al.* (2018) is the only work that studied droplet deformation in extensional flows and extensional rheology of emulsions formed by polarizable media under the action of external fields. In their work, the droplets are electrically polar and the flow is a uniaxial extension. The authors found that the presence of an electric field can either amplify the extensional-thickening behavior of the emulsion or even invert it to an extensional-thinning behavior.

1.3 Contributions of the present work

As noted above, prior to this work, no studies have been conducted to analyze either the deformation, magnetization, and breakup of ferrofluid droplets in extensional flows or the dilute ferrofluid emulsion extensional rheology. In order to fill this gap, we conducted here three-dimensional numerical experiments on a suspended ferrofluid droplet subjected to both planar extensional flow and uniform magnetic fields. Specifically, we investigate the effects of the magnetic fields on the droplet's configuration (in other words, emulsion microstructure), magnetization, and breakup, and on the corresponding extensional rheology of dilute ferrofluid emulsions. Altogether, four directions for the applied magnetic field are analyzed, among which three are in the flow's main direction, and the other is not. First, we analyze the cases in which the droplet shape remains steady so that the steady rheology can be assessed. Then, we investigate the conditions of flow and magnetic field for which the droplet breakup can be expected to occur.

We show that the droplet deformation strongly depends on the applied magnetic field intensity and direction relative to the flow, so it can either prevent or induce breakup. The droplet shape and magnetization are directly related to the extensional viscosities. Hence, the extensional rheology of ferrofluid emulsions can be controlled by external magnetic fields. In particular, when the magnetic field is in a direction different from the three flow's main directions, unexpected shear stresses are present in the system. Moreover, they are nonsymmetric. For this reason, new material functions, said shear and rotational viscosities, are necessary to fully characterize the extensional rheology of ferrofluid emulsions. It is the first time that shear stresses are reported for emulsions in extensional flows. The present authors believe that these results are valuable not only for ferrofluid emulsions control characterization but also for the field of non-Newtonian fluid mechanics. The main results of this work, with the exception of the breakup analysis, were recently published in co-authorship with other researchers in the Physical Review Fluids, Volume 8, Issue 6 (GUILHERME *et al.*, 2023),

The remainder of this work is organized as follows. In Chapter 2, we present the description of the problem and the dimensionless parameters involved. We also describe the governing equations and the methods to evaluate the variables of interest such as the stress tensor and the magnetization of the ferrofluid emulsion. In Chapter 3, we describe the numerical methodology, which includes the projection method to solve the equations of motion, and the Level-Set method for the interface problem. A mesh convergence test is presented at the end of this chapter. In Chapter 4, then, we present validation tests and discuss the main results obtained in this study. Finally, in Chapter 5, we present our concluding remarks.

2 Problem formulation

2.1 Problem statement

The system under consideration is that of a ferrofluid droplet of radius a and viscosity η_d immersed in another nonmagnetizable liquid of viscosity η_c and the same density ρ as the droplet. Figure 2.1 shows a schematic view of the problem. Both fluids are Newtonian, and σ is the interfacial tension between them. The ferrofluid is considered superparamagnetic with constant magnetic susceptibility χ, i.e., the magnetic field intensities are not great enough to surpass the linear regime of magnetization. The droplet is initially ($t = 0$) in its equilibrium spherical shape and centered at the origin of the coordinate system. The system is ideally subjected to a planar extensional flow of constant extension rate $\dot{\varepsilon}$ so that the velocity at $||\boldsymbol{x}|| \to \infty$, $\boldsymbol{u}_\infty$, is given by

$$\boldsymbol{u}_\infty = \dot{\varepsilon} \begin{bmatrix} 1 & 0 & 0 \\ 0 & -1 & 0 \\ 0 & 0 & 0 \end{bmatrix} \cdot \boldsymbol{x}. \tag{2.1}$$

In addition to the external flow, a uniform magnetic field, $\boldsymbol{H_0}$, is externally applied over the system, both being initialized at the same time. The presence of the ferrofluid droplet disturbs both the flow and the magnetic field in its vicinity so that the solution domain needs to be sufficiently large in order to impose $\boldsymbol{u}_\infty$ and $\boldsymbol{H_0}$ at the domain boundaries without accounting for significant confinement effects. Bearing this in mind, we choose a lattice computational domain with edge sizes equal to $S_x = 12.5a$, $S_y = 10a$, and $S_z = 7.5a$ in the x, y, and z direction, respectively, which gives a volume fraction of the dispersed phase $\beta \approx 0.45\%$. This choice is consistent with numerical and experimental studies of droplets in extensional flows (BENTLEY; LEAL, 1986; HSU; LEAL, 2009; PARK *et al.*, 2019) (in some cases, we use an even larger domain. Details are given in Sec. 3.5). The volume fraction is also consistent with the assumption of dilute emulsion necessary for the rheology assessment via the procedure explained in Sec. 2.3.

The Reynolds number is defined here as $Re = \rho a^2 \dot{\varepsilon}/\eta_c$, where the characteristic length is the droplet's radius $l_c = a$, the time scale is that of the flow, i.e., the inverse of the rate of extension $t_c = \dot{\varepsilon}^{-1}$, and the characteristic velocity is, then, $U_c = a\dot{\varepsilon}$. Given that the droplet is sufficiently small, as it is assumed in this work, its dynamics occur in a

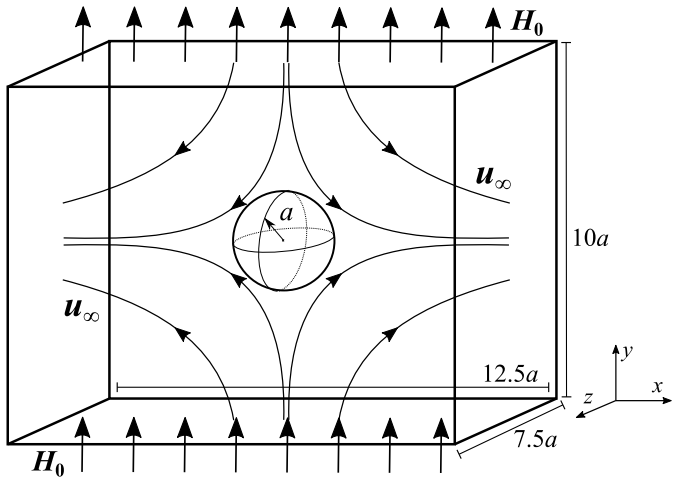

Figure 2.1 – Sketch of the problem (not to scale). The droplet is initially spherical, has radius a, and the domain size (normalized by a) is 12.5, 10, and 7.5 in the x, y, and z direction, respectively ($\beta \approx 0.45\%$). The system is subjected to a planar extensional flow [Eq. (2.1)] that defines the directions of flow extension (x direction), flow compression (y direction), and neutral (z direction). The system is also subjected to a uniform magnetic field $\boldsymbol{H_0}$ applied externally (in this sketch it is in the y direction). The origin $\boldsymbol{x} = \boldsymbol{0}$ is fixed at the droplet center. Reprinted from (GUILHERME *et al.*, 2023, p. 4). © 2023 by American Physical Society.

low-Re regime, which is inertia-free. Moreover, there is no variation in density between the phases so there are no buoyancy effects. In such a situation and in the absence of an applied magnetic field, the ferrofluid droplet dynamics result from the competition between viscous forces that tend to stretch it in the extension direction (x direction) and compress it in the compression direction (y direction), and the restorative capillary forces that act in the way to bring the droplet to its spherical shape. The capillary number measures the ratio between these two effects. It can be defined as $Ca = \eta_c a\dot{\varepsilon}/\sigma$, being the droplet less likely to be stretched in lower values of Ca. Another important parameter is the viscosity ratio between dispersed and continuous phases, $\lambda = \eta_d/\eta_c$, which influences the way the viscous forces act at the interface between the phases. The two parameters, Ca and λ, define, therefore, the droplet's configuration in the absence of external magnetic fields. When in the presence of an external magnetic field, however, magnetic forces also play an important role in the droplet's configuration, with their effects depending on the applied direction. To account for its effects, two other nondimensional groups are included. The magnetic capillary number, defined as $Ca_{mag} = \mu_0 a||\boldsymbol{H_0}||^2/\sigma$, which corresponds to the ratio between magnetic and capillary forces, and dispersed-to-continuous phase magnetic permeability ratio, $\zeta = \mu_d/\mu_0$, where $\mu_d = \mu_0(1+\chi)$ is the dispersed phase magnetic permeability. Note that the magnetic permeability of the continuous phase is taken to be that of the free space, μ_0, since it is nonmagnetizable.

For reference, the relevant nondimensional parameters are summarized as follows:

$$Re = \frac{\rho a^2 \dot{\varepsilon}}{\eta_c}, \quad Ca = \frac{\eta_c a \dot{\varepsilon}}{\sigma}, \quad Ca_{mag} = \frac{\mu_0 a ||\boldsymbol{H_0}||^2}{\sigma}, \quad \lambda = \frac{\eta_d}{\eta_c}, \quad \text{and} \quad \zeta = \frac{\mu_d}{\mu_0}. \tag{2.2}$$

Regarding the competition between the viscous, magnetic, and capillary forces, the droplet can reach a steady equilibrium shape or not. Because the viscous forces promoted by the external flow are responsible for droplet continuous stretching, there exists a critical capillary number Ca_c for a given set of λ, Ca_{mag}, ζ, and magnetic field direction, where higher values of Ca lead to an unsteady burst situation and lower values lead to a steady configuration of the droplet. When the droplet configuration, i.e., the corresponding dilute emulsion microstructure, achieves a steady state ($Ca < Ca_c$), we can assess the steady extensional rheology of the corresponding ferrofluid emulsion. From the magnetic point of view, the integration of the magnetization field over the domain tells us about how hydrodynamics aspects affect the system bulk magnetization, i.e., the magnetization of the corresponding dilute ferrofluid emulsion.

In this work, we investigate the steady droplet configuration and magnetization, and the corresponding ferrofluid emulsion rheology for different Ca, Ca_{mag}, and magnetic field directions. In these cases, we chose $\lambda = 1$ because we are interested in assessing only the effects of the magnetic field. This value is consistent with previous studies of ferrofluid droplets in shear flows ($\lambda = 0.5 - 5$) (HASSAN; ZHANG; WANG, 2018; CUNHA *et al.*, 2020; ISHIDA; MATSUNAGA, 2020; CAPOBIANCHI *et al.*, 2021; ABICALIL *et al.*, 2021). We also investigate the limits for stable ferrofluid emulsions (Ca_c) for different Ca_{mag} and magnetic field directions. In these cases, however, we explore two decades of λ. In all cases, the susceptibility is set to $\chi = 1$. This value is consistent with previous experiments of ferrofluid droplets in quiescent liquids ($\chi = 0.9 - 2.2$) (FLAMENT *et al.*, 1996; AFKHAMI *et al.*, 2010) and simulations of ferrofluid droplets in shear flows ($\chi = 0.5 - 1.0$) (HASSAN; ZHANG; WANG, 2018; CUNHA *et al.*, 2020; ISHIDA; MATSUNAGA, 2020; CAPOBIANCHI *et al.*, 2021; ABICALIL *et al.*, 2021). The following sections of this chapter describe the mathematical modeling of the problem in its dimensional and nondimensional forms, as well as the procedures used to evaluate the variables of interest, such as the droplet deformation, the droplet magnetization, the particle stress, and Ca_c.

2.2 Governing Equations

The motion of a ferrofluid droplet immersed in a nonmagnetizable liquid subjected to both an external flow field and a uniform magnetic field is governed by the incompressible Navier-Stokes equations with the addition of the magnetic force term.

2.2.1 Equations of the fluid motion

The Navier-Stokes equations for a two-phase incompressible and buoyancy-free flow in an Eulerian frame of reference are given by the mass conservation law

$$\boldsymbol{\nabla} \cdot \boldsymbol{u} = 0, \tag{2.3}$$

and the momentum balance

$$\rho \left(\frac{\partial \boldsymbol{u}}{\partial t} + \boldsymbol{u} \cdot \nabla \boldsymbol{u} \right) = -\nabla p + \boldsymbol{\nabla} \cdot [\eta(\boldsymbol{x})(\nabla \boldsymbol{u} + \nabla \boldsymbol{u}^T)] + \boldsymbol{F_c} + \boldsymbol{F_m}, \tag{2.4}$$

where $\boldsymbol{u}$ is the velocity field, p is the pressure, $\eta(\boldsymbol{x})$ is the fluid viscosity, which depends on the phase, $\boldsymbol{F_c}$ and $\boldsymbol{F_m}$ are the capillary and magnetic body forces per unit volume, respectively. The Young-Laplace condition states that the normal stress jump across a curved interface is equal to $(-\sigma\kappa\hat{\boldsymbol{n}})$, where κ is the local mean curvature of the interface, and $\hat{\boldsymbol{n}}$ is the normal unit vector pointing to the convex side (in our case, outward the droplet) (LANDAU; LIFSHITZ, 2013). Following the Young-Laplace condition, the capillary force per unit volume is given by $\boldsymbol{F_c} = -\sigma\kappa\hat{\delta}(\boldsymbol{x} - \boldsymbol{x_\Gamma})\hat{\boldsymbol{n}}$, where $\boldsymbol{x_\Gamma}$ is the position vector of the interface's point which is closest to $\boldsymbol{x}$ and $\hat{\delta}(\boldsymbol{x})$ is the spatial Dirac function, responsible for concentrating the force density in the interface. The magnetic force term corresponds to the Kelvin force $\boldsymbol{F_m} = \mu_0 \boldsymbol{M} \cdot \nabla \boldsymbol{H}$, where $\boldsymbol{M}$ is the magnetization field, given that the ferrofluid is electrically non-conducting and superparamagnetic (ROSENSWEIG, 2013).

2.2.2 Magnetic problem

From the assumption of superparamagnetism, the magnetization field inside the ferrofluid droplet is locally parallel to the magnetic field. Further, we assume that the magnetic field will never be high enough to surpass the ferrofluid magnetization's linear regime so that $\boldsymbol{M} = \chi \boldsymbol{H}$, where χ is constant [for an explanation of Langevin and nonequilibrium regimes of magnetization, see (SHLIOMIS, 2001)]. Out of the droplet, the magnetization is null due to the fact the continuous phase is nonmagnetizable, $\chi = 0$. Therefore, we can define a piecewise constant scalar function for permeability ratio in function of space, $\zeta(\boldsymbol{x})$. Inside the droplet, we have that $\zeta(\boldsymbol{x}) = 1 + \chi$. Outside, we have that $\zeta(\boldsymbol{x}) = 1$. Using this definition, the magnetic force $\boldsymbol{F_m}$ can be written as a function of $\boldsymbol{H}$ as

$$\boldsymbol{F_m} = \mu_0(\zeta(\boldsymbol{x}) - 1)\boldsymbol{H} \cdot \nabla \boldsymbol{H}. \tag{2.5}$$

At the magnetostatic limit, the Maxwell's equations are $\boldsymbol{\nabla} \cdot \boldsymbol{B} = 0$ and $\nabla \times \boldsymbol{H} = \boldsymbol{0}$, where $\boldsymbol{B} = \mu_0(\boldsymbol{M} + \boldsymbol{H}) = \mu_0 \zeta(\boldsymbol{x})\boldsymbol{H}$ is the magnetic induction field. From the fact $\boldsymbol{H}$ is

irrotational, it can be described by the gradient of a potential. The magnetic potential field ψ is then given by

$$\nabla\psi = -\boldsymbol{H}. \tag{2.6}$$

From the solenoidal nature of the magnetic induction field, its definition, and the relation given in Eq. (2.6), it follows that

$$\boldsymbol{\nabla} \cdot (\zeta(\boldsymbol{x})\nabla\psi) = 0, \tag{2.7}$$

which is the Poisson equation for the magnetic potential. If $\zeta(\boldsymbol{x})$ is uniform throughout the domain, the uniform magnetic field imposed at the boundaries would lead to a uniform magnetic field all over the system. The presence of a ferrofluid droplet, however, perturbs the magnetic field due to the appearance of gradients in $\zeta(\boldsymbol{x})$. As a consequence, from Eq. (2.7), there would be gradients in $\boldsymbol{H}$, which in turn would induce magnetic forces at the interface.

2.2.3 Boundary conditions

In all cases covered here, a uniform applied magnetic field $\boldsymbol{H_0}$ is considered. From the numerical point of view, fixed von Neumann boundary conditions for ψ are set to all boundaries, provided that the droplet will not attain them. From Eq. (2.6) we have that

$$\frac{\partial\psi}{\partial n} = -\boldsymbol{H_0} \cdot \boldsymbol{n} \tag{2.8}$$

at the boundaries, where $\boldsymbol{n}$ is the normal vector pointing outward the domain boundary, and $\partial/\partial n$ is the normal derivative operator.

Differently from the magnetic potential, periodicity is set for the hydrodynamic variables in the direction normal to the extension plane (z direction). In the other domain boundaries, planar extensional flow, Eq. (2.1), is imposed to the velocity field

$$\boldsymbol{u} = \boldsymbol{u_\infty}. \tag{2.9}$$

Finally, the pressure field has homogeneous von Neumann conditions for the non-periodic boundaries, since the imposed flow is linear and the motion is inertia-free. This can be readily verified by applying Eq. (2.9) to the inertia-free Navier-Stokes equations. At these boundaries, therefore, we have that

$$\frac{\partial p}{\partial n} = 0. \tag{2.10}$$

2.2.4 Nondimensional equations

The governing equations can be converted into a nondimensional form in order to generalize the results. Appropriate scaling of the variables is of fundamental importance. As already depicted in Section 2.1, the characteristics length scale, time scale, and velocity scale are, respectively, a, $\dot{\varepsilon}^{-1}$, and $a\dot{\gamma}$, which give rise to the Reynolds number $Re = \rho a^2 \dot{\varepsilon}/\eta_c$.

The droplet dynamics occurs on a scale where inertia effects are negligible, as assumed earlier. In order to check this suppose a typical ferrofluid of viscosity $\eta = 0.003$ kg/m.s and density $\rho = 1020$ kg/m^3 (KÚDELČÍK; HARDOŇ; VARAČKA, 2017). A droplet of radius $a = 5$ μm immersed in a liquid of the same density and viscosity ($\lambda = 1$) and subjected to a high extension rate of $\dot{\varepsilon} = 500$ s^{-1} would lead to only $Re \approx 0.004$, characterizing a low-Reynolds number flow. It confirms the assumption of low-Re used in this work.

The pressure is scaled with $\rho a^2 \dot{\varepsilon}^2$. The representative scale for the magnetic field is the magnitude of the applied magnetic field, $H_0 = \|\boldsymbol{H_0}\|$. Then for the magnetic potential, we have the scaling aH_0. Finally, since we can have different viscosities between the phases, it is necessary to define a characteristic viscosity. We choose the continuous-phase viscosity, η_c, in order to match with the nondimensional parameters definition given earlier.

Using the characteristic scales described above we get the following nondimensional variables:

$$\tilde{t} = t\dot{\epsilon}, \quad \tilde{\boldsymbol{x}} = \frac{\boldsymbol{x}}{a}, \quad \tilde{\boldsymbol{u}} = \frac{\boldsymbol{u}}{a\dot{\varepsilon}}, \quad \tilde{p} = \frac{p}{\rho a^2 \dot{\varepsilon}^2}, \quad \tilde{\boldsymbol{H}} = \frac{\boldsymbol{H}}{H_0}, \quad \tilde{\psi} = \frac{\psi}{aH_0}, \quad \text{and} \quad \tilde{\eta}(\boldsymbol{x}) = \frac{\eta(\boldsymbol{x})}{\eta_c} \tag{2.11}$$

Substituting these variables in Eqs. (2.3), (2.4) and (2.7) we get the nondimensional form of the governing equations as follows:

$$\tilde{\nabla} \cdot \tilde{u} = 0 \tag{2.12}$$

for the continuity equation,

$$\begin{aligned} &\frac{\partial \tilde{\boldsymbol{u}}}{\partial \tilde{t}} + \tilde{\boldsymbol{u}} \cdot \tilde{\nabla}\tilde{\boldsymbol{u}} = -\tilde{\nabla}\tilde{p} + \frac{1}{Re}\tilde{\nabla} \cdot [\tilde{\eta}(\tilde{\boldsymbol{x}})(\tilde{\nabla}\tilde{\boldsymbol{u}} + \tilde{\nabla}\tilde{\boldsymbol{u}}^T)] \\ &-\frac{1}{ReCa}\tilde{\kappa}\hat{\delta}(\tilde{\boldsymbol{x}}_\Gamma - \tilde{\boldsymbol{x}})\boldsymbol{n} + \frac{Ca_{mag}}{ReCa}(\zeta(\tilde{\boldsymbol{x}}) - 1)\tilde{\boldsymbol{H}} \cdot \tilde{\nabla}\tilde{\boldsymbol{H}} \end{aligned} \tag{2.13}$$

for the momentum balance,

$$\tilde{\nabla} \cdot (\zeta(\tilde{\boldsymbol{x}})\tilde{\nabla}\tilde{\psi}) = 0 \tag{2.14}$$

for the magnetic potential Poisson's equation, and

$$\tilde{\boldsymbol{H}} = -\tilde{\nabla}\tilde{\psi} \tag{2.15}$$

for the magnetic field.

These coupled equations are solved in space and time by using the numerical methods described in Chapter 3. It is worth noting that the interface problem is treated using the Level-Set method, presented in Sec. 3.3. In this method, the physical variables that are functions of space are substituted to smoothed versions as functions of ϕ, the Level-Set scalar variable. They are $\eta(\boldsymbol{x})$ and $\zeta(\boldsymbol{x})$. $\hat{\delta}(\boldsymbol{x})$ present in the capillary term in Eq. (2.13) is also modified. Details are given in Sec. 3.3.2.

2.3 Rheology assessment

In this work, both continuous and dispersed phase fluids are considered to be Newtonians, which means that their stress state responds linearly with the rate of strain which they are submitted through the Newton's Law of viscosity, $\boldsymbol{\sigma} = -p\boldsymbol{I} + 2\eta\boldsymbol{D}$, where $\boldsymbol{\sigma}$ is the Cauchy's stress tensor, $\boldsymbol{I}$ is the identity tensor, and $\boldsymbol{D}$ is the rate of strain tensor, i.e., the symmetric part of $\nabla\boldsymbol{u}$. Although both phases are Newtonian, an emulsion formed by a combination of them manifests non-Newtonian behavior due to the fact that the droplets change in shape and orientation as a function of the extension/shear rate. The change in stress for emulsions of deformable droplets is modeled through the addition of an extra stress, called the particle stress (KIM; KARRILA, 2013). A ferrofluid emulsion, when submitted to an external field, besides having its droplets' configurations changed due to the action of the magnetic forces, has yet another source of stress due to the magnetic forces at the interface between the phases, as we will see later in this section. The stress tensor of a ferrofluid emulsion is then described by

$$\boldsymbol{\sigma} = -p\boldsymbol{I} + 2\eta\boldsymbol{D} + \boldsymbol{\sigma}^d, \tag{2.16}$$

where $\boldsymbol{\sigma}^d$ is the extra stress due to the droplet commonly known as the particle stress. It will from now on, however, be referred to as droplet stress, as it is more appropriate for our case.

2.3.1 Droplet contribution to the stress

In a dilute ferrofluid emulsion of volume fraction β, treated as a homogeneous continuous fluid in the macroscopic scale, and in which it can be considered that there are neither hydrodynamic nor magnetic interactions between the droplets, the droplet stress can be obtained by the extrapolation of the extra stress caused by the presence of one single droplet in a volume V of corresponding volume fraction. Landau and Lifshitz (2013)

and Batchelor (1970) developed the expression for proper computation of the droplet stress in terms of the difference in viscosity between the phases and the normal stress jump at the interface. For regular droplets, the stress jump is given by the capillary stress. In this section, we describe how the magnetic stress can be included in the expression, in order to properly compute the droplet stress for superparamagnetic ferrofluid droplets. This approach was first used in the work of Cunha *et al.* (2020), and its accuracy was confirmed in the three-dimensional study of ferrofluid emulsions in shear flows of Abicalil *et al.* (2021).

First, consider the signed distance function from the interface ϕ, where negative values are obtained inside the droplet and positive outside. We can substitute $\hat{\delta}(\boldsymbol{x})$ and $\zeta(\boldsymbol{x})$ to $\delta(\phi)|\nabla\phi|$ and $\zeta(\phi)$, respectively, where $\delta(\phi)$ is a one-dimensional Dirac function, and $\zeta(\phi) = \zeta + (1-\zeta)\mathcal{H}(\phi)$. $\mathcal{H}(\phi)$ is the classical one-dimensional Heaviside function (0 when $\phi < 0$, and 1, when $\phi > 0$). Using them, and the fact that $|\nabla\phi| = 1$, we can write the capillary and magnetic forces at the droplet surface as $\boldsymbol{F_c} = -\sigma\kappa\delta(\phi)\hat{\boldsymbol{n}}$ and $\boldsymbol{F_m} = \mu_0(\zeta(\phi)-1)\boldsymbol{H}\cdot\nabla\boldsymbol{H}$, respectively. The latter can be written as follows:

$$\boldsymbol{F_m} = \nabla\left[\frac{1}{2}\mu_0(\zeta(\phi)-1)H^2\right] - \frac{1}{2}\mu_0 H^2\nabla\zeta(\phi) \tag{2.17}$$

where H is the magnetic field intensity, i.e., $H = \|\boldsymbol{H}\|$.

While the first term of Eq. (2.17) can be readily incorporated into a modified pressure field, thus playing no role in the flow other than ensuring incompressibility, the second is of special importance for the droplet dynamics and emulsion rheology. As $\nabla\zeta(\phi) = -\chi\delta(\phi)\hat{\boldsymbol{n}}$, where we have used that $\nabla\zeta(\phi) = -\chi\nabla\mathcal{H}(\phi), \nabla\mathcal{H}(\phi) = \delta(\phi)\nabla\phi$, and $\hat{\boldsymbol{n}} = \nabla\phi$ (the relations involving the signed distance function ϕ are demonstrated in Sec. 3.3), the second term of Eq. (2.17) corresponds to a normal stress jump of intensity $\frac{1}{2}\mu_0\chi H^2$ across the fluid interface.

The momentum balance in a control volume of width $2e$ around a portion Γ of the droplet surface leads to

$$(\hat{\boldsymbol{n}}\cdot\boldsymbol{\sigma}^o)\Gamma^o - (\hat{\boldsymbol{n}}\cdot\boldsymbol{\sigma}^i)\Gamma^i + \int_{-e}^{e}\left[\frac{1}{2}\mu_0\chi H^2 - \sigma\kappa\right]\Gamma\delta(\phi)|\nabla\phi|\hat{\boldsymbol{n}}\mathrm{d}\phi = \boldsymbol{0} \tag{2.18}$$

where $\boldsymbol{\sigma}$ is the stress tensor of each fluid phase and the superscripts i and o are used to distinguish quantities of the inner and outer phases, respectively. Figure 2.2 shows an illustrative scheme of the force balance in the control volume. Using the convolution property of $\delta(\phi)$ and taking the limit $e \to 0$, Eq. (2.18) becomes

$$\hat{\boldsymbol{n}}\cdot\boldsymbol{\sigma}^o - \hat{\boldsymbol{n}}\cdot\boldsymbol{\sigma}^i + \frac{1}{2}\mu_0\chi H^2\hat{\boldsymbol{n}} - \sigma\kappa\hat{\boldsymbol{n}} = \boldsymbol{0} \tag{2.19}$$

Hence, the stress jump across the interface, $\Delta f = \hat{\boldsymbol{n}}\cdot[\boldsymbol{\sigma}^o - \boldsymbol{\sigma}^i]$, is given by

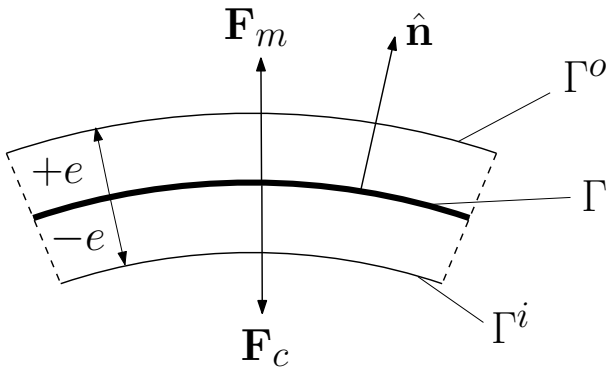

Figure 2.2 – Force balance in a control volume of width $2e$ around a portion Γ of the droplet surface. The superscripts i and o are used to distinguish quantities of the inner and outer phases, respectively. Reprinted from (GUILHERME *et al.*, 2023, p. 4). © 2023 by American Physical Society.

$$\Delta f = \sigma\kappa\hat{\boldsymbol{n}} - \frac{1}{2}\mu_0\chi H^2\hat{\boldsymbol{n}} \tag{2.20}$$

Following the formulation of the extra stress given by Batchelor (1970) for a general particulate system in terms of the stress jump and difference in phases viscosities, the exact equation for the droplet stress for a dilute ferrofluid emulsion reads

$$\boldsymbol{\sigma}^d = \frac{1}{V}\int_\Gamma \left[\left(\sigma\kappa - \frac{1}{2}\mu_0\chi H^2\right)\boldsymbol{x}\hat{\boldsymbol{n}} + \eta_c(\lambda-1)(\boldsymbol{u}\hat{\boldsymbol{n}} - \hat{\boldsymbol{n}}\boldsymbol{u})\right]\mathrm{d}S. \tag{2.21}$$

In nondimensional form, we have that

$$\tilde{\boldsymbol{\sigma}}^d = \frac{1}{\tilde{V}}\int_\Gamma \frac{1}{Ca}\left[\tilde{\kappa}\tilde{\boldsymbol{x}}\hat{\boldsymbol{n}} - \frac{Ca_{mag}}{2}(\zeta-1)\tilde{H}^2\tilde{\boldsymbol{x}}\boldsymbol{n} + Ca(\lambda-1)(\tilde{\boldsymbol{u}}\hat{\boldsymbol{n}} + \hat{\boldsymbol{n}}\tilde{\boldsymbol{u}})\right]\mathrm{d}\tilde{S}, \tag{2.22}$$

where $\tilde{V} = V/a^3$, and with $\tilde{\boldsymbol{\sigma}}^d = \boldsymbol{\sigma}^d/\eta_c\dot{\varepsilon}$.

Note that this derivation is exact and does not depend on the interfacial thickness of the Level-Set method used to smooth discontinuous properties across the interface, presented in Sec. 3.3.

2.3.2 Extensional rheology

Two material properties are commonly used to describe the resistivity, i.e., the dissipation of energy, of a fluid undergoing steady planar extensional flow (PETRIE, 2006). They are related to the diagonal components of Cauchy's stress tensor when the material is subjected to the planar extensional flow described by Eq. (2.1). They are the *planar extensional viscosity*, defined as $\eta_{ext} = (\sigma_{xx} - \sigma_{yy})/\dot{\varepsilon}$, and the *second extensional viscosity*, defined as $\eta_{cross} = (\sigma_{zz} - \sigma_{yy})/\dot{\varepsilon}$, in which the subscript denotes the tensor component. η_{ext} refers to the material resistance to be continuously stretched in the x direction (extension

direction) and compressed in y direction (compression direction), while η_{cross} refers to the material resistance to prevent continuous deformation in the z direction (neutral direction). Note that, for a Newtonian fluid, these viscosities do not depend on the extension rate, and are related to the shear viscosity, η_N, by $\eta_{ext} = 4\eta_N$, and $\eta_{cross} = 2\eta_N$. For a ferrofluid emulsion, the droplet stress, described by Eq. (2.22), introduces dependence of these viscosities on the extension rate, surface tension, and applied magnetic field intensity and direction. As a result, a deviation from the Newtonian behavior is expected. In order to measure these effects, we analyze here the excess extensional viscosities normalized by the shear viscosity of the continuous phase, given by

$$\tilde{\eta}_p = \tilde{\sigma}^d_{xx} - \tilde{\sigma}^d_{yy}, \tag{2.23}$$

and

$$\tilde{\eta}_2 = \tilde{\sigma}^d_{zz} - \tilde{\sigma}^d_{yy}, \tag{2.24}$$

where $\tilde{\eta}_p$ is the nondimensional droplet contribution to the planar extensional viscosity, and $\tilde{\eta}_2$ is the nondimensional droplet contribution to the second extensional viscosity. Note that $\tilde{\eta}_p = \eta_{ext}/\eta_c - 4$, and $\tilde{\eta}_2 = \eta_{cross}/\eta_c - 2$.

Henceforward in this work, the tilde superscripts will be suppressed from the nondimensional variables in order to alleviate the notation unless otherwise stated.

2.4 Emulsion magnetization assessment

The bulk magnetization of the system can be obtained by applying a volume-averaging technique to the magnetization field over the system domain. Note that the bulk magnetization of the system is equivalent to the magnetization of a ferrofluid emulsion of the corresponding volume fraction. As $\boldsymbol{M} = (\zeta(\boldsymbol{x}) - 1)\boldsymbol{H}$, the bulk magnetization, $\langle \boldsymbol{M} \rangle$, is given by

$$\langle \boldsymbol{M} \rangle = \frac{1}{V} \int_V (\zeta(\boldsymbol{x}) - 1)\, \boldsymbol{H}\, \mathrm{d}V. \tag{2.25}$$

2.5 Droplet's configuration assessment

In steady situations ($Ca < Ca_c$) the droplet always assumes an ellipsoidal shape. For the cases in which the semi-axes of the droplet remain aligned with the coordinate axes, we define one deformation parameter for each orthogonal plane based on the Taylor approach (TAYLOR, 1934). Figure 2.3 illustrates how they are measured. They are D_{xy}

for the deformation in the xy plane, D_{xz} for the deformation in the xz plane, and D_{zy} for the deformation in the zy plane. They are given by

$$D_{xy} = \frac{L_x - L_y}{L_x + L_y}, \quad D_{xz} = \frac{L_x - L_z}{L_x + L_z}, \quad \text{and} \quad D_{zy} = \frac{L_z - L_y}{L_z + L_z}, \tag{2.26}$$

where L_x is the semi-axis length in the x direction, L_y is the semi-axis length in the y direction, and L_z is the semi-axis length in the z direction.

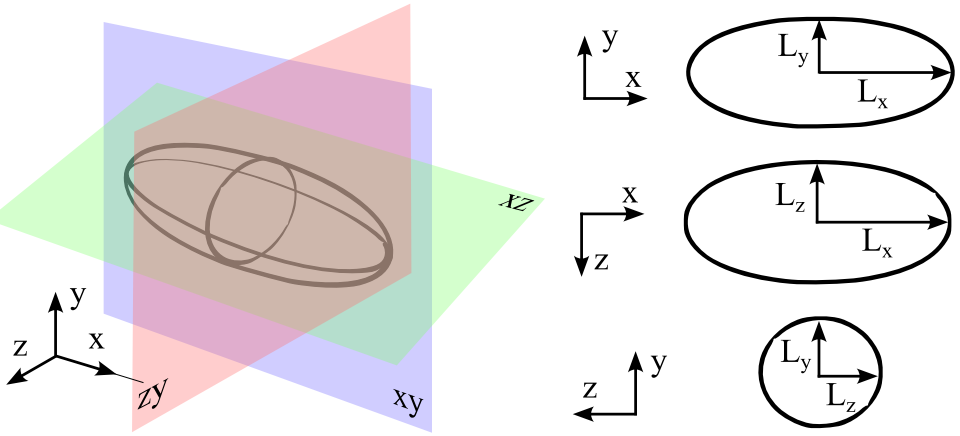

Figure 2.3 – Illustrative scheme of a deformed droplet and the orthogonal planes passing through the droplet centroid (left). Respective intersections between the planes and the droplet surface (right). L_x, L_y, and L_z are the droplet's semi-axes lengths in the x, y, and z direction, respectively.

In the cases in which there are two semi-axes laying in the extension plane (xy plane) without being in the x and y direction, and the other semi-axis in the z direction, we use the standard Taylor's deformation, D, given by

$$D = \frac{L - B}{L + B}, \tag{2.27}$$

where L and B are the lengths of the semi-major and semi-minor axes laying in the extension plane, respectively. In that case, the semi-major axis makes an angle θ with the extension direction (x direction).

Two distinct methods are used to obtain the ellipsoid semi-axes. In the cases in which the droplet remains symmetric with respect to the reference axes, the semi-axes, L_x, L_y, and L_z are evaluated using a search of the location of the droplet tips (the location of the surface central portion in each direction). L and B are evaluated using the eigenvalues and eigenvectors of the inertia tensor of the droplet (ellipsoid).

2.6 Critical capillary number assessment

The approach used here to estimate Ca_c is a searching procedure, in the way that for each case a series of simulations departing from rest is performed by taking step

changes in Ca until the breakup is observed. More precisely, we proceed as summarized in Algorithm 1, where Ca_s refers to the last steady result, the subcritical capillary number, Ca_p is the Ca of the first observed breakup, and ΔCa is the step change in Ca.

Algorithm 1 Ca_c assessment

1: Start with $Ca = 0.01$ (this is sufficient to ensure a steady configuration in the range of parameters studied here)
2: **while** breakup is not observed **do**
3: $Ca_s \leftarrow Ca$ (attribute Ca to Ca_s)
4: $Ca \leftarrow Ca + \Delta Ca$ (do an increment in Ca)
5: Perform simulation with Ca
6: **end while**
7: $Ca_p \leftarrow Ca$ (attribute the Ca of observed breakup to Ca_p)
8: $Ca_c = (Ca_s + Ca_p)/2 \pm \Delta Ca/2$

Note that with this procedure, we have a band of width ΔCa in which the transition from a stable to an unstable droplet is expected to occur. However, we do say that $(Ca_s + Ca_p)/2$ is the critical capillary number, keeping in mind that it is in fact the mean value of a band of width ΔCa.

In our study, we set $\Delta Ca = 0.01$. So if we say, for instance, that $Ca_c = 0.105$, the last stable condition was $Ca_s = 0.1$, and the first unstable condition was $Ca_p = 0.11$. We believe that the chosen ΔCa is small enough to ensure accuracy, and great enough to incorporate any numerical error and to keep the computational cost more affordable. The criterion for determining if the droplet achieves steady is explained in Sec. 3.5.

3 Numerical formulation

3.1 Spatial discretization

In this work, the governing equations are discretized using finite-difference schemes. Due to the simplicity of the geometry (a lattice), a staggered grid, also called Marker-and-Cell (MAC) grid, is used for domain discretization. In this arrangement, the scalar variables are evaluated at the center of the grid cells, while the components of the vector variables are evaluated at the respective cell faces. The usual index connectivity for a uniform rectilinear grid is used, where $i = 0, 1, 2, ..., N_x$; $j = 0, 1, 2, ..., N_y$; and $k = 0, 1, 2, ..., N_z$ corresponds to the $C_{i,j,k}$ cell grid of the lattice discretized in (N_x, N_y, N_z) elements for each, respective, x, y and z direction. The grid spacing in each direction is then given by $\Delta x = S_x/N_x$, $\Delta y = S_y/N_y$, and $\Delta z = S_z/N_z$. In our simulations, we choose N_x, N_y, and N_z so the cells are cubic with a grid spacing h, where $h = \Delta x = \Delta y = \Delta z$. Fig. (3.1) illustrates, for instance, the $C_{i,j}$ cell grid and the positioning of variables for a two-dimensional domain, where $\Phi_{i,j}$ is a scalar field, and $u_{i,j}$ and $v_{i,j}$ are the x and y components of a vector field, respectively. In practice, in our three-dimensional domain, we have four grids. One for the scalar fields (the main grid), and one for each vector fields components, each one staggered in each respective direction by $h/2$ in relation to the main grid.

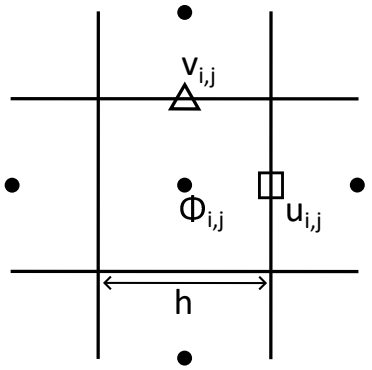

Figure 3.1 – $C_{i,j}$ and its neighboring cells for a two-dimensional staggered grid. Φ, a generic scalar field, is evaluated at the cell center. The vector components of a generic vector field, u and v, are evaluated at the cell face which points normal to their respective positive directions. h is the grid spacing in both x, and y direction.

The great advantage of this arrangement is that central difference schemes can

be obtained with a reduced stencil when compared to a regular co-located arrangement (cell-centered) when we evaluate the spatial derivative of a scalar variable that belongs to a vectorial equation, and vice versa. Whilst a central difference in a co-located grid would require a $(2\Delta x)$ stencil, it requires only a (Δx) stencil for a MAC grid. Consider, for example, the discrete spatial derivative with central differences of u when discretizing the equation for Φ. In a regular grid, the discrete operator would be

$$\left(\frac{\partial u}{\partial x}\right)_{i,j} = \frac{u_{i+1,j} - u_{i-1,j}}{2\Delta x} + O(4\Delta x^2), \tag{3.1}$$

while in a MAC grid, it reads

$$\left(\frac{\partial u}{\partial x}\right)_{i,j} = \frac{u_{i,j} - u_{i-1,j}}{\Delta x} + O(\Delta x^2). \tag{3.2}$$

It is worth noting that both approximations are second-order. The second, however, is more accurate due to the reduced stencil (half of that of the first case).

The derivative $\partial^2 u/\partial x^2$ in the u equation as well as $\partial^2 \Phi/\partial x^2$ in the Φ equation can be approximated by

$$\left(\frac{\partial^2 \Psi}{\partial x^2}\right)_{i,j} = \frac{(\partial \Psi/\partial x)_{i+1/2,j} - (\partial \Psi/\partial x)_{i-1/2,j}}{\Delta x} = \frac{\Psi_{i+1,j} - 2\Psi_{i,j} + \Psi_{i-1,j}}{(\Delta x)^2} \tag{3.3}$$

where Ψ is either a scalar or the component of a vector.

These central difference schemes, Eqs. (3.2) and (3.3), were used for the ordinary spatial derivatives in the Navier-Stokes equations (solved using the projection method explained in Sec. 3.2), such as $\nabla^2 \boldsymbol{u}^\star$ and $\nabla^2 \boldsymbol{u}^n$ in Eq. (3.7), ∇q^{n+1} in Eq. (3.8), and $\nabla^2 q^{n+1}$ and $\nabla \cdot \boldsymbol{u}^\star$ in Eq. (3.9). When the use of Eq. (3.2) is not possible, as in $\nabla \boldsymbol{H}$ present in the magnetic force term, the approximation given by Eq. (3.1) is used. The derivatives $\nabla \cdot (\zeta(\boldsymbol{x}) \nabla \psi)$ and $\nabla \cdot (\eta(\boldsymbol{x}) \nabla \boldsymbol{u})$ are evaluated using a similar approximation as Eq. (3.3). For example, in $\nabla \cdot (\zeta(\boldsymbol{x}) \nabla \psi)$ we have that

$$\left[\frac{\partial}{\partial x}\left(\zeta(\boldsymbol{x})\frac{\partial \psi}{\partial x}\right)\right]_{i,j} = \frac{1}{\Delta x}\left[\zeta(\boldsymbol{x})_{i+1/2,j}\left(\frac{\psi_{i+1,j} - \psi_{i,j}}{\Delta x}\right) - \zeta(\boldsymbol{x})_{i+1/2,j}\left(\frac{\psi_{i,j} - \psi_{i-1,j}}{\Delta x}\right)\right] \tag{3.4}$$

It is important to point out that some cases require the interpolation of a variable to match with the grid it is being evaluated. The H_y, for example, needs to be evaluated in the x component grid when solving the u_x equation. To do this, we use a four-point linear interpolation as $H_{y;i,j} \approx 0.25(H_{y;i,j} + H_{y;i+1,j} + H_{y;i,j+1} + H_{y;i+1,j})$. Interpolation is also necessary for evaluating scalar variables at midpoints between cell grids such as $\zeta(\boldsymbol{x})_{i+1/2,j}$ in Eq. (3.4). In this case, an harmonic mean is used, giving

$$\frac{2}{\zeta(\boldsymbol{x})_{i+1/2,j}} = \frac{1}{\zeta(\boldsymbol{x})_{i,j}} + \frac{1}{\zeta(\boldsymbol{x})_{i-1,j}} \tag{3.5}$$

The harmonic mean ensures appropriate computation of fluxes near the interface, where the variable changes considerably (PATANKAR, 2018). It is also used to interpolate $\eta(\boldsymbol{x})$.

Unlike the other derivatives, the advection term $(\boldsymbol{u} \cdot \nabla \boldsymbol{u})$ is discretized using a second-order essentially non-oscillatory (ENO) scheme with upwind, as presented in (OSHER; FEDKIW, 2006). This scheme consists of high-degree polynomial interpolation involving the upwind nodes, which guarantees proper computation near discontinuities.

The von Neumann boundary conditions are applied with the use of ghost grid points outside the solution domain. Due to the staggered grid, some vector components coincide with the domain boundary in a specific direction, while others do not. For Dirichlet boundary conditions of components that do not match the domain boundary, ghost grid points are also used.

3.2 Projection method

The Navier-Stokes equations can be numerically integrated in time by using second-order explicit Adams-Bashforth schemes for the convective, pressure, and source terms while using second-order implicit Crank-Nicolson scheme for the viscous term. Considering first the case of uniform viscosity, the application of this approximation in Eq. (2.13) results in

$$\frac{\boldsymbol{u}^{n+1} - \boldsymbol{u}^n}{\Delta t} = -\nabla p^{n+1/2} - (\boldsymbol{u} \cdot \nabla \boldsymbol{u})^{n+1/2} + \frac{1}{2Re}(\nabla^2 \boldsymbol{u}^{n+1} + \nabla^2 \boldsymbol{u}^n) + \boldsymbol{F}^{n+1/2}, \tag{3.6}$$

where $\boldsymbol{F}$ stands for the nondimensional magnetic and capillary force terms and Δt is the time-advancing step and the superscript denotes the time level. The pressure field, however, is unknown. The continuity equation, i.e., the free divergence constraint, Eq. (2.12), can be used to give an additional equation for the pressure field in order to solve the problem. In this work, we perform the pressure-velocity coupling of the unsteady incompressible Navier-Stokes equations by using the projection method of Kim and Moin (1985).

This method consists of splitting the time-advancement scheme into two steps as follows:

$$\frac{\boldsymbol{u}^\star - \boldsymbol{u}^n}{\Delta t} = -(\boldsymbol{u} \cdot \nabla \boldsymbol{u})^{n+1/2} + \frac{1}{2Re}(\nabla^2 \boldsymbol{u}^\star + \nabla^2 \boldsymbol{u}^n) + \boldsymbol{F}^{n+1/2}, \tag{3.7}$$

and

$$\frac{\boldsymbol{u}^{n+1} - \boldsymbol{u}^{\star}}{\Delta t} = -\nabla q^{n+1}, \tag{3.8}$$

where $\boldsymbol{u}^{\star}$ is a provisional velocity field that corresponds to the advanced velocity field that would be obtained with Eq. (3.6) in the absence of the pressure term, and q^{n+1} is an auxiliary pressure field. $\boldsymbol{F}^{n+1/2}$ is obtained by the extrapolation from previous values as $\boldsymbol{F}^{n+1/2} = 1.5\boldsymbol{F}^{n} - 0.5\boldsymbol{F}^{n-1}$, and so is the convective term $(\boldsymbol{u} \cdot \nabla \boldsymbol{u})^{n+1/2}$. Taking the divergence of Eq. (3.8) and applying the divergence constraint to $\boldsymbol{u}^{n+1}$ we get the following Poisson's equation for q^{n+1}:

$$\nabla^2 q^{n+1} = \frac{1}{\Delta t} \boldsymbol{\nabla \cdot u}^{\star} \tag{3.9}$$

The advancing algorithm is then summarized as follows: (1) find the provisional velocity $\boldsymbol{u}^{\star}$ using Eq. (3.7), (2) solve the Poisson's equation for the auxiliary pressure field q^{n+1} using Eq. (3.9), and (3) compute the advanced velocity $\boldsymbol{u}^{n+1}$ using Eq. (3.8). Note that the actual pressure field p is different from q. It can be determined, if required, by

$$p^{n+1/2} = q^{n+1} + \frac{\Delta t}{2Re} \nabla^2 q^{n+1}. \tag{3.10}$$

This relation is obtained by summing Eqs (3.7) and (3.8), and comparing the result with Eq. (3.6).

In order to solve these four partial differential equations (three Helmholtz equations for the provisional velocity components, and a Poisson's equation for the auxiliary pressure), appropriate boundary conditions must be used. The boundary condition for $\boldsymbol{u}^{\star}$ can be obtained by using Eq. (3.8), the boundary condition for $\boldsymbol{u}$ [Eq. (2.9)], and the extrapolation $q^{n+1} = 2q^{n} - q^{n-1}$. Since the boundary condition for auxiliary pressure is arbitrary, the homogeneous von Neumann condition is set ($\partial q^{n+1}/\partial n = 0$) as it facilitates the computation of the boundary conditions of $\boldsymbol{u}^{\star}$.

In the case of variable viscosity, i.e., $\lambda \neq 1$, the semi-implicit treatment used above applied to viscous term $\frac{1}{Re}\nabla \cdot [\eta(\boldsymbol{x})(\nabla \boldsymbol{u} + \nabla \boldsymbol{u}^{T})]$ would lead to variable coefficients when the corresponding Helmholtz equations are discretized, which, in turn, would require additional computational effort to recalculate the coefficients in each time step. To overcome this problem we use the semi-implicit treatment of the viscous term proposed in the work of Badalassi, Ceniceros and Banerjee (2003). The treatment consists in extrapolating the true viscous term, as did with the convective and body force terms, while adding to the first step of the projection method the term $\frac{1}{2Re}(\nabla^2 \boldsymbol{u}^{\star} + \nabla^2 \hat{\boldsymbol{u}}^{n+1})$, with $\hat{\boldsymbol{u}}^{n+1}$ extrapolated from previous values as $\hat{\boldsymbol{u}}^{n+1} = 2\boldsymbol{u}^{n} - \boldsymbol{u}^{n-1}$. In this case ($\lambda \neq 1$), the first step of the method, Eq. (3.7), is replaced for

$$\frac{\boldsymbol{u}^\star - \boldsymbol{u}^n}{\Delta t} = -(\boldsymbol{u}\cdot\nabla\boldsymbol{u})^{n+1/2} + \frac{1}{Re}\nabla\cdot[\eta(\boldsymbol{x})(\nabla\boldsymbol{u}+\nabla\boldsymbol{u}^T)]^{n+1/2} + \frac{1}{2Re}(\nabla^2\boldsymbol{u}^\star + \nabla^2\hat{\boldsymbol{u}}^{n+1}) + \boldsymbol{F}^{n+1/2}, \tag{3.11}$$

while the subsequent steps remain the same.

3.3 Level-Set method

Numerical computation of multiphase flows requires an accurate prediction of the location of the interface, as well as appropriate boundary conditions therein. Several methods have been developed since the middle of the last century. They can be categorized with respect to the way the interfaces are represented and advected. The applicability, accuracy, conservation properties, and easiness in computing geometrical quantities such as curvature are key features in choosing the appropriate method for a given problem. There are two main categories of numerical methods used to treat interfaces: *tracking methods* and *capturing methods*.

In the tracking methods, either the phase's volume regions (volume-tracking) or the sharp interface between them (front-tracking) are represented by placing markers in their location and advecting them in a Lagrangean manner. In the capturing methods, the interface location is defined implicitly in an Eulerian grid by the contour of a scalar function and it is advected naturally through an advection equation. Both classes of interface methods are used in numerical studies on droplet dynamics. Examples of works using the *boundary integral* (tracking) method are Loewenberg and Hinch (1996) and Oliveira and Cunha (2011). Examples of works using the *phase-field* (capturing) method are Ishida and Matsunaga (2020) and Ishida *et al.* (2022). Examples of works using the *Level-Set* (LS) (capturing) method are Cunha *et al.* (2020), Abicalil *et al.* (2021), and Abdo *et al.* (2023). There are also hybrid approaches, such as the hybrid LS-Volume-of-Fluid method (this latter is a tracking method). An example of this method in droplet dynamics research is Capobianchi *et al.* (2021). The method used to treat the interface in this work is a variation of the Level-Set method of Sussman, Smereka and Osher (1994).

In this method, the interface is represented by a level set of a higher-dimension scalar function $\phi(\boldsymbol{x}, t)$. The signed distance function with the interface implicitly described by its zero level is a common choice due to the easiness of computing geometrical quantities of the level set contour, i.e., of the interface. In the case of a droplet of one liquid immersed in another liquid, let Γ be the closed surface in R^3 that represents the interface between the inner region Ω^- (dispersed phase) and the outer region Ω^+ (continuous phase), and $d = |\boldsymbol{d}| = |\boldsymbol{x} - \boldsymbol{x}_\Gamma|$ be the magnitude shortest euclidean distance between $\boldsymbol{x}$ and Γ (see Fig. 3.2). The Level-Set function is thus defined over the whole computational domain by

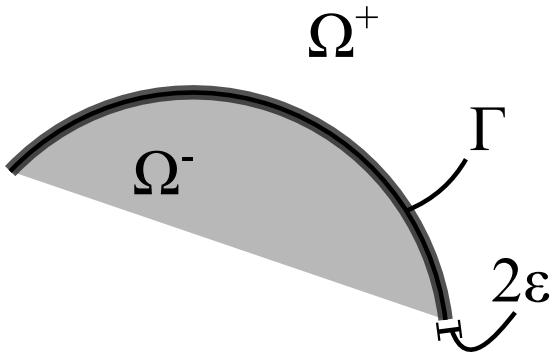

Figure 3.2 – Illustrative scheme of the important regions in the Level-Set framework (not to scale). In our case, the region Ω^- refers to the region inside the droplet, Ω^+ to the continuous phase, and Γ to the interface between both phases. 2ε refers to the interface thickness.

$$\phi(\boldsymbol{x},t) = \begin{cases} -d, \text{ if } & \boldsymbol{x} \in \Omega^-, \\ +d, \text{ if } & \boldsymbol{x} \in \Omega^+, \\ 0, \text{ if } & \boldsymbol{x} \in \Gamma. \end{cases} \tag{3.12}$$

As ϕ clearly does not vary in the tangential direction from Γ, its gradient points out in the normal direction to the interface. Then, the interface unit normal pointing outward Ω^-, $\hat{\boldsymbol{n}}$, is easily computed by

$$\hat{\boldsymbol{n}} = \frac{\nabla\phi}{|\nabla\phi|} \tag{3.13}$$

From differential geometry, the signed mean curvature is naturally given by

$$\kappa = \boldsymbol{\nabla} \cdot \hat{\boldsymbol{n}} \tag{3.14}$$

Note that these quantities are defined not only at $\phi = 0$ but at level sets.

3.3.1 Level-Set function

The movement of the interface is naturally given by the advection of ϕ due to the flow velocity, $\boldsymbol{u}$, by

$$\frac{\partial\phi}{\partial t} + \boldsymbol{u} \cdot \nabla\phi = 0. \tag{3.15}$$

Note that for a material point $D\phi/Dt = 0$, thus the interface $\phi = 0$ is preserved. Although the interface is well advected, nothing guarantees that ϕ remains as a signed distance function (i.e., $|\nabla\phi| \neq 1$) as it evolves in time, and it is indeed the general case [see, for instance, the work of Sussman, Smereka and Osher (1994)]. For that reason, a *reinitialization* procedure must be used when ϕ ceases to be a signed-distance function

in order to *redistance* the Level-Set field, and so, guarantee the proper computation of the geometrical quantities. We present the reinitialization procedure used in this work in Sec. 3.3.4.

3.3.2 Interface thickness and smoothed functions

The Level-Set method treats the interface no longer as sharp. Instead, it defines an interface thickness equal to 2ε where there is a smooth transition of the physical properties between the phases (see Fig. 3.2). This treatment is necessary in order to mitigate the numerical instabilities that would occur due to abrupt changes in the physical properties in the discrete domain. Furthermore, the spatial delta function would fail to impose the correct capillary force in the interface regions where the interface location does not exactly match the grid points. In this work, we take the typical value of $\varepsilon = 1.5h$ (OSHER; FEDKIW, 2006). Note that this finite representation can be made naturally from the signed distance function since this region is easily defined by $|\phi| \leq \varepsilon$.

The smooth transition of properties between the phases is made by using the smoothed version of the Heaviside function as an interpolator. The smoothed Heaviside function, $\mathcal{H}_\varepsilon$, is given by

$$\mathcal{H}_\varepsilon(\phi) = \begin{cases} 0, \text{ if } & \phi < -\varepsilon, \\ \frac{1}{2}\left[1 + \frac{\phi}{\varepsilon} - \frac{1}{\pi}\sin\left(\frac{\pi\phi}{\varepsilon}\right)\right], \text{ if } & |\phi| \leq \varepsilon, \\ 1, \text{ if } & \phi > \varepsilon. \end{cases} \tag{3.16}$$

So a physical property $\Psi(\boldsymbol{x})$ that changes sharply from its value at the continuous phase, Ψ_c, to the value at the dispersed phase, Ψ_d, can be substituted to a smoothed version $\Psi_\varepsilon(\phi)$ through $\Psi_\varepsilon(\phi) = \Psi_c\mathcal{H}_\varepsilon(\phi) + [1 - \mathcal{H}_\varepsilon(\phi)]\Psi_d$. In this work, the physical properties $\zeta(\boldsymbol{x})$ and $\eta(\boldsymbol{x})$ are replaced for their smoothed versions $\zeta_\varepsilon(\phi)$ and $\eta_\varepsilon(\phi)$, recalling that $\phi = \phi(\boldsymbol{x}, t)$.

Following the definition of $\mathcal{H}_\varepsilon$, we can define a smoothed one-dimensional Dirac function, $\delta_\varepsilon(\phi)$, by taking $\delta_\varepsilon(\phi) = \frac{d}{d\phi}\mathcal{H}_\varepsilon(\phi)$. It gives

$$\delta_\varepsilon(\phi) = \begin{cases} \frac{1}{2\varepsilon}\left[1 + \cos\left(\frac{\pi\phi}{\varepsilon}\right)\right], & \text{if } |\phi| \leq \varepsilon, \\ 0, & \text{otherwise.} \end{cases} \tag{3.17}$$

The spatial (sharp) Dirac function, $\hat{\delta}(\boldsymbol{d})$, is related to $\delta_\varepsilon(\phi)$ by

$$\hat{\delta}(\boldsymbol{d}) = \delta_\varepsilon(\phi)|\nabla\phi|. \tag{3.18}$$

In Eq. (3.18), we made use of Eq. (3.13), and the fact that $\hat{\delta}(\boldsymbol{x}) = \nabla\mathcal{H}(\boldsymbol{x}) \cdot \hat{\boldsymbol{n}}$, $\nabla\mathcal{H}(\boldsymbol{x}) = \mathcal{H}'(\phi)\nabla\phi$, and $\delta(\phi) = \mathcal{H}'(\phi)$. Substituting Eq. (3.18) in the nondimensional capillary term of Eq. (2.13), we get the capillary force term in the Level-Set framework:

$$\boldsymbol{F_c} = -\frac{1}{ReCa}\kappa\delta_\varepsilon(\phi)|\nabla\phi|\hat{\boldsymbol{n}}. \tag{3.19}$$

3.3.3 Volume and surface integrals

In order to evaluate volume integrals over the region bounded by the interface, or surface integrals over the interface in the Level-Set framework, it is necessary to use appropriate methods. To evaluate an arbitrary function of space $F(\boldsymbol{x})$ over the region Ω^-, i.e., in our case, over the volume of the droplet, we use

$$\int_{\Omega^-} F(\boldsymbol{x})dV = \int_V F(\boldsymbol{x})\mathcal{H}_\varepsilon(-\phi)dV, \tag{3.20}$$

where V is the entire domain. When $F(\boldsymbol{x}) = \boldsymbol{x}$, for example, we have the moment of inertia of the droplet. For surface integrals over the interface, we use

$$\int_\Gamma F(\boldsymbol{x})dS = \int_V F(\boldsymbol{x})\delta_\varepsilon(\phi)|\nabla\phi|dV. \tag{3.21}$$

Equation (3.21) is used when computing the particle stress, Eq. (2.22). In Eq. (3.21) we made use of the fact $\int_\Gamma F(\boldsymbol{x})dS = \int_V F(\boldsymbol{x})\hat{\delta}(\boldsymbol{x} - \boldsymbol{x_\Gamma})dV$, and the relation given by Eq. (3.18) (OSHER; FEDKIW, 2006). We use Eq. (3.21), for instance, to solve the droplet stress surface integral [Eq. (2.22)]. Numerically, these volume integrals are computed using a second-order quadrature in a 27-point cubic stencil. In other words, they are computed as the sum of the following integral over each grid cell $C_{i,j,k}$:

$$\int_{C_{i,j,k}} FdV = \frac{h^3}{78}\left(52F_{i,j,k} + \sum_{l=-1}^{1}\sum_{m=-1}^{1}\sum_{n=-1}^{1}\alpha_{l,m,n}F_{i+l,j+m,k+n}\right) \tag{3.22}$$

where $\alpha_{l,m,n} = 0$ if $l = m = n = 0$, and $\alpha_{l,m,n} = 1$ otherwise.

3.3.4 Reinitialization procedure

As discussed earlier, we need to reinitialize the Level-Set function when it starts to deviate from a signed distance function. A naive procedure would be remeasuring the smaller distance from $\boldsymbol{x}(\phi = 0)$ at all points throughout the domain at each time step, however, it would need complex algorithms to explicitly find the interface location and large computational cost. Sussman, Smereka and Osher (1994) suggested a more efficient approach that consists in reaching a steady state on the following initial value problem:

$$\frac{\partial \phi}{\partial \tau} + sgn(\phi_0)(|\nabla \phi| - 1) = 0 \tag{3.23}$$

$$\phi(\boldsymbol{x}, 0) = \phi_0(\boldsymbol{x}) \tag{3.24}$$

where τ is a fictitious time, ϕ_0 is the initial Level-Set function resulting from advancing Eq. (3.15) in time (supposed to be close to a distance function), and $sgn(\phi_0) = \phi_0/\sqrt{\phi_0^2 + |\nabla\phi|^2\varepsilon^2}$ is a smoothed sign function. Note that Eq. (3.23) conserves ϕ at the interface so that the zero level set is unchanged through the reinitialization procedure. The numerical solution of Eq. (3.23), however, can lead, and generally does, to undesired displacements of the zero level set due to numerical errors related to the discretization. For the problem of a droplet dispersed in a continuous media, it would mean undesired displacements of the droplet's interface and, hence, nonphysical variations of the droplet's volume.

In order to overcome this problem, Sussman and Fatemi (1999) proposed the application of a volume constraint to Eq. (3.23) for incompressible viscous-driven multiphase flows. It consists of the addition of a source term that could balance the possible undesired convection of the interface. This correction term is given by ensuring that the volume of the region Ω^- is unchanged. It means that

$$\frac{\partial}{\partial \tau} \int_\Omega \mathcal{H}_\varepsilon(\phi) dV = 0. \tag{3.25}$$

Giving to the source term the form $\gamma f(\phi)$, where $f(\phi)$ is an arbitrary function and the parameter γ is a function of time, we fall on the following correction equation

$$\frac{\partial \phi}{\partial \tau} + \mathcal{L}(\phi, \phi_0) = \gamma f(\phi), \tag{3.26}$$

where

$$\mathcal{L}(\phi, \phi_0) = sgn(\phi_0)(|\nabla \phi| - 1). \tag{3.27}$$

Noting that the integration region in Eq. (3.25) does not depend on τ, and using Eq. (3.26), we have that

$$\frac{\partial}{\partial \tau} \int_\Omega \mathcal{H}_\varepsilon(\phi) dV = \int_\Omega \mathcal{H}'_\varepsilon(\phi) \frac{\partial \phi}{\partial \tau} dV = \int_\Omega \mathcal{H}'_\varepsilon(\phi)[\gamma f(\phi) - \mathcal{L}(\phi, \phi_0)] dV = 0 \tag{3.28}$$

From Eq. (3.17) we know that $\mathcal{H}'_\varepsilon(\phi) = \delta_\varepsilon(\phi)$. We can now separate γ by assuming its constancy in space. The arbitrary function $f(\phi)$ can be the spatial delta function $f(\phi) = \delta_\varepsilon(\phi)|\nabla\phi|$, since we need to apply the correction only at the interface (OSHER; FEDKIW, 2006). γ is then given by

$$\gamma = \frac{\int_\Omega \delta_\varepsilon(\phi)\mathcal{L}(\phi,\phi_0)dV}{\int_\Omega \delta_\varepsilon^2(\phi)|\nabla\phi|dV}. \tag{3.29}$$

When solving this correction scheme, the domain Ω is set as an individual grid cell, $C_{i,j,k}$, so that any undesired interface displacement is corrected locally. Note that this procedure does not affect the derivation above.

3.4 Solution of the numerical formulation

3.4.1 Level-Set function solving

The Level-Set equation [Eq. (3.15)] and the reinitialization equation [Eq. (3.26)] are hyperbolic. They are solved with a conservative Gudonov's method in which the spatial derivatives are discretized using a fifth-order weighted essentially nonoscillatory (WENO) scheme (JIANG; PENG, 2000). This scheme involves the use of a weighted combination of the possible approximations of the ENO scheme and can increase the order of approximation up to fifth-order [the reader is referred to (OSHER; FEDKIW, 2006) for further explanation of the scheme and its numerical implementation]. In time, the equations are integrated using a third-order strong stability preserving (SSP) Runge-Kutta scheme (GOTTLIEB; KETCHESON; SHU, 2011).

3.4.2 Construction of the linear systems

All the elliptic equations are solved either implicitly, such as the magnetic potential equation [Eq. (2.7)] and the auxiliary pressure equation [Eq. (3.9)], or semi-implicitly, such as the provisional velocity components equations [Eq. (3.11)]. When discretized, these equations assume the form of sevendiagonal linear systems. Note that, for the provisional velocity components equations, this is possible due to the explicit treatment of the convective terms. The linear system for the equation of a generic variable Φ reads

$$\boldsymbol{A}\boldsymbol{\Phi} = \boldsymbol{h}, \tag{3.30}$$

where $\boldsymbol{A}$ is the coefficient matrix, $\boldsymbol{\Phi}$ is the Φ array, and $\boldsymbol{h}$ corresponds to the right-hand side of the equation, i.e., the source terms.

As commented in Sec. 3.1, the connectivity between the grid points is directly associated with the cell indices (i,j,k) due to the rectilinear structure. Then, the coefficient matrix can be described as a set of three-dimensional arrays, one for the diagonal, and each other related to each neighbor cell:

$$
\begin{aligned}
a_{i,j,k}\Phi_{i-1,j,k} + b_{i,j,k}\Phi_{i,j-1,k} + c_{i,j,k}\Phi_{i,j,k-1} + d_{i,j,k}\Phi_{i,j,k} \\
+ e_{i,j,k}\Phi_{i+1,j,k} + f_{i,j,k}\Phi_{i,j+1,k} + g_{i,j,k}\Phi_{i,j,k+1} = h_{i,j,k}.
\end{aligned}
\tag{3.31}
$$

To illustrate the process of obtaining the coefficient arrays, consider the auxiliary pressure equation [Eq. (3.9)]. Applying the discrete spatial derivative operator [Eq. (3.2)] to this Poisson's equation and rearranging yields

$$
\begin{aligned}
&\left(\frac{1}{\Delta x}\right) q_{i+1,j,k} + \left(\frac{1}{\Delta y}\right) q_{i,j+1,k} + \left(\frac{1}{\Delta z}\right) q_{i,j,k+1} - \left(\frac{2}{\Delta x} + \frac{2}{\Delta y} + \frac{2}{\Delta z}\right) q_{i,j,k} \\
&\quad + \left(\frac{1}{\Delta x}\right) q_{i-1,j,k} + \left(\frac{1}{\Delta y}\right) q_{i,j-1,k} + \left(\frac{1}{\Delta z}\right) q_{i,j,k-1} \\
&\quad = \left[\frac{u^{\star}_{i,j,k} - u^{\star}_{i-1,j,k}}{\Delta x} + \frac{v^{\star}_{i,j,k} - v^{\star}_{i,j-1,k}}{\Delta y} + \frac{w^{\star}_{i,j,k} - w^{\star}_{i,j,k-1}}{\Delta z}\right]
\end{aligned}
\tag{3.32}
$$

The coefficients arrays are thus obtained by direct comparison between the Eq. (3.32) and Eq. (3.31). These coefficient values are valid for cell points away from boundaries. For the cell points near or coincident with domain boundary points, boundary conditions are applied.

The numerical methods used for approximating the inverse of the coefficient matrix and computing $\Phi = \boldsymbol{A}^{-1}\boldsymbol{h}$ are briefly described in the following section.

3.4.3 Linear system solvers

In this work, all the linear systems are solved using the well-known iterative Conjugate Gradient method, but with different preconditioning. The linear systems for $\boldsymbol{u}^{\star}$ are solved with Symmetric Successive Over-Relaxation (SSOR) as preconditioning, while the linear systems for q and ψ are solved with multigrid preconditioning [see (SAAD, 2003) for a detailed description of the conjugate gradient method and the preconditioning algorithms].

3.4.4 Solution algorithm

The nondimensional multiphase model described by the Eqs. (2.12)-(2.15) solves the problem described in Sec. 2.1 through the numerical methods presented in this chapter. The solution algorithm of the numerical model is summarized in Algorithm 2.

3.5 Numerical settings

The multiphase model described in this text was implemented in an in-house code written in *FORTRAN 95*©. Two different domain sizes, grid spacings, and time steps were

Algorithm 2 Solution algorithm

1: Read the simulation parameters from a configuration file (Re, Ca, Ca_{mag}, λ, ζ, magnetic field direction, domain length, grid parameters, etc.)
2: Initialize variables, including ϕ in accordance with the initial spherical shape of the droplet
3: **if** *ferrofluid droplet* **then**
4: Solve the magnetic potential ψ^1 [Eq. (2.14)]
5: Compute the magnetic field from the magnetic potential $\boldsymbol{H}^1$ [Eq. (2.15)]
6: **end if**
7: **for** $it = 1$ **to** nit **do**
8: Find the provisional velocity vector $\boldsymbol{u}^\star$ [Eq. (3.7) or Eq. (3.11)]
9: Find the auxiliary pressure field q [Eq. (3.9)]
10: Compute the true velocity field $\boldsymbol{u}^{it}$ [Eq. (3.8)]
11: Update the true pressure field p^{it} [Eq. (3.10)]
12: Advect the Level-Set function [Eq. (3.15)]
13: Reinitialize the Level-Set function [Eq. (3.26)]
14: **if** *ferrofluid droplet* **then**
15: Solve the magnetic potential ψ^{it+1} [Eq. (2.14)]
16: Compute the magnetic field from the magnetic potential $\boldsymbol{H}^{it+1}$[Eq. (2.15)]
17: **end if**
18: **end for**

used all over the simulations.

- For the simulations regarding the steady-state results of the droplet's configuration, and corresponding ferrofluid emulsion magnetization and rheology, the following settings were used: a domain size of $12.5 \times 10 \times 7.5$ ($\beta \approx 0.45\%$), a grid spacing length of $h = 0.062500$, and a time step of $\Delta t = 2 \times 10^{-3}$.

- For the simulations in which we are looking for the droplet breakup, the following settings were used: a domain size of $20.0 \times 10 \times 7.5$ ($\beta \approx 0.28\%$), a grid spacing length of $h = 0.078125$, and a time step of $\Delta t = 3 \times 10^{-3}$.

In the latter case, a larger domain was used because the droplet was expected to reach more elongated shapes. In order to balance the number of elements, given that searching for Ca_c requires a large number of simulations, a slightly coarser grid was used, and so was the time step. No grid tests were performed for this case, because the methodology used here for evaluating the parameter of interest, Ca_c, incorporates the numerical errors (see Sec. 2.6).

A grid independence test was performed to analyze the convergence of the variables and to guide the choice of the used grid spacing lengths. It is presented in Sec. 3.6.

The steady state is determined when the droplet distortion in the xy plane, D, changes in less than 0.5% between two consecutive units of dimensionless time. When

D does not reach the above criterion and continuously increases, a breakup situation is attributed to the case.

3.6 Grid independence test

In order to verify the accuracy of the numerical solutions for the steady-state cases, we performed a grid independence test for a representative case where $\lambda = 1$, $Ca = 0.02$, $Ca_{mag} = 20$, and the external magnetic field is applied in the x direction. The domain size is that of the steady cases, $12.5 \times 10 \times 7.5$ (see Sec. 3.5). We tested four different grids (termed G1 to G4) for which the number of cells along the longest side of the flow domain is set to 120, 160, 200, and 240, respectively; therefore, the total number of grid cells and the meshing size vary from ∼800,000 to ∼6,600,000 and from ∼0.1 to ∼0.05, respectively. In all cases, the time step is set to $\Delta t \approx 0.25h/\|\boldsymbol{u}_{max}\|$, where $\|\boldsymbol{u}_{max}\| \approx 8$ is the maximum flow velocity, as determined by the boundary condition and the domain size.

Table 1 summarizes the steady-state results for the droplet deformation in the xy plane, D_{xy}, the system bulk magnetization, $\langle M \rangle$, and the xx component of the first and second terms of the droplet stress, $\boldsymbol{\sigma}^d_{1,xx}$ and $\boldsymbol{\sigma}^d_{2,xx}$, respectively. As the refinement increases from grid G1 to grid G4, the results change in less than ∼1.2%, ∼0.7%, and ∼0.5%, respectively, demonstrating that the hydrodynamic, magnetic, and Level-Set variables indeed converge with the spatial discretization. We chose the G3 grid for the steady cases because the results change in less than ∼0.5% when compared to G4 at the cost of almost double the number of grid cells. Note that if the variables converge with this domain size, they should converge with a larger one, including that used in the breakup cases. Further, we see that the G2 can be used for that cases without losing significant accuracy.

In all simulations performed in this work, the divergence of the velocity field (the divergence constraint, $\nabla \cdot \boldsymbol{u} = 0$) is maintained below 10^{-10}.

Table 1 – Mesh convergence study in terms of the droplet distortion in the xy plane (D_{xy}), the system bulk magnetization ($\langle M \rangle$), and the xx component of the first and second terms of the particle stress ($\boldsymbol{\sigma}^d_{1,xx}$ and $\boldsymbol{\sigma}^d_{2,xx}$, both normalized by β). The results are for $Ca = 0.02$ and $Ca_{mag} = 20$ when the external magnetic field is applied in the x-direction.

Grid	Grid cells	Meshing size	D_{xy}	$\boldsymbol{\sigma}^d_{1,xx}/\beta$	$\boldsymbol{\sigma}^d_{2,xx}/\beta$	$\langle M \rangle$
G1	829,440	0.104167	0.5703	0.7723	-2.2728	0.004171
G2	1,966,080	0.078125	0.5765	0.7817	-2.2673	0.004151
G3	3,840,000	0.062500	0.5804	0.7869	-2.2649	0.004142
G4	6,635,520	0.052083	0.5835	0.7906	-2.2629	0.004138

4 Results and discussion

In this chapter, we present and discuss the main results of our numerical experiments. The discussion begins by examining the behavior of a ferrofluid droplet subjected to the isolated actions of either planar extensional flow or an external magnetic field. These initial results serve as a validation of our computational model. Once the model's validity is established, we proceed to investigate the impact of applying magnetic fields along each of the three flow main directions, assessing their effects on the emulsion microstructure, magnetization, and resulting rheology. Subsequently, we explore the scenario wherein the applied magnetic field deviates from the aforementioned directions. Finally, with a thorough analysis of a stable ferrofluid emulsion, we investigate the conditions of flow and magnetic field in which the breakup can be expected to occur. All results are for $Re = 0.01$, to be consistent with the inertia-free assumption (see Sec. 2.2.4), and $\zeta = 2$ ($\chi = 1$, see Sec. 2.1).

4.1 Isolated action of planar extension and magnetic field: code validation

In this section, we present the simulation results of two cases: a viscous droplet subjected to planar expansion flows and a ferrofluid droplet subjected to uniform external magnetic fields. The purpose here is to demonstrate the applicability of the proposed numerical model before proceeding to the general case in which ferrofluid droplets or corresponding ferrofluid emulsions are subject to both planar expansion flows and uniform magnetic fields. For this, measurements of the droplet distortion in the xy plane, D_{xy}, were compared with the experimental, numerical, and theoretical results present in the literature.

4.1.1 Droplet distortion in planar extensional flow

Figure 4.1 shows steady-state results of D_{xy} as a function of Ca for a viscous regular droplet of $\lambda = 1$ subjected to a planar extensional flow (defined in Section 2.1). We also present the experimental results of Hsu and Leal (2009) (measured in a four-roll mill

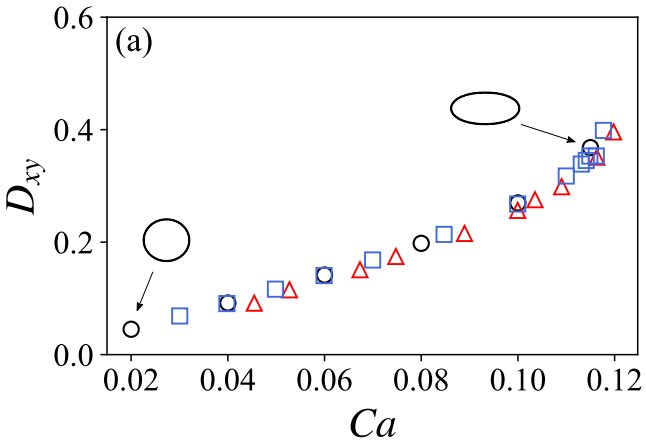

Figure 4.1 – Droplet distortion in the xy plane (D_{xy}) as a function of Ca with no external magnetic field ($Ca_{mag} = 0$) and $\lambda = 1$: present work (black circles), experimental results of Hsu and Leal (2009) (red triangles), and simulation results of Park *et al.* (2019) (blue squares). The insets show the droplet cross-section in the xy plane at $Ca = 0.02$ and $Ca = 0.115$. Adapted from (GUILHERME *et al.*, 2023, p. 6). © 2023 by American Physical Society.

apparatus) and the simulation results of Park *et al.* (2019) (measured with commercial software). The droplet is stretched in the x direction and, due to incompressibility, compressed in the other two directions with slightly different intensities: more in the y direction than in the z direction. As a result, the droplet assumes the shape of a prolate-like ellipsoid and distorts progressively as Ca increases. This progression is almost linear in the limit of low Ca, as predicted by the small deformation theory of Taylor (1934). As Ca increases, the droplet distortion becomes more pronounced. From above a certain value, in this case, around $Ca \approx 0.12$, the droplet surface at the central portion becomes "flat" (infinite curvature in the xy cross-section), and the droplet continuously distorts without achieving a steady state, in a process marked by the appearance of necking regions near the tips in the x axis. This process is called breakup here, as this behavior suggests that the droplet will eventually burst, although this was not observed for this case due to the limited computation domain length. Figure 4.2 shows the evolution of the droplet surface during the breakup process with $Ca = 0.12$, where we can see the droplet becoming flat at around $t \approx 7.50$. We provide a detailed analysis of the breakup process in the absence and in the presence of external magnetic fields in Sec. 4.4.

4.1.2 Magnetic field induced deformation with no external flow

Figure 4.3 shows steady-state results of D_{xy} as a function of Ca_{mag} for a ferrofluid droplet immersed in a quiescent liquid ($\boldsymbol{u}_\infty = \mathbf{0}$) subjected to an applied uniform magnetic field in the x direction. We also present the theoretical predictions of Afkhami *et al.* (2010) for the droplet shape at equilibrium with $\zeta = 2$. The external field induces a magnetic force normal to the droplet surface because the difference in magnetic permeability between

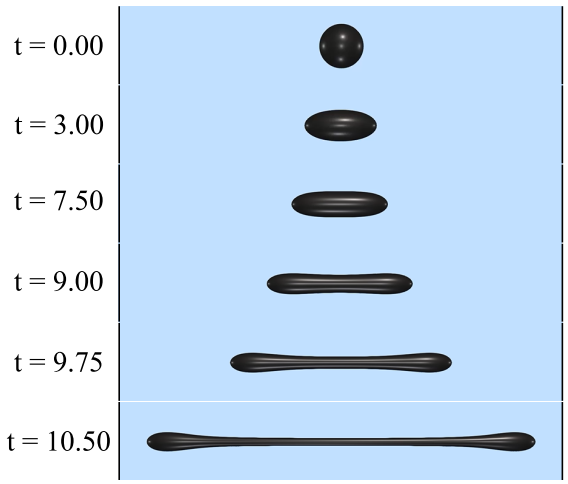

Figure 4.2 – Droplet shape evolution during breakup process with $Ca = 0.12$ and $\lambda = 1$. The domain size in the x direction for this case is $S_x = 20$. Its limits are denoted by the black vertical lines. At around $t \approx 7.5$, the droplet surface becomes flat in the xy plane at the central portion.

the phases leads to a magnetic field jump across the interface. This force is stronger in regions where the interface is perpendicular to the external field direction because the magnetic field points in the gradient direction. As a result, the droplet is stretched in the x direction, and, due to incompressibility, compressed in the other two directions with equal intensities, assuming a prolate ellipsoidal shape. The droplet reaches an equilibrium shape when the magnetic forces balance with the capillary forces so that its distortion progressively increases with Ca_{mag}. However, unlike the flow-induced distortion relation with Ca presented in Fig. (4.1), the rate of variation of D_{xy} with respect to Ca_{mag} decreases, characterizing a hardening-like response with Ca_{mag}. No breakup was observed in field-induced distortion for static fields, even in high field intensities, at least for $\chi = 1$.

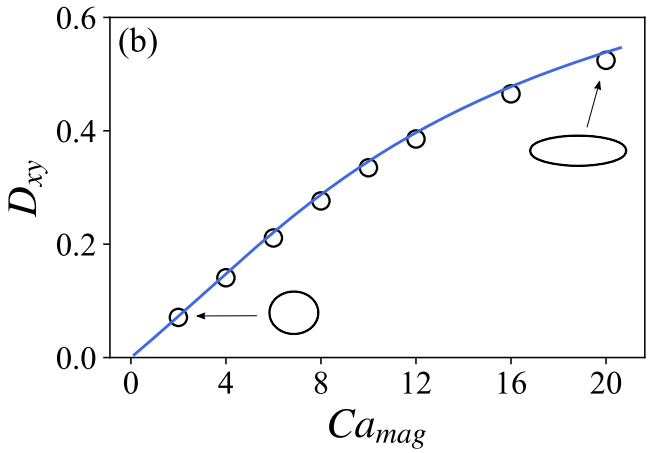

Figure 4.3 – Droplet distortion in the xy plane (D_{xy}) as a function of Ca_{mag} when the external magnetic field is applied in the x direction with no external flow ($\boldsymbol{u}_\infty = \mathbf{0}$) and $\chi = 1$: present work (black circles) and theoretical predictions of Afkhami *et al.* (2010) (blue line). The insets show the droplet cross-section in the xy plane at $Ca_{mag} = 2$ and $Ca_{mag} = 20$. Adapted from (GUILHERME *et al.*, 2023, p. 6). © 2023 by American Physical Society.

The agreement between current simulations and previous studies in the literature shown in this validation section confirms the reliability of our numerical model with respect to hydrodynamic, magnetic, and interfacial problems.

4.2 External field applied in one of the flow main directions

We now proceed with the analysis of the droplet deformation, magnetization, and emulsion rheology for the magnetic field applied in each of the flow main directions, i.e., $\boldsymbol{H_0} = \hat{\boldsymbol{e}}_{\boldsymbol{x}}$, $\boldsymbol{H_0} = \hat{\boldsymbol{e}}_{\boldsymbol{y}}$, and $\boldsymbol{H_0} = \hat{\boldsymbol{e}}_{\boldsymbol{z}}$. We explore Ca and Ca_{mag} in the ranges $0.02 \leq Ca \leq 0.12$, and $2 \leq Ca_{mag} \leq 20$.

4.2.1 Droplet deformation: emulsion microstructure

Figure 4.4 shows the droplet distortion in the xy plane, D_{xy}, as a function of Ca_{mag}. The results are for different values of Ca when the external magnetic field is applied in the x and y direction. We see that D_{xy} grows with Ca_{mag} when the external field is in the x direction [Fig. 4.4(a)]. Because viscous and magnetic forces stretch the droplet together in the same direction, the droplet assumes a prolate-like shape with the major axis in the x axis ($D_{xy} > 0$). This field-induced extension is slightly more pronounced in strong flows (high Ca). In turn, D_{xy} falls with Ca_{mag} when the external field is in the y direction [Fig. 4.4(b)]. Viscous and magnetic forces now compete to stretch the droplet in directions that are perpendicular to one another. Briefly, the field-induced extension

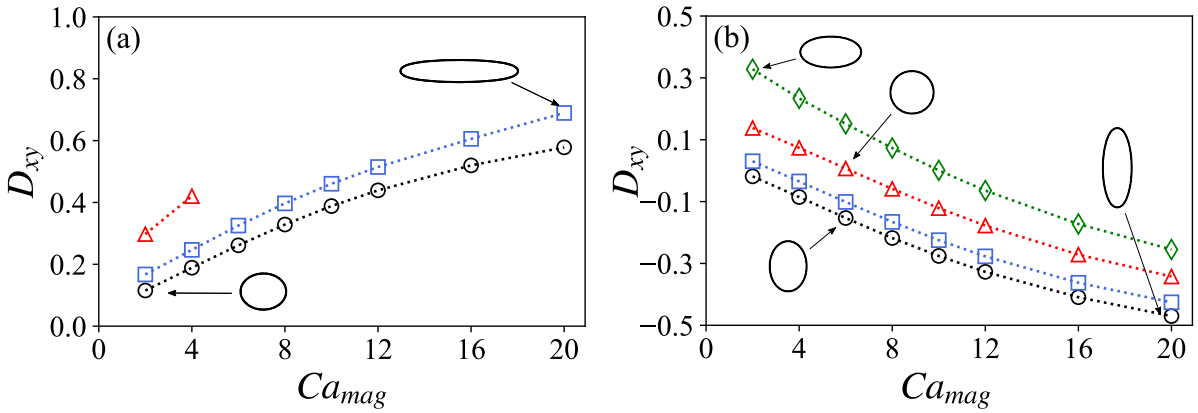

Figure 4.4 – Droplet distortion in the xy plane (D_{xy}) as a function of Ca_{mag} when the external magnetic field is applied in the (a) x direction and (b) y direction. The results are for $Ca = 0.02$ (black circles), $Ca = 0.04$ (blue squares), $Ca = 0.08$ (red triangles), and $Ca = 0.12$ (green diamonds). The insets show the droplet cross-section in the xy plane at different conditions. The data set is not complete in (a) because the droplet does not achieve a steady shape when $Ca = 0.08$ and $Ca_{mag} \geq 6$ and when $Ca = 0.12$ and $Ca_{mag} \geq 0$ [see the discussion for Fig. 4.1(a)]. Adapted from (GUILHERME *et al.*, 2023, p. 8). © 2023 by American Physical Society.

in the y direction is counteracted by flow-induced compression, whereas the flow-induced extension in the x direction is counteracted by field-induced compression. At low enough Ca_{mag}, viscous forces dominate over magnetic forces and the droplet major axis is in the x axis ($D_{xy} > 0$). As Ca_{mag} increases and the external field intensity grows stronger, magnetic forces eventually overtake viscous forces and the droplet major axis becomes aligned with the y axis ($D_{xy} < 0$). This field-induced shape transition is easier in weak flows (low Ca).

Figure 4.5 shows the droplet distortion as a function Ca_{mag} for different values of Ca when the external magnetic field is applied in the z direction. Note that we now plot D_{xy} and the deformation in the xz plane, D_{xz}. We observe that D_{xy} is a weak function of Ca_{mag} [Fig. 4.5(a)]. The field-induced compression in the x and y direction is approximately the same, particularly at low Ca [see the discussion for Fig. 4.1(b)]. Thus, the droplet distortion in the xy plane is mainly governed by the balance between viscous and capillary forces, as determined by Ca. Conversely, D_{xz} falls strongly with Ca_{mag} [Fig. 4.5(b)]. The competition between viscous and magnetic forces behind this field-induced shape transition — from $D_{xz} > 0$ with the droplet major axis in the x axis to $D_{xz} < 0$ with the droplet major axis in the z axis — is similar to that discussed for Fig. 4.4(b). The major difference here is that D_{xz} is a weaker function of Ca, especially at high Ca_{mag}, where all curves approach one another. This indicates that viscous forces play a minor role in the droplet distortion in the direction of the external magnetic field when the latter is sufficiently strong and aligned with the flow neutral direction.

Figures 4.4 and 4.5 suggest that the intensity and direction of external magnetic fields can be adjusted to either induce or prevent droplet breakup in planar extensional flows. We have seen that the droplet bursts at $Ca \approx 0.12$ in the absence of external field

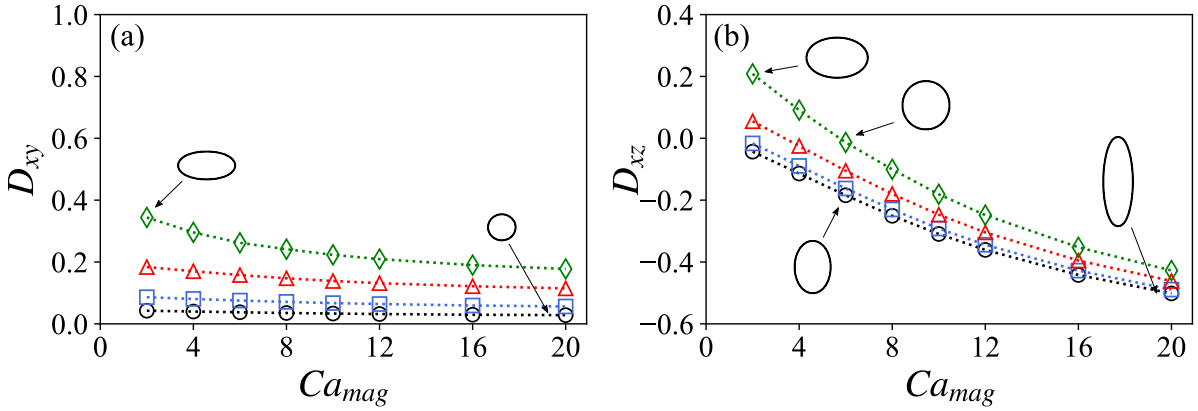

Figure 4.5 – Droplet distortion in the (a) xy plane (D_{xy}) and (b) xz plane (D_{xz}) as a function of Ca_{mag} when the external magnetic field is applied in the z direction. The results are for $Ca = 0.02$ (black circles), $Ca = 0.04$ (blue squares), $Ca = 0.08$ (red triangles), and $Ca = 0.12$ (green diamonds). The insets show the droplet cross-section in the (a) xy plane and (b) xz plane at different conditions. Adapted from (GUILHERME *et al.*, 2023, p. 8). © 2023 by American Physical Society.

($Ca_{mag} = 0$) [see the discussion for Fig. 4.1(a)]. Now, we find that when an external field is applied in the x direction with $Ca_{mag} = 6$, the droplet does not achieve a steady shape at $Ca \geq 0.08$, indicating that the droplet will eventually break up. On the other hand, we do observe steady shapes with no signs of droplet breakup at $Ca = 0.12$ when the external field is either in the y or z direction at $Ca_{mag} \geq 2$. In Section 4.4, we provide a detailed analysis of how the external magnetic field affects the breakup of ferrofluid droplets in planar extensional flows. For now, we are interested in the cases where the droplets achieve steady shapes.

4.2.1.1 Droplet spheroidizing

The field-induced shape transition presented in Figs. 4.4(b) and 4.5(b) also deserves special remarks. We build the discussion based on the results of Fig. 4.4(b), for which the external field is in the y direction. At fixed Ca, there is a specific value of Ca_{mag}, say Ca^*_{mag}, at which the droplet cross-section in the xy plane is circular because the semi-axes in the x and y axis are equal ($D_{xy} = 0$ when $L_x = L_y$). At this condition, the net effects of field-induced extension in the y direction and flow-induced extension in the x direction match one another. Because both viscous and magnetic forces compress the droplet together in the z direction, the droplet becomes an oblate ellipsoid with a polar radius $p_r = L_z$ in the z axis. A similar rationale applies when the external field is in the z direction, as in Fig. 4.5(b). The only difference is that the circular cross-section is in the xz plane ($D_{xz} = 0$ when $L_x = L_z$) and the polar radius is $p_r = L_y$ in the y axis. To

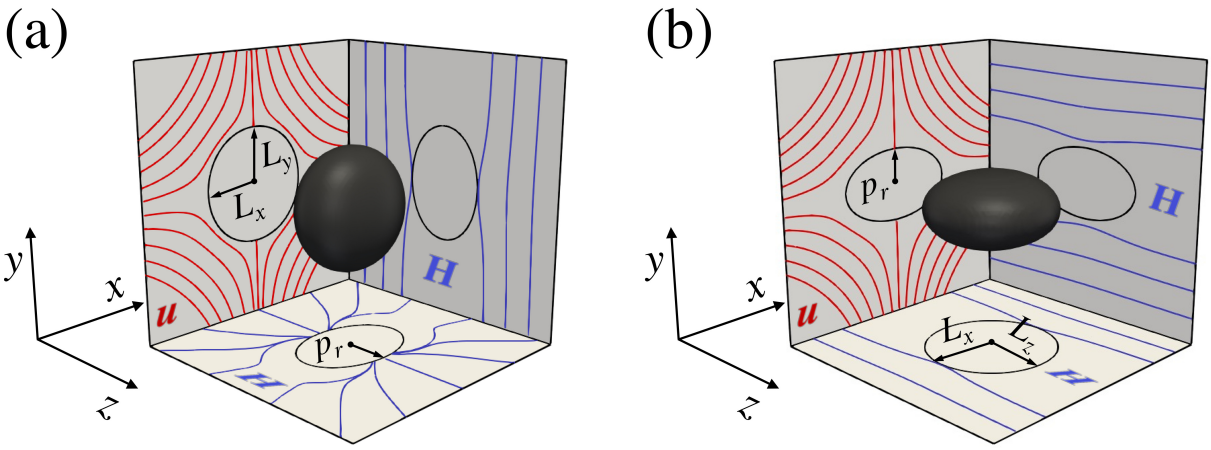

Figure 4.6 – Three-dimensional view of oblate droplets at $Ca = 0.12$ when the external magnetic field is applied in the (a) y direction (at $Ca_{mag} = Ca^*_{mag} \approx 10.03$) and (b) z direction (at $Ca_{mag} = Ca^*_{mag} \approx 5.74$). In (a), $L_x = L_y$ is the equatorial radius in the xy plane and p_r is the polar radius in the z axis; in (b), $L_x = L_z$ is the equatorial radius in the xz plane and p_r is the polar radius in the y axis. For the sake of visualization, the droplet shape is projected on each plane (black), flow streamlines outside the droplet are projected on the xy plane (red), and magnetic field lines outside the droplet are projected on the yz and xz plane (blue). Reprinted from (GUILHERME *et al.*, 2023, p. 9). © 2023 by American Physical Society.

ease the visualization, Fig. 4.6 displays a three-dimensional view of oblate droplets at $Ca = 0.12$ (and $Ca_{mag} = Ca^*_{mag}$) for the two external field configurations. Additionally, Fig. 4.7 shows how Ca^*_{mag} and p_r depend on Ca. Interestingly, both Ca^*_{mag} and p_r vary linearly with Ca, at least within the range of parameters explored here [see the caption of Fig. 4.7 for details]. We note that Ca^*_{mag} increases and p_r decreases with Ca. Because viscous and magnetic forces stretch the droplet in directions that are perpendicular to one another, the magnetic force required to promote a circular droplet cross-section in a plane — either xy or xz — increases as the relative intensity of viscous forces grows stronger. The equatorial radius — either $L_x = L_y$ in the xy plane or $L_x = L_z$ in the xz plane — also increases with the intensity of viscous forces, so that the polar radius — either $p_r = L_z$ in the z axis or $p_r = L_y$ in the y axis — decreases to preserve the droplet volume. At fixed Ca, we see that Ca^*_{mag} and p_r are higher for external fields in the y direction. This is not unexpected, as the field-induced extension is more attenuated by the flow-induced compression in this case. The reader interested in the shape control of liquid droplets through external force fields in hydrodynamic flows is referred to Liu *et al.* (2021), who recently presented a study of the electric field-mediated spheroidizing of leaky dielectric droplets in uniaxial extensional flows.

Overall, the droplet shape is determined by a balance between viscous, magnetic, and capillary forces that depends on the external field intensity and direction relative to the flow. The present discussions can bring new insights to improve the field-assisted manufacturing of microparticles for which shape–property relationships can be broadly

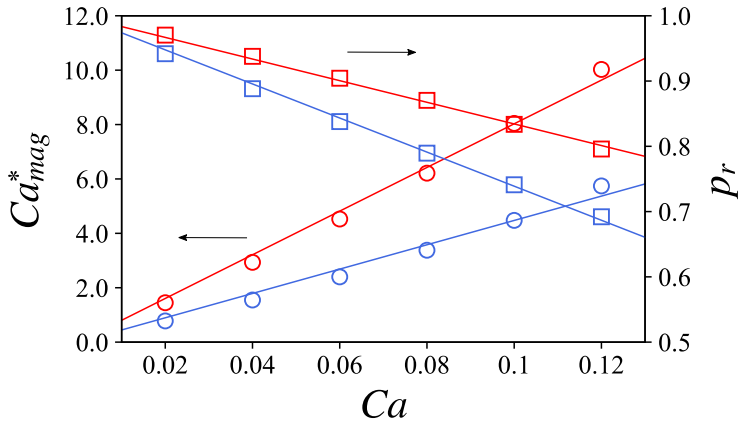

Figure 4.7 – Magnetic capillary number Ca^*_{mag} at which the droplet becomes an oblate ellipsoid (circles, left axis) and the corresponding droplet polar radius p_r (squares, right axis) as a function of Ca. The results are for external magnetic fields applied in the y direction (red symbols) and z direction (blue symbols). The solid lines are linear fits with fixed intercepts ($Ca^*_{mag} = 0$ and $p_r = 1$ at $Ca = 0$): $Ca^*_{mag} \approx 80Ca$ and $p_r \approx 1 - 1.7Ca$ when the external field is in the y direction (red); $Ca^*_{mag} \approx 44Ca$ and $p_r \approx 1 - 2.6Ca$ when the external field is in the z direction (blue). The coefficient of determination of all adjustments is $R^2 > 0.99$. Adapted from (GUILHERME *et al.*, 2023, p. 10). © 2023 by American Physical Society.

explored based on the magnetic–hydrodynamic coupling of ferrofluids and nonmagnetizable liquids (ZHU *et al.*, 2015; ZHAO *et al.*, 2022).

Before proceeding to the next section, it is worth noting that when the magnetic field is applied in one of the flow main directions, as well as when there is no magnetic field, the droplet remains symmetric with respect to the three main directions of the planar extensional flow. Figure 4.8 shows the z component of the flow vorticity $\boldsymbol{\xi} = \boldsymbol{\nabla} \times \boldsymbol{u}$ and flow streamlines near the droplet in the xy plane. The results are for $Ca = 0.04$ when the external field is absent ($Ca_{mag} = 0$) [Fig. 4.8(a)] and when the external field is applied in one of the flow main directions at $Ca_{mag} = 16$ [Figs. 4.8(b)–(d)]. The magnetic field does not change the general flow pattern. Even though the way the distorted droplet affects the streamlines near the interface depends on the external field direction, the flow inside the droplet remains characterized by four recirculation regions in the xy cross-section that are symmetric with respect to the reference axes, as in the absence of the external field. The z component of the vorticity field, however, is skew-symmetric with respect to the reference axes, as the flow inside the droplet follows that of the surrounding fluid near the interface. It is worth noting that the flow near the center of the droplet approaches a planar extensional flow with the extension and compression directions inverted.

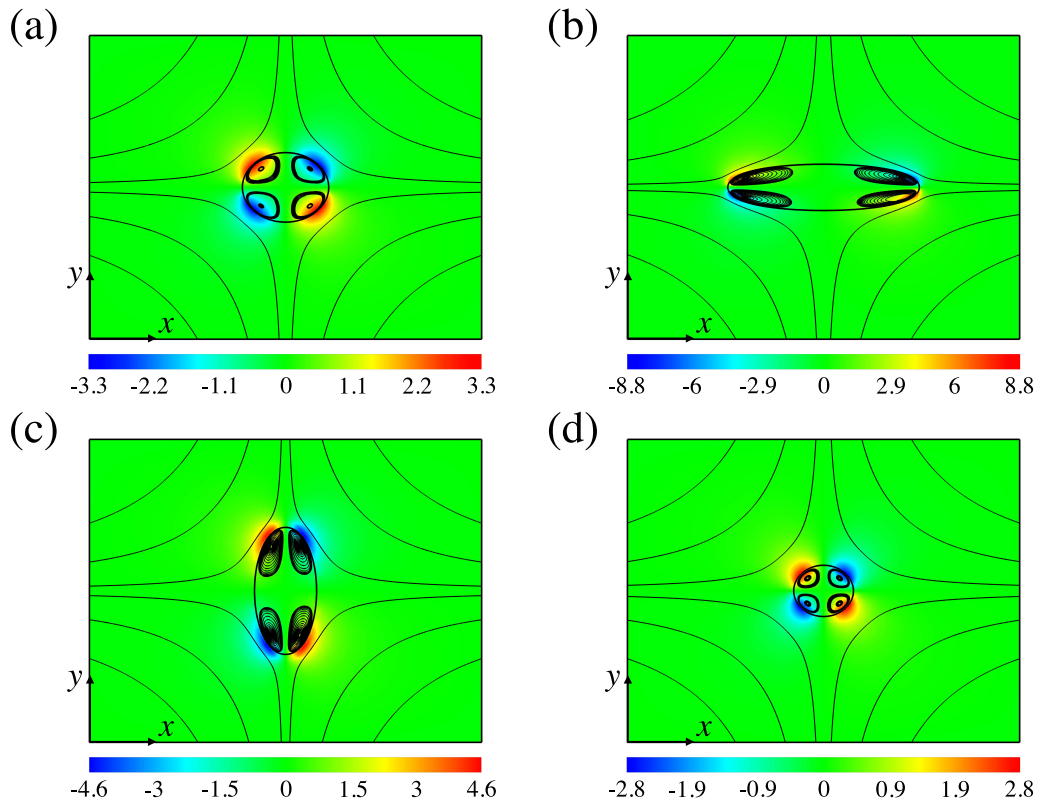

Figure 4.8 – z component of the flow vorticity ($\boldsymbol{\xi} = \boldsymbol{\nabla} \times \boldsymbol{u}$) and flow streamlines in the xy plane. The results are for $Ca = 0.04$ when (a) there is no external magnetic field ($Ca_{mag} = 0$) and when the external magnetic field is applied in the (b) x direction, (c) y direction, and (d) z direction at $Ca_{mag} = 16$. Reprinted from (GUILHERME *et al.*, 2023, p. 11). © 2023 by American Physical Society.

4.2.2 Emulsion magnetization

The magnetization of the system is given by the volumetric average of the local magnetization throughout the system, $\langle \boldsymbol{M} \rangle$ [see Eq. (2.25) in Sec. 2.4]. It is equivalent to the ferrofluid emulsion magnetization of the corresponding volume fraction. On the other hand, as the continuous phase is nonmagnetizable, it does not contribute to the system magnetization, hence the droplet magnetization, $\boldsymbol{M_d}$, is related to $\langle \boldsymbol{M} \rangle$ through $\boldsymbol{M_d} = \langle \boldsymbol{M} \rangle / \beta$. From a particle perspective, we have the droplet magnetic moment, $\boldsymbol{m_d}$, given by $\boldsymbol{m_d} = \boldsymbol{M_d} V_d$, where V_d is the dimensionless droplet volume. The magnetization results will be presented in terms of $\boldsymbol{M_d}$ because of its direct relation with both emulsion magnetization and droplet magnetic moment by dividing it by β and multiplying it by V_d, respectively.

Before proceeding to the analysis, we briefly discuss the demagnetizing effect inside magnetic ellipsoids in the presence of external uniform magnetic fields as it will help us to understand the results for deformed ferrofluid droplets. When subjected to a uniform magnetic field, the magnetic field inside an ellipsoid is also uniform and its intensity, H_{in}, is reduced, so that H_{in} is a decreasing function of a demagnetizing factor, say k (AFKHAMI

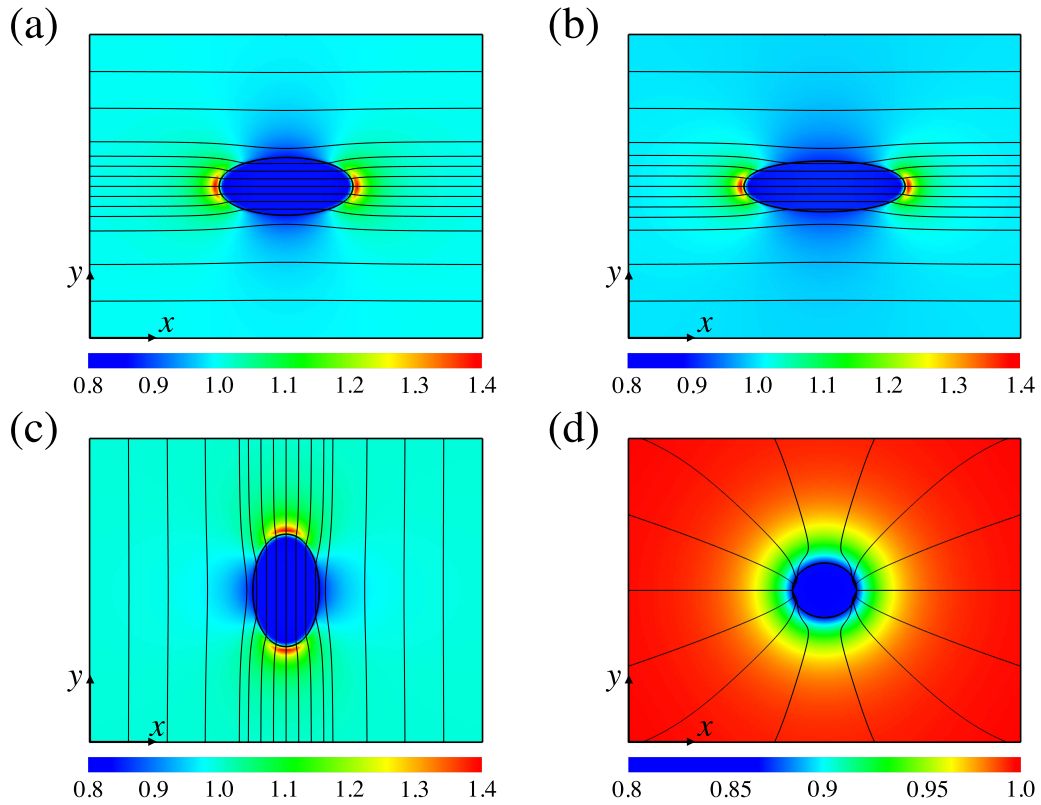

Figure 4.9 – Magnitude of the magnetic field and magnetic field lines in the xy plane. The results are for $Ca_{mag} = 12$ when (a) the external magnetic field is applied in the x direction with no external flow ($\boldsymbol{u}_\infty = \boldsymbol{0}$) and when the external magnetic field is applied in the (b) x direction, (c) y direction, and (d) z direction with the external flow at $Ca = 0.04$. Reprinted from (GUILHERME *et al.*, 2023, p. 12). © 2023 by American Physical Society.

et al., 2010). k is maximized when the ellipsoid is a sphere and becomes smaller as the ellipsoid eccentricity in the external field direction increases. Since the steady shape of the analyzed droplets here are always ellipsoids, their demagnetizing factor should behave in the same way. Furthermore, if one of the ellipsoid main axes is aligned with the external field, the magnetic field inside the body remains aligned with the external field. This is the case for ferrofluid droplets subjected to both planar extensional flows and external fields in one of the flow main directions.

Figure 4.9 shows the magnetic field intensity and lines over the system in the xy plane when the droplet is immersed in a quiescent fluid and subjected to a uniform external field [Fig. 4.9(a)], and when the droplet is subjected to both planar extensional flow and external fields in one of the flow main directions [Figs. 4.9(b)-(d)]. These results illustrate the demagnetizing effect as a function of eccentricity, and the uniformity of the internal field in such cases. Further, we do observe the deflection of the external field near the droplet and the distribution of the field gradients on the droplet surface; they are higher in large curvatures; recalling that the magnetic forces are proportional to $\boldsymbol{H} \cdot \nabla \boldsymbol{H}$ [Eq. (2.5)], we understand the reason why the field-induced distortion acts in the external field direction [see the discussion of Fig. 4.3].

Figure 4.10 shows the magnitude of the droplet magnetization, $M_d = \|\boldsymbol{M_d}\|$, as a function of Ca_{mag} for different values of Ca. We note that M_d grows monotonically with Ca_{mag} independently of the external field direction. Increasing the external field intensity increases the droplet elongation in the external field direction [see Figs. 4.4 and 4.5(b)]; this decreases the demagnetizing factor and increases the droplet magnetization. Viscous forces play a role in the droplet shape and affect the demagnetizing factor as well. Yet, the way M_d trends with Ca essentially depends on the external field direction. We see that M_d increases with Ca when the external field is in the x direction [Fig. 4.10(a)]. The flow improves the droplet magnetization because viscous and magnetic forces stretch the droplet together in the same direction, increasing the overall droplet elongation in the external

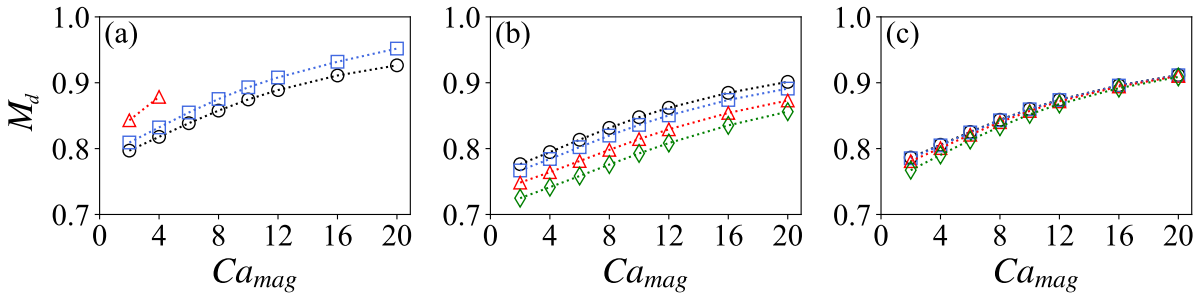

Figure 4.10 – Magnitude of the droplet magnetization (M_d) as a function of Ca_{mag} when the external magnetic field is applied in the (a) x direction, (b) y direction, and (c) z direction. The results are for $Ca = 0.02$ (black circles), $Ca = 0.04$ (blue squares), $Ca = 0.08$ (red triangles), and $Ca = 0.12$ (green diamonds). Adapted from (GUILHERME *et al.*, 2023, p. 12). © 2023 by American Physical Society.

field direction [see Fig. 4.4(a)]. Conversely, M_d decreases with Ca when the external field is in the y direction [Fig. 4.10(b)]. The flow hinders the droplet magnetization because viscous and magnetic forces compete to stretch the droplet in different directions that are perpendicular to one another, decreasing the overall droplet elongation in the external field direction [see Fig. 4.4(b)]. All M_d *vs.* Ca_{mag} curves collapse when the external field is in the z direction [Fig. 4.10(c)]. The flow is not consequential to the droplet magnetization because viscous forces have a minor effect on the droplet elongation in the external field direction when the latter is in the neutral direction [see Fig. 4.5(b)]. In all cases, the rate at which M_d grows with Ca_{mag} decreases as Ca_{mag} increases.

4.2.3 Emulsion rheology

Once we have established the effects of the planar extensional flow and external magnetic fields on dilute ferrofluid emulsions microstructure, we proceed with the analysis of the impacts of the magnetic fields on the planar extensional rheology of such emulsions. In Section 2.3, we derived the expression for the dimensionless droplet stress associated with ferrofluid droplets in suspension, Eq. (2.22), here referred to as droplet stress. For $\lambda = 1$, the third term in the integral vanishes so the droplet stress is

$$\boldsymbol{\sigma^d} = \frac{1}{V}\int_S \left[\left(\frac{\kappa}{Ca} - \frac{Ca_{mag}}{2Ca}\left(\zeta - 1\right)\|\boldsymbol{H}\|^2\right)\boldsymbol{x}\hat{\boldsymbol{n}}\right] \mathrm{d}S. \tag{4.1}$$

From Eq. (4.1) and our previous knowledge about droplet configuration, we can draw some initial conclusions to guide our analysis. First, anisotropic contributions to the stress associated with the droplet shape are captured by the dyadic $\boldsymbol{x}\hat{\boldsymbol{n}}$. Since the droplet configuration is symmetric with respect to the reference axes, the normal components of $\boldsymbol{x}\hat{\boldsymbol{n}}$ are all positive, and the shear components change in sign along the interface in an antisymmetric manner. Furthermore, as the droplet assumes an ellipsoidal shape and the magnetic field is symmetrically distributed over the droplet interface, both κ and $\|\boldsymbol{H}\|^2$ are symmetric and positive. Hence, the shear components of the integrals of $\kappa\boldsymbol{x}\hat{\boldsymbol{n}}$ and $\|\boldsymbol{H}\|^2\boldsymbol{x}\hat{\boldsymbol{n}}$ over S are zero. As a result, the shear stresses of $\boldsymbol{\sigma^d}$ vanish identically, making $\boldsymbol{\sigma^d}$ a symmetric tensor for which the only nonzero entries are the normal stresses σ^d_{xx}, σ^d_{yy}, and σ^d_{zz}.

Second, the stress tensor of the bulk emulsion is affected by the droplets solely through capillary and magnetic forces at the fluid interface. These forces, however, contribute to $\boldsymbol{\sigma^d}$ in opposite manners. Owing to the fact that the normal components of $\kappa\boldsymbol{x}\hat{\boldsymbol{n}}$ and $\|\boldsymbol{H}\|^2\boldsymbol{x}\hat{\boldsymbol{n}}$ at the fluid interface are always positive, the capillary forces contribute to $\boldsymbol{\sigma^d}$ as a traction, while the magnetic forces contribute to $\boldsymbol{\sigma^d}$ as a compression. Note that droplet-induced tractioning compresses the stress state, and vice versa. Separating Eq. (4.1) with respect to these terms, we get the traction term,

$$\boldsymbol{\sigma}_{\boldsymbol{t}}^{\boldsymbol{d}} = \frac{1}{V}\int_S \frac{\kappa}{Ca}\boldsymbol{x}\hat{\boldsymbol{n}}\,\mathrm{d}S, \tag{4.2}$$

and the compression term,

$$\boldsymbol{\sigma}_{\boldsymbol{c}}^{\boldsymbol{d}} = -\frac{1}{V}\int_S \frac{Ca_{mag}}{2Ca}\left(\zeta - 1\right)\|\boldsymbol{H}\|^2\boldsymbol{x}\hat{\boldsymbol{n}}\,\mathrm{d}S. \tag{4.3}$$

While the traction term depends on $1/Ca$, the compression term depends on Ca_{mag}/Ca. It means that at a fixed Ca, increasing Ca_{mag} enhances the overall compression of the stress state. In contrast, at fixed Ca_{mag}, increasing Ca mitigates both the traction and compression contributions to the stress state. If Ca_{mag} is sufficiently small, the normal stresses are positive (traction-dominated), and increasing Ca leads to lower normal stresses (less traction). If Ca_{mag} is sufficiently high, the normal stresses are negative (compression-dominated), and increasing Ca leads to higher normal stresses (less compression). We find that this transition occurs around $Ca_{mag} \approx 6$ for the cases analyzed here. As commented earlier, the droplet shape, represented by the dyadic $\boldsymbol{x}\hat{\boldsymbol{n}}$, plays an important role in both traction and compression terms as a source of anisotropy. As the droplet is stretched in one direction, the normal component of the dyadic associated with that direction is increased, while it is decreased in the other directions. Furthermore, the stretched droplet has a nonuniform distribution of curvature, which contributes to the anisotropy of the traction term.

The droplet contribution to the planar extensional viscosity, (η_p), and to the second extensional viscosity, (η_2) [introduced in Sec. 2.3. See Eqs. (2.23) and (2.24)], are the normal stress differences, and so are directly affected by the anisotropy of the stress state. Thus, Ca and Ca_{mag} affect them both directly and indirectly through the droplet shape.

Figure 4.11 shows η_p (normalized by β) as a function of Ca_{mag} for different values of Ca. Consider first the external field applied in the x direction [Fig. 4.11(a)]. Increasing Ca_{mag} results in greater elongation of the prolate-like droplet in the x direction [see Fig. 4.4(a)]. The higher curvature at the droplet tips along the x axis increases the traction contribution to σ_{xx}^d, while the lower curvature along the droplet tips in the y direction decreases the traction contribution to σ_{yy}^d. Moreover, the rise of the compression contribution to σ_{xx}^d with Ca_{mag} does not follow the increase of the traction counterpart in the same intensity as happens with σ_{yy}^d. As a result, η_p grows with Ca_{mag}, which corresponds to a field-induced viscous-hardening behavior, or equivalently, a magnetic-thickening effect [Fig. 4.11(a)]. Because viscous forces also stretch the droplet in the x direction [see Fig. 4.4(a)], the net effect of increasing Ca is an increase in the anisotropic contribution of $\boldsymbol{x}\hat{\boldsymbol{n}}$ to the traction term. Hence, η_p also grows with Ca [Fig. 4.11(a)]. The growth becomes more significant as long as Ca_{mag} increases, so the magnetic field in the x direction enhances the planar-extensional-thickening effect.

The results with the external field in the y direction are more delicate [Fig. 4.11(b)]. Increasing Ca_{mag} now drives the droplet through a large geometric change in the xy

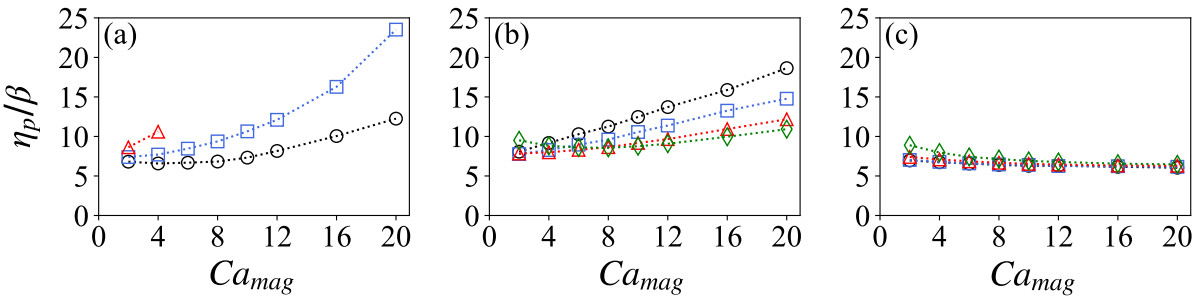

Figure 4.11 – Droplet contribution to the planar extensional viscosity (η_p, normalized by β) of the ferrofluid emulsion as a function of Ca_{mag} when the external magnetic field is applied in the (a) x direction, (b) y direction, and (c) z direction. The results are for $Ca = 0.02$ (black circles), $Ca = 0.04$ (blue squares), $Ca = 0.08$ (red triangles), and $Ca = 0.12$ (green diamonds). Adapted from (GUILHERME *et al.*, 2023, p. 15). © 2023 by American Physical Society.

plane [see Fig. 4.4(b)]; the droplet starts as a prolate-like ellipsoid with the major axis in the x axis at low Ca_{mag}, becomes an oblate ellipsoid with the polar radius in the z axis at $Ca_{mag} = Ca^*_{mag}$, and eventually becomes a prolate-like ellipsoid with the major axis in the y axis at high Ca_{mag}. The anisotropic contribution of $\boldsymbol{x\hat{n}}$ to the compression and traction terms associated with σ^d_{yy} progressively increases throughout this process. Nevertheless, the anisotropic changes in the droplet shape with Ca_{mag} are not accompanied by significant changes in curvature because the viscous and magnetic forces tend to stretch the droplet in different directions, which results in less pronounced curvatures at the droplet tips. As a result, the compression contribution overcomes the traction contribution in σ^d_{yy}, so that η_p generally grows with Ca_{mag} [Fig. 4.11(b)]. The only exception of the growth with Ca_{mag} occurs at $Ca = 0.12$ for $Ca_{mag} \lesssim 6$. This viscous-hardening behavior is less apparent in strong flows because increasing Ca decrease $1/Ca$, which reduces both traction and compression terms resulting in an attenuation of the imbalance of the stress state. For a fixed Ca_{mag}, increasing Ca leads to higher curvatures associated with σ^d_{xx}. The changes in curvature, however, are not significant enough due to the competition of forces in different directions. Because of the attenuation due to $1/Ca$, η_p generally falls with Ca [Fig. 4.11(b)]. In general, the external field in the y direction induces a planar-extensional-thinning effect that enhances with Ca_{mag}. The results for the external field in the z direction are straightforward [Fig. 4.11(c)]. Because both Ca_{mag} and Ca are not very consequential to the droplet shape in the xy plane [see Fig. 4.5(a)], η_p remains nearly constant [Fig. 4.11(c)].

Figure 4.12 shows the results for η_2 (also normalized by β) as a function of Ca_{mag} for different values of Ca. To assist the discussion, Fig. 4.13 presents the droplet deformation in the yz plane, D_{zy}. When the external field is in the x direction [Fig. 4.12(a)], viscous and magnetic forces compress the droplet together with similar intensities in the y and z direction, so that Ca_{mag} and Ca do not induce substantial changes in the droplet deformation in the yz plane [Fig. 4.13(a)]. For this reason, η_2 is nearly constant [Fig. 4.12(a)]. This is equivalent to the results for η_p when the external field is in the z direction [see

Fig. 4.11(c)].

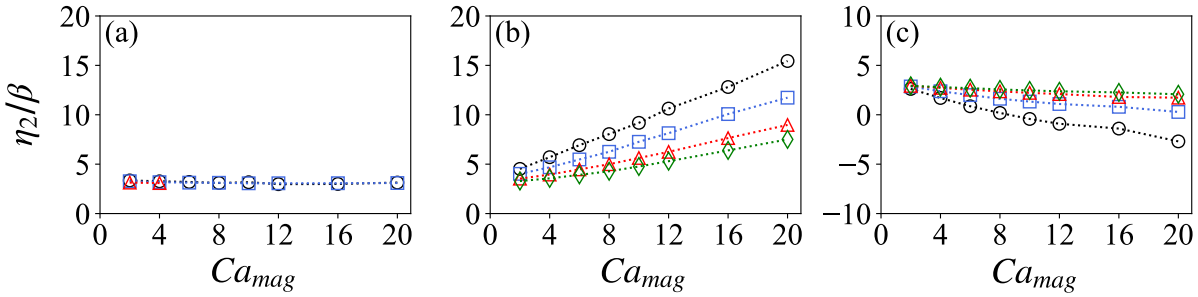

Figure 4.12 – Droplet contribution to the second extensional viscosity (η_2, normalized by β) of the ferrofluid emulsion as a function of Ca_{mag} when the external magnetic field is applied in the (a) x direction, (b) y direction, and (c) z direction. The results are for $Ca = 0.02$ (black circles), $Ca = 0.04$ (blue squares), $Ca = 0.08$ (red triangles), and $Ca = 0.12$ (green diamonds). Adapted from (GUILHERME *et al.*, 2023, p. 15). © 2023 by American Physical Society.

When applied in the y direction, the external field induces a viscous-hardening behavior of η_2 [Fig. 4.12(b)]. The increasing of Ca_{mag} increases the stretching in the y direction resulting in an increase of the anisotropic contribution of $\boldsymbol{x}\hat{\boldsymbol{n}}$ to both traction and compression term associated with σ^d_{yy}. The rise in the traction term, however, is less significant than that of the compression term, because the changes in curvature are less pronounced than the changes in Ca_{mag} [see Fig. 4.13(b)]. This rationale is the same as that applied to η_p, but with less intense hardening behavior. That difference becomes evident if we regard the z direction as a direction of extension but with lower intensity compared to the x direction. The traction term associated with σ^d_{zz} in strong flows is not too significant in lower field intensities ($Ca_{mag} = 2$) as σ^d_{xx} is, so the viscous-hardening effect happens even at $Ca = 0.12$ for $Ca_{mag} \lesssim 6$. Note that, at low Ca_{mag}, D_{xy} grows with Ca much more significantly than D_{zy} do [see Figs. 4.4(b) and 4.13(b)]. In summary, η_2 grows with Ca_{mag} and falls with Ca [Fig. 4.12(b)].

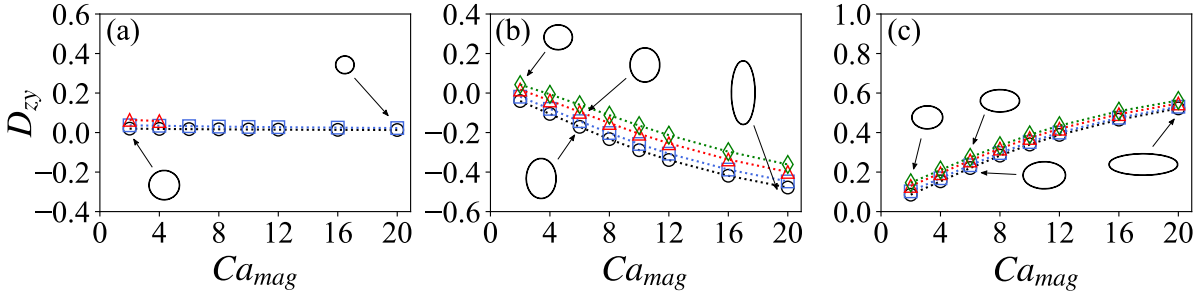

Figure 4.13 – Droplet distortion in the yz plane (D_{zy}) as a function of Ca_{mag} when the external magnetic field is applied in the (a) x direction, (b) y direction, and (c) z direction. The results are for $Ca = 0.02$ (black circles), $Ca = 0.04$ (blue squares), $Ca = 0.08$ (red triangles), and $Ca = 0.12$ (green diamonds). The insets show the droplet cross-section in the yz plane at different conditions. Adapted from (GUILHERME *et al.*, 2023, p. 16). © 2023 by American Physical Society.

The same rationale applies to the field-induced viscous-softening behavior, or equivalently, the magnetic-thinning effect of η_2 when the external field is in the z direction [Fig. 4.12(c)]. Increasing Ca_{mag} and stretching the droplet in the z direction leads to compression terms stronger than the corresponding traction terms because of insufficiently strong changes in the droplet curvature [see Fig. 4.13(c)]. This time, increasing Ca decreases the curvature at the droplet tips in the y direction more than the anisotropic terms associated with σ^d_{yy}, while the curvature at the droplet tips in the z direction and the anisotropic terms associated with σ^d_{zz} does not change substantially. As a result, the difference of the traction terms becomes more important so η_2 increases, characterizing a second-extensional-thickening behavior. In summary, η_2 falls with Ca_{mag} and grows with Ca [Fig. 4.12(c)].

The latter result deserves a special remark. Unlike the field-induced viscous-hardening behavior observed in the cases where the external field is applied in the x and y directions, the external field in the z direction induces a viscous-softening behavior of the droplet contribution to the second extensional viscosity, η_2. This contribution eventually achieves negative values at low Ca and high Ca_{mag}. Therefore, in this case, increasing the external field intensity mitigates the difficulty added by the droplet in imposing the bulk extensional kinematics in the yz plane; when η_2 is negative, the droplet facilitates the bulk motion in this plane. It is worth mentioning, however, that although the presence of the droplet can facilitate the bulk emulsion motion in the yz plane (when in the presence of external magnetic fields), the emulsion second extensional viscosity itself, η_{cross}, is not necessarily negative due to the remaining Newtonian part [see Sec. 2.3].

4.3 External magnetic fields applied in a direction different from one of the flow main directions

We now take $\boldsymbol{H_0} = \left(\hat{\boldsymbol{e}}_{\boldsymbol{x}} + \hat{\boldsymbol{e}}_{\boldsymbol{y}}\right)/\sqrt{2}$, so that the external magnetic field is perpendicular to the z axis and parallel to the $x = y$ plane. With this configuration, the droplet does not achieve a steady shape at $Ca = 0.12$ and $Ca_{mag} \geq 2$, at $Ca = 0.1$ and $Ca_{mag} \geq 6$, and at $Ca = 0.08$ and $Ca_{mag} \geq 16$. We explore the parameter space accordingly.

4.3.1 Droplet configuration

Figure 4.14 shows a three-dimensional view of the droplet at $Ca = 0.02$ and $Ca_{mag} = 20$. Even though symmetric with respect to the xy plane, the prolate-like droplet is not symmetric with respect to the x and y axis separately. The droplet configuration is now assessed with the Taylor's deformation parameter D and the angle θ between the droplet major axis and the x axis (see Sec. 2.5). Figure 4.15 shows how D and θ (normalized by $\pi/4$) vary with Ca_{mag} and Ca. Viscous and magnetic forces stretch the

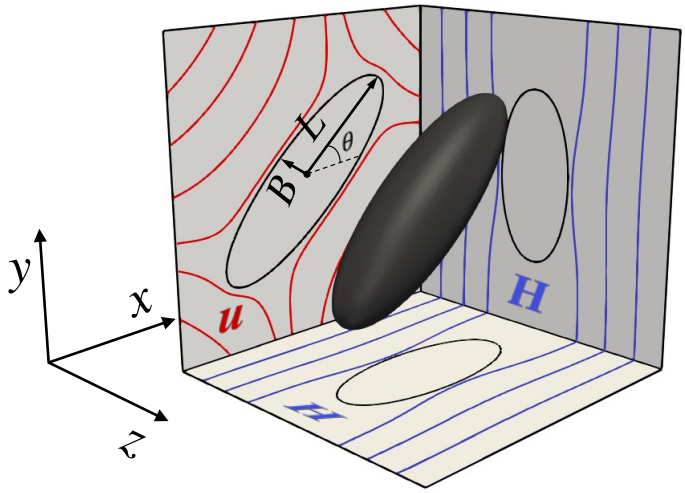

Figure 4.14 – Three-dimensional view of the prolate-like droplet at $Ca = 0.02$ when the external magnetic field is applied in the $x = y$ direction at $Ca_{mag} = 20$. The droplet shape is projected on each plane (black), flow streamlines outside the droplet are projected on the xy plane (blue), and magnetic field lines outside the droplet are projected on the xz and yz plane (red). The angle θ is determined by the droplet major axis and the x axis. Reprinted from (GUILHERME *et al.*, 2023, p. 17). © 2023 by American Physical Society.

droplet in directions that are neither parallel nor perpendicular to one another. The viscous forces are responsible for flow-induced extension in the x direction, whereas the magnetic forces are responsible for field-induced extension in the $x = y$ direction. The magnetic force can be generally split into three components: one that collaborates with viscous extension in the x direction; one that counteracts viscous compression in the y direction; and one that collaborates with viscous compression in the z direction. It follows that D grows with both Ca_{mag} and Ca [Fig. 4.15(a)].

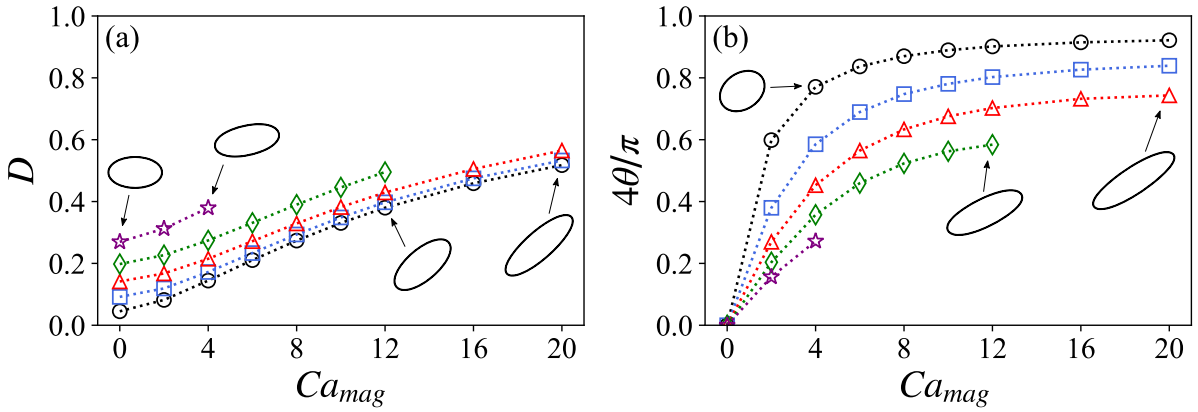

Figure 4.15 – (a) Droplet distortion (D) and (b) orientation (θ, normalized by $\pi/4$) as a function of Ca_{mag} when the external magnetic field is applied in the $x = y$ direction. The results are for $Ca = 0.02$ (black circles), $Ca = 0.04$ (blue squares), $Ca = 0.06$ (red triangles), $Ca = 0.08$ (green diamonds), and $Ca = 0.1$ (magenta stars). The insets show the droplet cross-section in the xy plane at different conditions. Adapted from (GUILHERME *et al.*, 2023, p. 17). © 2023 by American Physical Society.

The balance between viscous and magnetic forces also determines the droplet orientation in the flow. While the former tends to align the droplet major axis with the direction of flow extension, the latter tends to align the droplet major axis with the external field direction. At fixed Ca_{mag}, θ decreases as Ca increases; conversely, at fixed Ca, θ increases as Ca_{mag} increases. Hence, θ grows with Ca_{mag} and the curves of θ *vs.* Ca_{mag} shift upwards as Ca falls [Fig. 4.15(b)]. The droplet orientation is $0 < \theta < \pi/4$; we expect $\theta = 0$ as $Ca_{mag}/Ca \to 0$ (or in the absence of external field) and $\theta = \pi/4$ as $Ca_{mag}/Ca \to \infty$ (or in the absence of external flow). The predictions also suggest that the dependence of D on Ca and of θ on Ca_{mag} becomes weaker as Ca_{mag} grows stronger. That is, there is a threshold value of Ca_{mag} above which a further increase in Ca_{mag} changes D without changing θ, which becomes a function of Ca only.

Figure 4.16 shows the z component of the flow vorticity and flow streamlines near the droplet in the xy plane at $Ca = 0.04$ and $Ca_{mag} = 16$ [see Fig. 4.8 for comparison]. The tilted configuration, promoted by the magnetic forces when the magnetic field is applied in the $x = y$ direction, changes the way the flow inside the droplet interacts with the external flow. The viscous forces induced by the new surrounding flow push the two vortices of negative vorticity toward the droplet tips and eventually merge the two vortices of positive vorticity into a large vortex around the droplet center. We also tested the field in the $x = -y$ direction to investigate if the negative vortices that merge one another, and that is indeed the case. In both cases, the flow inside the droplet becomes characterized by three recirculation regions, highlighting an intriguing field-induced topological transformation of the flow pattern at the droplet scale. By way of information, the merge of the vortices happens gradually as long as Ca_{mag} increases and the droplet elongates.

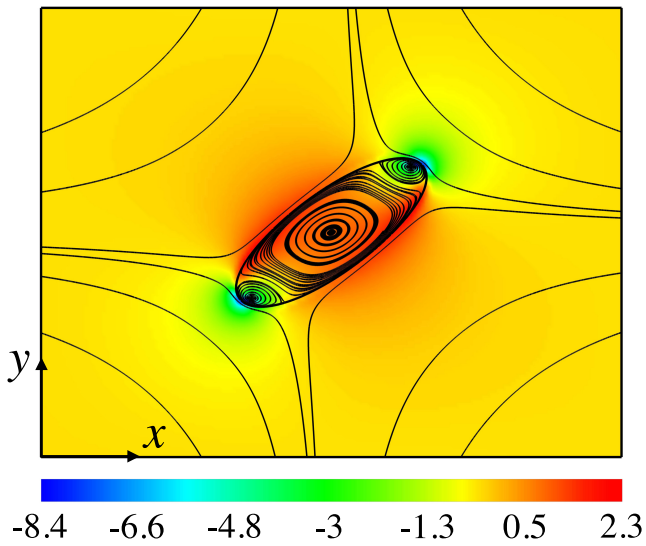

Figure 4.16 – z component of the flow vorticity ($\boldsymbol{\xi} = \boldsymbol{\nabla} \times \boldsymbol{u}$) and flow streamlines in the xy plane. The result is for $Ca = 0.04$ when the external magnetic field is applied in the $x = y$ direction at $Ca_{mag} = 16$. Reprinted from (GUILHERME *et al.*, 2023, p. 19). © 2023 by American Physical Society.

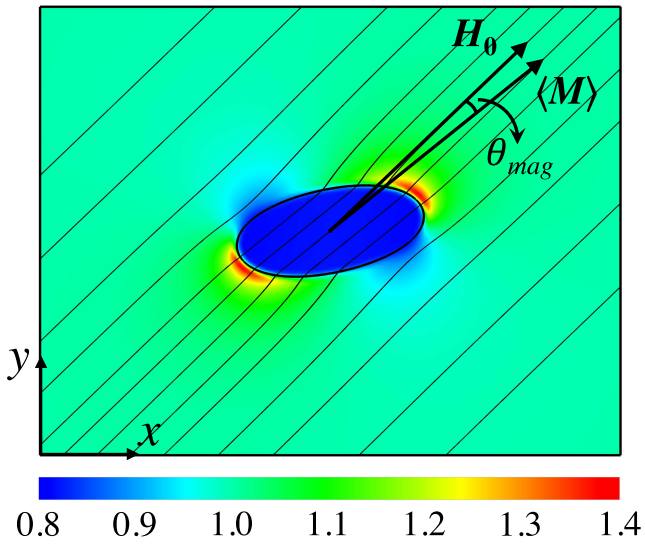

Figure 4.17 – Magnitude of the magnetic field and magnetic field lines in the xy plane. The result is for $Ca = 0.1$ when the external magnetic field is applied in the $x = y$ direction at $Ca_{mag} = 4$. The arrows (not to scale) indicate the direction of the external field $\boldsymbol{H_0}$ and the direction of the system magnetization $\langle \boldsymbol{M} \rangle$; θ_{mag} is the angle between them. Reprinted from (GUILHERME *et al.*, 2023, p. 18). © 2023 by American Physical Society.

4.3.2 Emulsion magnetization

Figure 4.17 shows the magnetic field intensity and lines near the droplet in the xy plane at $Ca = 0.1$ and $Ca_{mag} = 4$ [refer to Fig. 4.9 for comparison]. The magnetic field inside the droplet remains uniform due to its ellipsoidal shape, but the field lines are no longer parallel to the external field direction. Notably, the regions of higher or lower field intensity outside the droplet, close to the interface, are not symmetric and differ from the regions of maximum or minimum curvature at the droplet tips. Consequently, the magnetic force, which is a function of $\nabla \boldsymbol{H}$ and acts normal to the interface, induces a torque, due to the conservation of volume of the droplet, that causes the droplet major axis to lean counterclockwise around the z axis (towards the external field direction). As the ferrofluid is superparamagnetic, the droplet magnetization is parallel to the magnetic field inside the droplet. Thus, the primary effect of the magnetic torque is to align the droplet magnetization with the external field. In the absence of the external flow, the droplet magnetization would be in the direction of the external field. The viscous forces induced by the external flow, however, tend to tilt the droplet major axis clockwise around the z axis (towards the direction of flow extension), which forms an angle θ_{mag} between the droplet magnetization $\boldsymbol{M_d}$ and the external field $\boldsymbol{H_0}$ [see Fig. 4.17], and hence induces a magnetic torque at the droplet level. θ_{mag} varies as long as the droplet configuration changes, which in turn varies θ_{mag} and the magnetic and viscous torques relation. When the droplet achieves a stationary configuration, the torques balance one another, and θ_{mag} reaches a steady state. Note that the droplet only tilts in the extensional flow because the external field is not aligned with one of the flow main directions.

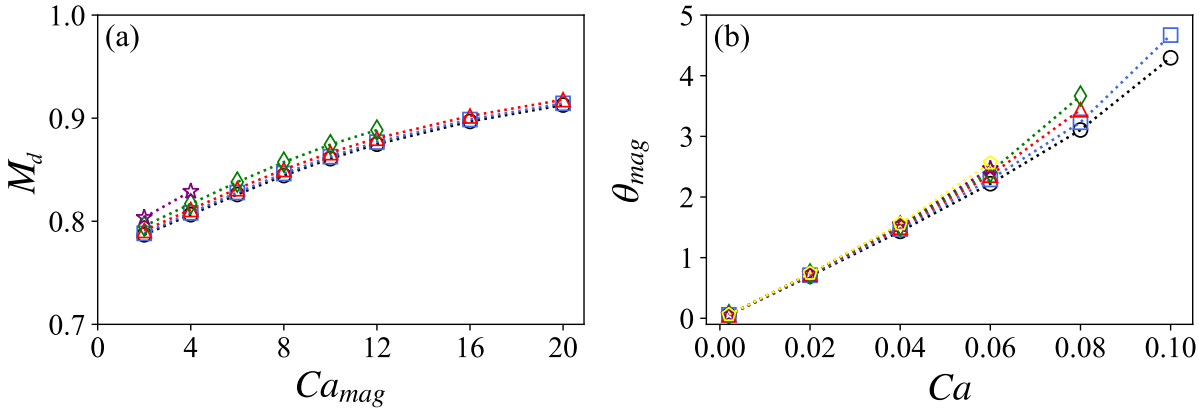

Figure 4.18 – (a) Magnitude of the droplet magnetization (M_d) as a function of Ca_{mag}. The results are for $Ca = 0.02$ (black circles), $Ca = 0.04$ (blue squares), $Ca = 0.06$ (red triangles), $Ca = 0.08$ (green diamonds), and $Ca = 0.1$ (magenta stars). (b) Angle between the ferrofluid emulsion bulk magnetization and the external field direction (θ_{mag}, in degrees) as a function of Ca. The results are for $Ca_{mag} = 2$ (black circles), $Ca_{mag} = 4$ (blue squares), $Ca_{mag} = 8$ (red triangles), $Ca_{mag} = 12$ (green diamonds), $Ca_{mag} = 16$ (magenta stars), and $Ca_{mag} = 20$ (yellow pentagons). In both cases, the external magnetic field is applied in the $x = y$ direction. Adapted from (GUILHERME *et al.*, 2023, p. 20). © 2023 by American Physical Society.

Macroscopically, the ferrofluid emulsion no longer responds as a superparamagnetic material, as there is a small angle θ_{mag} between the system magnetization $\langle \boldsymbol{M} \rangle$ and the external field $\boldsymbol{H_0}$ [see Fig. 4.17]. Conversely, the bulk emulsion experiences a field-induced internal torque $\boldsymbol{\tau_{mag}} = (Ca_{mag}/Ca)\langle \boldsymbol{M} \rangle \times \boldsymbol{H_0}$ whose intensity is $\tau_{mag} = (Ca_{mag}/Ca)\beta M_d \sin\theta_{mag}$. Figure 4.18 shows M_d as a function of Ca_{mag} and θ_{mag} as a function of Ca. Increasing the external field intensity stretches and tilts the droplet towards the external field direction [see Fig. 4.15]. Both effects decrease the droplet demagnetizing factor, so that M_d grows with Ca_{mag} [Fig. 4.18(a)]. Increasing the strength of viscous forces also stretches the droplet, but hinders the droplet alignment with the external field direction [see Fig. 4.15]. It turns out that the combined action of these two effects is not consequential to the droplet demagnetizing factor so that M_d is nearly constant with Ca [Fig. 4.18(a)]. Additionally, θ_{mag} increases close to linearly with Ca and is a weak function of Ca_{mag} [Fig. 4.18(b)]. This suggests that the flow is the main responsible for promoting field-induced internal torques in the bulk emulsion, provided that an external magnetic field exists to trigger the droplet magnetization. Figure 4.19 shows τ_{mag} (normalized by β) increases with Ca_{mag} and is approximately independent of Ca. The rationale is the following: first, τ_{mag} scales with Ca_{mag}, and increasing Ca_{mag} increases M_d without changing θ_{mag}; second, even though τ_{mag} scales with $1/Ca$, increasing Ca increases θ_{mag} without changing M_d. Because θ_{mag} is generally small, so that $\sin\theta_{mag} \approx \theta_{mag}$, the net effects of changing Ca on τ_{mag} are negligible. In summary, the ferrofluid emulsion behaves like a bulk material that, when subjected to external magnetic fields, responds to external extensional loads with field-induced internal torques.

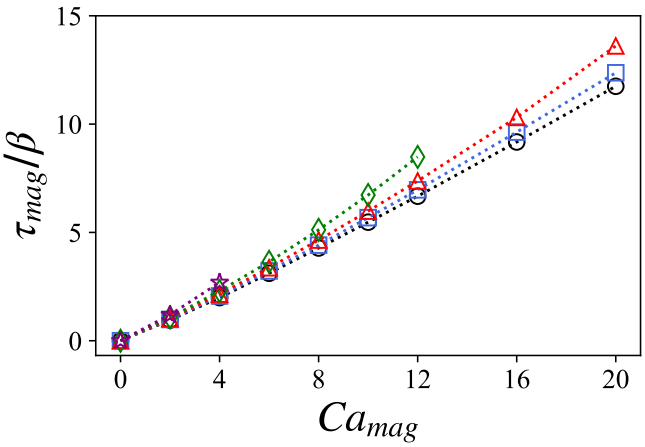

Figure 4.19 – Magnitude of the field-induced internal torque in the ferrofluid emulsion (τ_{mag}, normalized by β) as a function of Ca_{mag} when the external magnetic field is applied in the $x = y$ direction. The results are for $Ca = 0.02$ (black circles), $Ca = 0.04$ (blue squares), $Ca = 0.06$ (red triangles), $Ca = 0.08$ (green diamonds), and $Ca = 0.1$ (magenta stars). Adapted from (GUILHERME *et al.*, 2023, p. 20). © 2023 by American Physical Society.

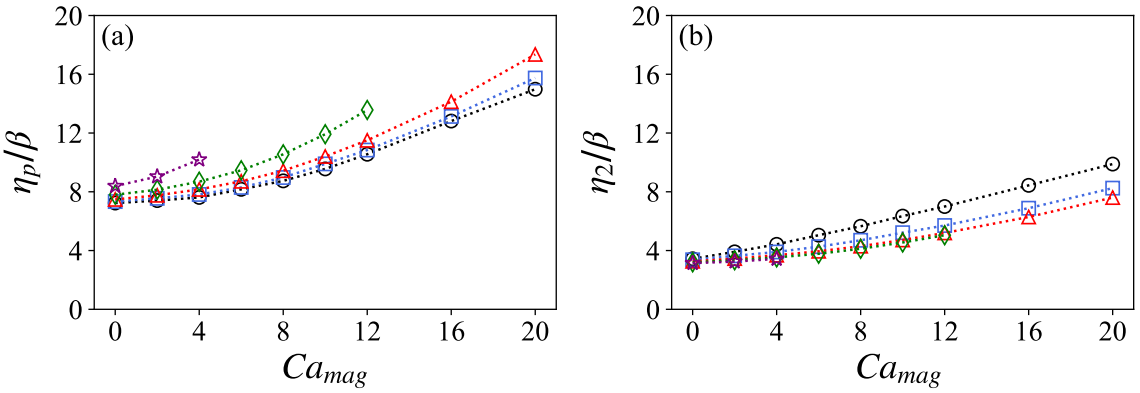

Figure 4.20 – Droplet contribution to the (a) planar extensional viscosity (η_p, normalized by β) and (b) second extensional viscosity (η_2, normalized by β) of the ferrofluid emulsion as a function of Ca_{mag} when the external magnetic field is applied in the $x = y$ direction. The results are for $Ca = 0.02$ (black circles), $Ca = 0.04$ (blue squares), $Ca = 0.06$ (red triangles), $Ca = 0.08$ (green diamonds), and $Ca = 0.1$ (magenta stars). Adapted from (GUILHERME *et al.*, 2023, p. 21). © 2023 by American Physical Society.

4.3.3 Emulsion rheology

Fig. 4.20 shows η_p and η_2 as a function of Ca_{mag} for different values of Ca. The trends are qualitatively similar to those discussed for Figs. 4.11 and 4.12 with the external field applied in the x and y directions. Because the droplet orientation is $0 < \theta < \pi/4$ [see Fig. 4.15(b)], the projection of the droplet major axis on the x axis is larger than the projection on the y axis. In a simplified manner, the general behavior η_p and η_2 when the external field is applied in the $x = y$ direction can be regarded as a weighted mean of the behavior when the external field is in the x and y directions separately, with more weight for that of the external field in the x direction. So, the field-induced viscous-hardening

behavior (and planar-extensional-thickening) of η_p in Fig. 4.20(a) is a less pronounced version of that when the external field is in the x direction [see Fig. 4.11(a)]. The same rationale applies to η_2. The viscous-hardening (and second-extensional-thinning) shown in Fig. 4.20(b) reflects the results with the external field in the y direction [see Fig. 4.12(b)], but with less pronounced effect due to the almost constant η_2 when the external field is in the x direction.

The steady-state rheology of complex fluids relies on a set of material functions that can capture the deviatoric part of the stress tensor in a motion with constant stretch history. The appearance of field-induced internal torques in the system implies that the droplet stress is no longer symmetric and contributes with shear stresses to the bulk stress tensor of the ferrofluid emulsion. As the two usual extensional viscosity coefficients are associated with normal stresses only, we must introduce new material functions to account for these unexpected shear stresses and fully characterize the stress state in planar extension. The parallel with shear rheology is straightforward: even though the rate-of-strain tensor only has shear components in viscometric flows, one still defines viscometric material functions associated with normal stresses. It is important to make a distinction between extensional motion and extensional loading at this point. The existence of shear stresses in extensional flows is related to the anisotropic nature of the fluid microstructure. Shear stresses appear as a macroscopic response to sustain the imposed extensional motion when the microstructure orientation is not aligned with one of the flow main directions. Here, the microstructure of the ferrofluid emulsion consists of ferrofluid droplets whose intrinsic orientation is affected by the external field configuration. Additionally, it is instructive to revisit the definition of the droplet stress in Eq. (4.1). Because the droplet is now tilted with respect to the references axes, changes in the sign of the shear components of $\boldsymbol{x}\hat{\boldsymbol{n}}$ at the interface are not exactly antisymmetric; likewise, the distributions of κ and $\|\boldsymbol{H}\|^2$ at the interface are not exactly symmetric [see Fig. 4.17]. As a result, the shear components of the integrals of $\kappa\boldsymbol{x}\hat{\boldsymbol{n}}$ and $\|\boldsymbol{H}\|^2\boldsymbol{x}\hat{\boldsymbol{n}}$ over S do not vanish; instead, they lead to nonsymmetric shear stresses in $\boldsymbol{\sigma^d}$.

Let $\boldsymbol{S^d}$ and $\boldsymbol{W^d}$ be the symmetric and skew-symmetric parts of $\boldsymbol{\sigma^d}$, respectively. We now define $\eta_s = S^d_{xy}$ and $\eta_r = W^d_{xy}$ as the dimensionless droplet contribution to the shear and rotational viscosity coefficients of ferrofluid emulsions in planar extension, respectively. Note that η_s and η_r are new material functions associated with shear stresses in the xy plane of the planar extensional flow. Figure 4.21 shows η_s and η_r as a function of Ca_{mag} for different values of Ca. Because the shear stresses in the bulk emulsion are in the clockwise direction [see Figs. 4.17 and 4.16], σ^d_{yx} is positive and σ^d_{xy} is negative. To explain this further, we analyze the traction and compression terms of the droplet stress separately [see Eqs. (4.2) and (4.3)]. The traction contributions to σ^d_{xy} and σ^d_{yx} are both positive because the regions of high/low curvature at the interface coincide with those where the shear components of $\boldsymbol{x}\hat{\boldsymbol{n}}$ are positive/negative. However, these contributions are equal to one another because the curvature distribution is symmetric with respect

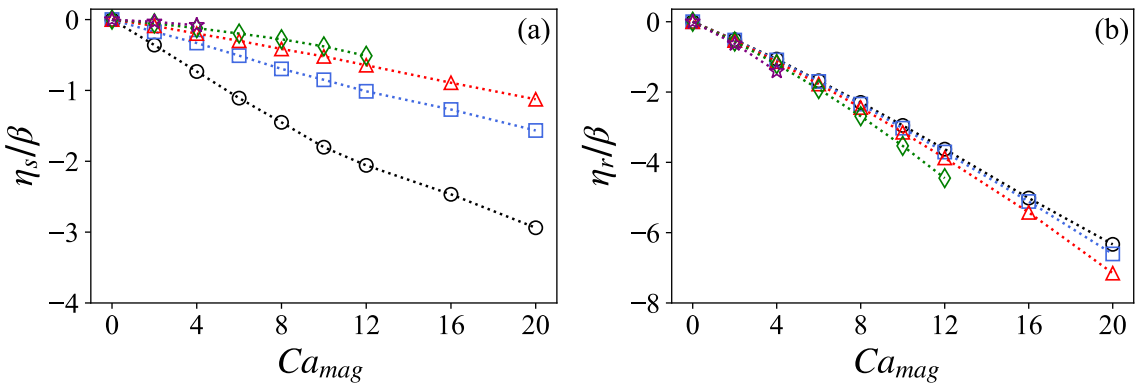

Figure 4.21 – Droplet contribution to the (a) shear viscosity (η_s, normalized by β) and (b) rotational viscosity (η_r, normalized by β) of the ferrofluid emulsion as a function of Ca_{mag} when the external magnetic field is applied in the $x = y$ direction. The results are for $Ca = 0.02$ (black circles), $Ca = 0.04$ (blue squares), $Ca = 0.06$ (red triangles), $Ca = 0.08$ (green diamonds), and $Ca = 0.1$ (magenta stars). Adapted from (GUILHERME *et al.*, 2023, p. 22). © 2023 by American Physical Society.

to the droplet major axis. Following the same rationale, the compression contributions to σ^d_{xy} and σ^d_{yx} are both negative because the magnetic field intensity near the droplet is higher/lower near the regions where the shear components of $\boldsymbol{x}\hat{\boldsymbol{n}}$ are positive/negative. Nevertheless, the distribution of magnetic field intensity near the interface is not symmetric with respect to the droplet major axis. The regions of high field intensity are dislocated in the counterclockwise direction from the droplet tips towards the regions where the xy component of $\boldsymbol{x}\hat{\boldsymbol{n}}$ is positive. Moreover, as the droplet orientation is $0 < \theta < \pi/4$ [see Fig. 4.15(b)], the xy component of $\boldsymbol{x}\hat{\boldsymbol{n}}$ is positive over a larger portion of the interface. The compression contribution to σ^d_{xy} is thus more intense than that associated with σ^d_{yx}. As a result, η_s is negative; based on the role Ca_{mag} and Ca play in the droplet distortion and orientation in the flow [see Fig. 4.15], it follows that η_s falls with Ca_{mag} and grows with Ca [Fig. 4.21(a)]. The rotational viscosity is strictly associated with the field-induced internal torque [see Fig. 4.19], so that η_r simply scales with τ_{mag} [Fig. 4.21(b)]. The fact that η_r is negative just reflects that the droplet contribution to the macroscopic flow opposes the magnetic torque induced at the droplet surface.

These results clarify the fact that if the external field direction is not in any of the main planes (xy, yz, and zx), the lack of symmetry with respect to these planes would lead to nonsymmetric shear stresses in all of them. In this case, it would be necessary to assess eight material functions in order to fully characterize the stress state in planar extension: the planar extensional viscosity, the second extensional viscosity, three pairs of shear and rotational viscosity coefficients associated with the shear stresses in each plane.

4.4 Conditions for stable ferrofluid emulsions: analysis of droplet breakup

In the previous sections, we have established the microstructure, magnetization, and planar extensional rheology of dilute ferrofluid emulsions. Now, we seek to determine and give some reasoning on the planar extensional flow conditions in which a ferrofluid emulsion submitted to an external magnetic field remains stable, i.e., the conditions in which the ferrofluid droplet does not break up and achieves a steady shape state. For this analysis, we will consider two decades of λ: from $\lambda = 0.1$ to $\lambda = 10$; and the external magnetic field applied in each of the three flow's main directions. The critical capillary number, $Ca_c = Ca_c(Ca_{mag}, \boldsymbol{H_0}/\|\boldsymbol{H_0}\|; \lambda)$, is the parameter under investigation, obtained via the procedure described in Sec. 2.6.

Before proceeding to the investigation of the role of the magnetic fields in the droplet breakup, we analyze the case in which the magnetic field is absent. Recalling the description of the breakup process for $\lambda = 1$ highlighted in Sec. 4.1.1, we have that for above a certain value of Ca, the flow induces a shift in the surface curvature at the central portion (see Fig. 4.23). Once this point is reached, the droplet distortion continuously increases, and no steady shapes seem to be possible. This process is referred to as droplet breakup, which is consistent with the descriptions of (TAYLOR, 1934; GRACE, 1982; RUMSCHEIDT; MASON, 1961; BENTLEY; LEAL, 1986; BIBEN *et al.*, 2003). Indeed, if the flow is abruptly stopped after a large droplet elongation, the droplet disintegrates into many smaller droplets (RUMSCHEIDT; MASON, 1961; BIBEN *et al.*, 2003).

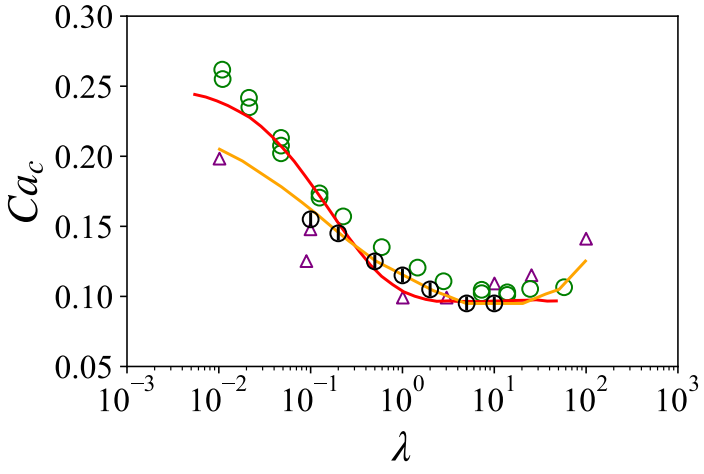

Figure 4.22 – Critical capillary number (Ca_c) as a function of λ with no magnetic field ($Ca_{mag} = 0$): present work (black circles), experimental results of Bentley and Leal (1986) and Grace (1982) (green circles and red triangles, respectively), second order small deformation theory by Bentley and Leal (1986) (red line), and simulation results of Biben *et al.* (2003) (yellow line). The black lines inside the black circles represent the error bars of our estimations.

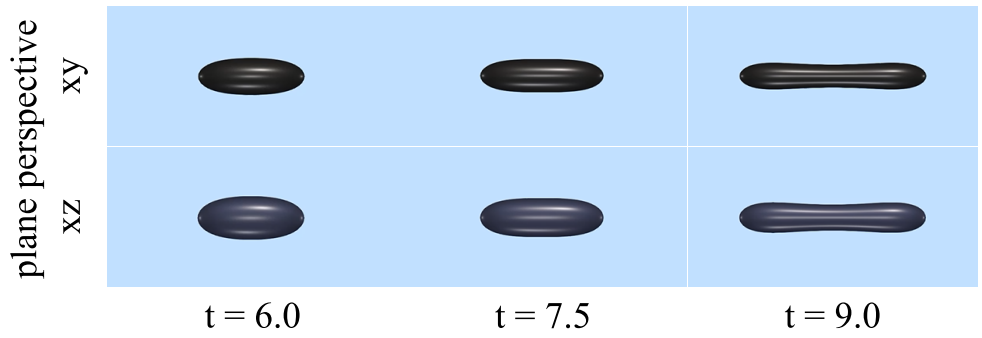

Figure 4.23 – Clip of the breakup process in the absence of magnetic field ($Ca_{mag} = 0$) for $\lambda = 1$ with $Ca = 0.12$. The curvatures in the xy plane and in the xz plane are "flattened" at around the same time ($t = 7.5$) in the central portion, although the deformations in the respective planes are not the same. From that time, the surface in the central portion becomes concave.

Figure 4.22 shows Ca_c as a function of λ for a viscous regular droplet subjected to a planar extensional flow. We also present the experimental results of Grace (1982) and Bentley and Leal (1986) (both measured in four-roll mill apparatus), the second-order small deformation theory of Bentley and Leal (1986), and the numerical results of Biben *et al.* (2003), who performed simulations using an uniaxial extensional flow. The error bars inside the black circles are sized by the ΔCa used and centered at the measured Ca_c. For planar extensional flows, Ca_c slightly varies with λ, only around 0.05 in two decades of change in λ, with low droplet viscosities requiring more flow strength to be broken out. This is attributed to the fact that as the viscosity ratio increases, for the same flow strength, the viscous stress at the droplet surface increases, hence the droplet becomes more likely to be distorted by the flow, as can be seen in Fig. 4.24 for $Ca = 0.09$. We found that the breakup process described above is qualitatively the same for all studied λ. The results of Fig. 4.22 confirm the reliability of the used grid spacing and estimation procedure.

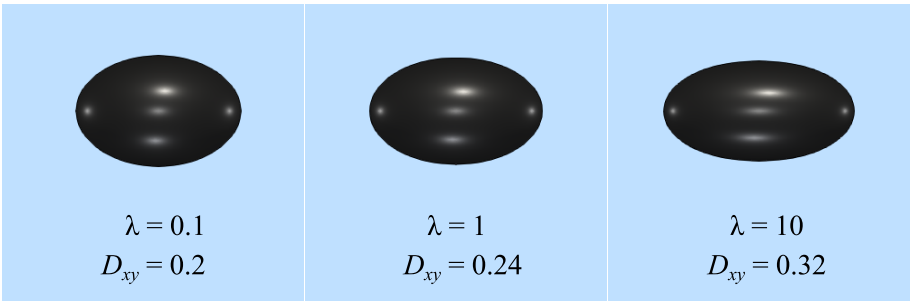

Figure 4.24 – Droplet steady shape for $Ca = 0.09$ and different λ with no magnetic field ($Ca_{mag} = 0$). The ratio Ca/Ca_c for each case is from left to right: 0.58, 0.78, and 0.95.

4.4.1 Magnetic field applied in one of the flow main directions

Figure 4.25 shows the critical capillary number as a function of λ. The results are for different values of Ca_{mag} when the external magnetic field is applied in the x, y,

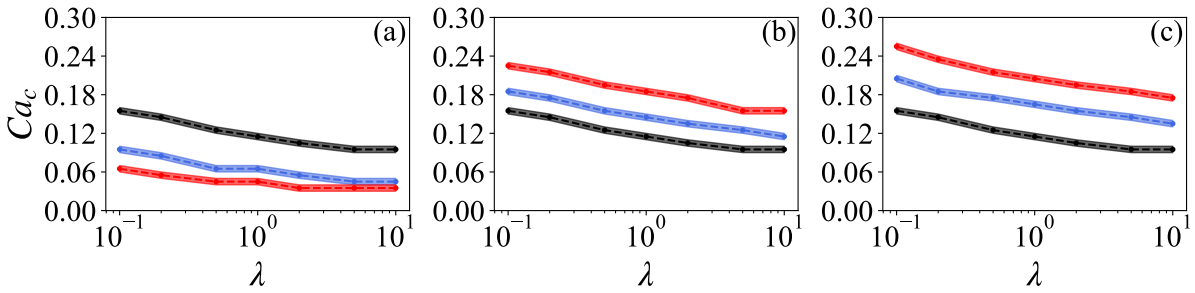

Figure 4.25 – Critical capillary number (Ca_c) as a function of λ when the external magnetic field is applied in (a) x direction, (b) y direction, and (c) z direction. The results are for $Ca_{mag} = 0$ (black circles), $Ca_{mag} = 10$ (blue circles), and $Ca_{mag} = 20$ (red circles). The strip thickness corresponds to the measurement error margin.

and z direction. We see that the external magnetic field can either facilitate or hinder the breakup process of ferrofluid droplets depending on the magnetic field direction, with its effect being proportional to the magnetic field intensity. When the magnetic field is applied in the x direction, the field-induced distortion occurs in the same direction as the flow-induced one; hence, the required flow strength to induce breakup is lower so that Ca_c decreases [see Fig. 4.25(a)]. On the other hand, for magnetic fields applied in the y and z direction, the field-induced forces are perpendicular to the extension direction so the distortion in this direction is hardened due to droplet incompressibility, and consequentially Ca_c increases [see Figs. 4.25(b) and (c)]. The hardening effect is more pronounced when the magnetic field is applied in the z direction rather than in the y direction. This is due to the fact that when the magnetic field is applied in the neutral direction (z direction), the droplet distorts in that direction and the droplet radius in the extension plane (and the effective Ca) decreases so the required Ca_c increases. Overall, the tendency of Ca_c with λ seems to be not affected by the presence of the magnetic field, at least in the observed range of λ and Ca_{mag}. This fact indicates a weak coupling between the effects of λ and $\boldsymbol{H_0}$ on the droplet breakup. In light of this, we can study more precisely the effects of the magnetic field on the droplet breakup for a specific λ, say $\lambda = 1$, and expect the results to be qualitatively similar for the others, at least in some limiting fashion.

Figure 4.26(a) shows Ca_c as a function of Ca_{mag} for $\lambda = 1$ and the external magnetic field applied in each of the flow main directions with Ca_{mag} up to $Ca_{mag} = 40$. The results confirm the overall trends discussed above and enlighten for possible saturation effect. For magnetic fields applied in the x direction, the Ca_c reduction that an additional increase in Ca_{mag} causes is smaller as Ca_{mag} increases. From $Ca_{mag} = 0$ to $Ca_{mag} = 10$, the Ca_c decreases by roughly 0.06, whereas from $Ca_{mag} = 30$ to $Ca_{mag} = 40$, it decreases only by 0.01. A similar attenuation curve occurs when the magnetic field is applied in either y or z direction. This attenuation behavior is believed to be related to the hardening-like response of the field-induced distortion [see Fig. 4.3]. Figure 4.26(b) shows the subcritical deformations in the xy plane ($D_{s;xy}$) and in the xz plane ($D_{s;xz}$) as a function of Ca_c for different Ca_{mag} and external magnetic field direction. The subcritical deformations are

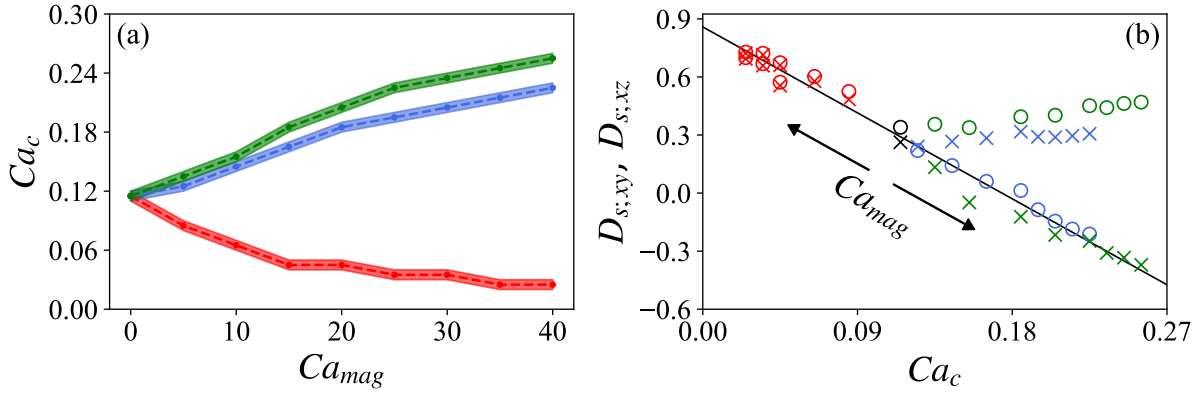

Figure 4.26 – (a) Critical capillary number (Ca_c) as a function of Ca_{mag} for $\lambda = 1$ and different external magnetic field directions, and (b) subcritical droplet deformation in the xy plane ($D_{s;xy}$, circles) and in the xz plane ($D_{s;xz}$, crosses) as a function of Ca_c for different Ca_{mag} and external magnetic field directions. Red strips and symbols refer to the x direction, blue ones to the y direction, and green ones to the z direction. The subcritical deformations for the case without a magnetic field are also shown in (b) (black symbols). In (b), each point corresponds to the (Ca_c, Ca_{mag}) pair in (a). The black arrows show the Ca_{mag} increasing direction. The black line graphs the linear equation $D_s = 0.86 \pm 0.02 + (-4.93 \pm 0.14)Ca_c$.

measured for the last stable cases in which further increment by ΔCa in Ca would lead to breakup. We see that although the magnetic field applied in the x direction decreases Ca_c, it enables the droplet to reach more elongated stable shapes: from $D_{s;xy} = 0.42$ for $Ca_{mag} = 5$ to $D_{s;xy} = 0.75$ for $Ca_{mag} = 40$. Moreover, as Ca_{mag} increases, the influence of the planar extensional flow on the final shape becomes less important in the way that $D_{s;xz}$ approaches $D_{s;xy}$. When applied in the y direction, an opposite trend occurs: as the pair (Ca_{mag}, Ca_c) increases the subcritical configuration becomes more stretched in the y direction than in the x direction, reaching $D_{s;xy} = -0.2$ for $Ca_{mag} = 40$, while $D_{s;xz}$ keeps about the same value as if there were no magnetic field. Here we recall the fact that, in the absence of magnetic fields, the curvature in the xy is flattened at the same time as the curvature in the xy plane, so both have the same importance in the breakup process (see Fig. 4.23). This indicates that the curvature of the droplet surface in the xz can be the main responsible for the droplet breakup when the magnetic field is applied in the y direction with enough intensity. In that case, while the magnetic forces compete with the flow-induced compression in the y direction, the droplet is compressed in the z direction. From above a certain value of distortion in the xz plane, the surface curvature in that plane at the central portion becomes negative, and the breakup process starts regardless of the surface curvature in the xy plane. Figure 4.27 shows the xy and xz plane perspectives of the droplet during the breakup process for $Ca_{mag} = 40$ and $Ca = 0.23$ when the magnetic field is applied in the y direction. We see that indeed the xz cross-section becomes concave at the central portion prior to the xy cross-section (at around $t \approx 18$), and as a consequence, the droplet distortion in the x direction is accelerated, which in turn leads to negative curvatures also in the xy cross-section.

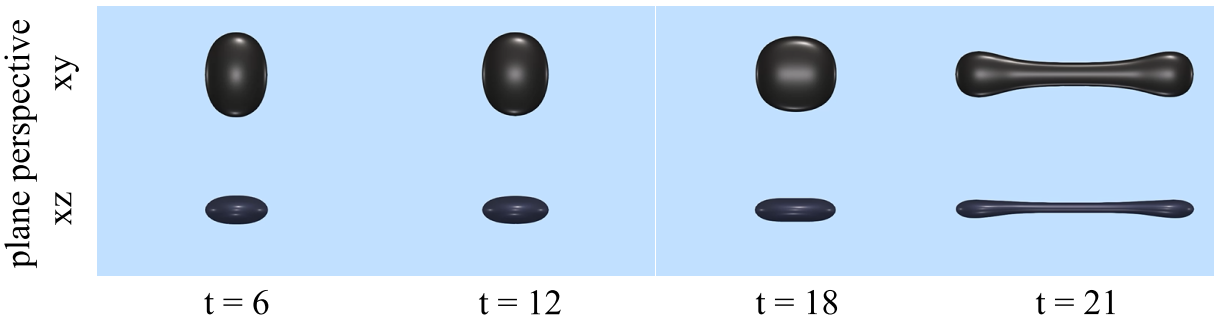

Figure 4.27 – Droplet breakup process for magnetic field applied in the y direction with $Ca_{mag} = 40$ and $Ca = 0.23$ from the xy plane perspective (top figures), and from the xz plane perspective (bottom figures).

We see a similar trend when the magnetic field is applied in the z direction. In this case, however, $D_{s;xy}$ and $D_{s;xz}$ have their trends inverted: as the pair (Ca_{mag}, Ca) increases, $D_{s;xz}$ becomes more pronounced, and $D_{s;xy}$ keeps about the same value as if there were no magnetic field. This suggests that the surface curvature in the xy plane at the central portion is responsible for initiating the breakup process when the magnetic field is applied in the z direction. Figure 4.28 shows the xy and xz plane perspectives of the droplet during the breakup process for $Ca_{mag} = 25$ and $Ca = 0.23$ when the magnetic field is applied in the z direction. This time, the surface becomes concave first in the xy cross-section (at around $t \approx 7.5$).

Despite the odd breakup behavior observed when the magnetic field is applied in the y or z direction for $Ca > Ca_c$, the droplet shapes when Ca is close to Ca_c, i.e., the subcritical shapes, are always ellipsoidal, as shown in Fig. 4.29. A further noteworthy aspect regarding the subcritical deformations is that the $D_{s;xy}$ and $D_{s;xz}$ vary linearly with Ca_c regardless of the applied magnetic field direction and intensity [see Fig. 4.26(b)]. In fact, they seem to obey very similar trends. A slope of $(-4.93 \pm 0.14)Ca_c$ was observed for both $D_{s;xy}$ and $D_{s;xz}$ for the magnetic field applied in the x direction, $D_{s;xy}$ for the magnetic field applied in the y direction, and $D_{s;xz}$ for the magnetic field applied in the z direction. This indicates that Ca_c is tightly linked to the subcritical deformations $D_{s;xy}$ and $D_{s;xz}$ regardless of the magnetic field intensity and direction. In view of that, we could estimate the subcritical deformations of ferrofluid droplets subjected to external magnetic

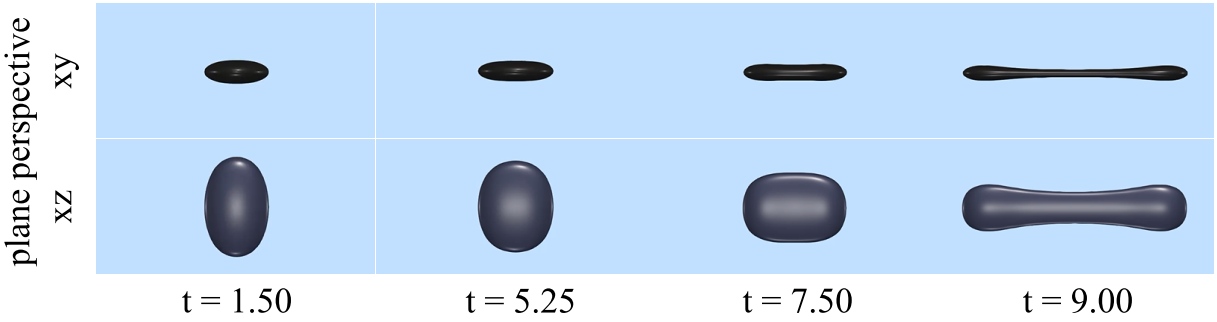

Figure 4.28 – Droplet breakup process for magnetic field applied in the z direction with $Ca_{mag} = 25$ and $Ca = 0.23$ from the xy plane perspective (top figures), and from the xz plane perspective (bottom figures).

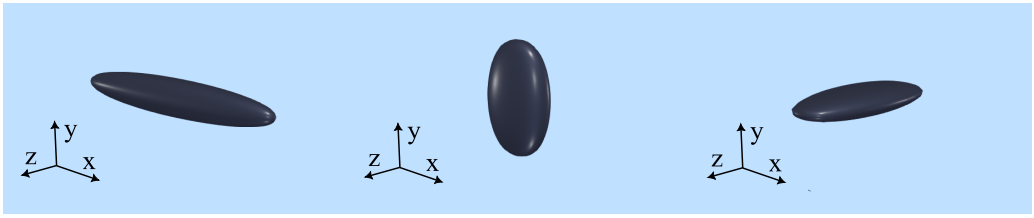

Figure 4.29 – Droplet subcritical shapes for $\lambda = 1$ with $Ca_{mag} = 40$ and the magnetic field applied in the (a) x direction, (b) y direction, and z direction. Ca is equal to 0.02, 0.22, and 0.25, respectively.

fields with certain accuracy by simply knowing the critical capillary number.

It is known that in the absence of magnetic fields, the droplet reaches very long slender shapes without breaking up, in the way that the experimental devices or numerical domains are not able to see the rupture happen. This was the case for our computational domain of size $S_x = 20$ in the extension direction. This was also the case in almost all our numerical experiments with external magnetic fields. Exceptions occur at $Ca_{mag} \geq 35$ when the magnetic field is applied in the z direction. Figure 4.30 shows the breakup of the droplet into two daughter droplets of the same size at $Ca_{mag} = 35$ with $Ca = 0.25$. The intense magnetic field in the z direction tapers the droplet in the xy plane. As a result, the droplet becomes more susceptible to being ripped in smaller elongations. It should be mentioned that although the method accurately predicts the condition the breakup occurs, the post-breakup dynamics [e.g. from $t > 10.5$ in Fig. 4.30] is unphysical due to the finite size of the grid which, in turn, leads to incorrect computation of the curvature and smoothed properties near the point of rupture (a singularity).

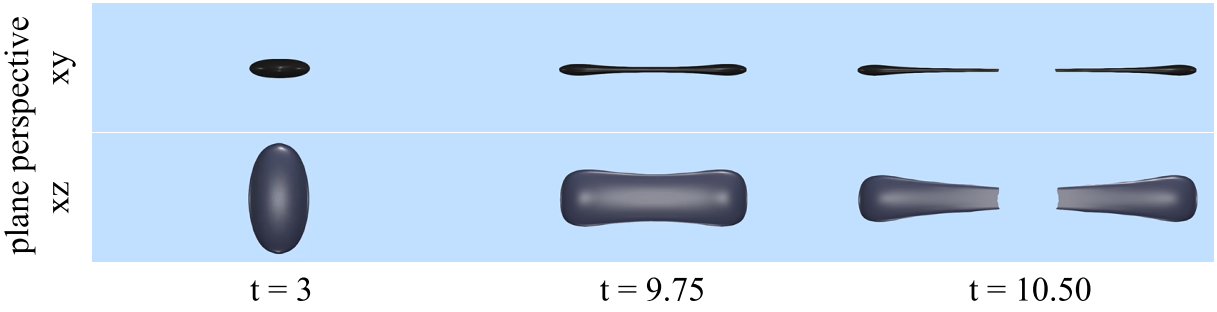

Figure 4.30 – Droplet breakup process for magnetic field applied in the z direction with $Ca_{mag} = 35$ and $Ca = 0.25$ from the xy plane perspective (top figures), and from the xz plane perspective (bottom figures).

5 Concluding remarks

In this work, we have performed three-dimensional numerical simulations of superparamagnetic ferrofluid droplets suspended in a nonmagnetizable viscous fluid under the action of planar extensional flows and uniform external magnetic fields. The full incompressible Navier-Stokes equations for a biphase system in a nondimensional form with the addition of the magnetic term were solved in a Lattice domain using a projection method. The interface problem was treated with the Level-Set method. Validation tests concerning the isolated influence of either the flow or the magnetic field on the droplet's steady shape confirmed the reliability of the numerical model with respect to hydrodynamic, magnetic, and interfacial problems. In our simulations, four distinct directions for the external field were explored: the three main directions of the extensional flow (x, y, and z directions), and the $x = y$ direction.

With regard to the droplet dynamics, we found that the shape of the droplet depends on a tight balance between the viscous, capillary, and magnetic forces at the droplet surface. These forces, in turn, are connected with the external field intensity and direction. While the capillary forces try to keep the spherical shape of the droplet, the flow-induced viscous forces stretch the droplet in the extension direction and compress it in the compression direction, and the field-induced forces tend to stretch the droplet in the external field direction. If the droplet reaches a steady shape, it assumes the form of a general ellipsoid. Under certain conditions, when the external field is in the compression or neutral direction, the droplet assumes an oblate shape. The required Ca_{mag} to obtain such a shape, $Ca^{\star}_{mag}$, varies linearly with Ca, at least in the observed range of parameters.

When the extension rate is sufficiently high, the flow-induced viscous forces lead the system to an unsteady situation in which the droplet is continuously stretched until breakup. The critical capillary number, Ca_c, which marks the transition between steady and breakup situations, is a function of the applied magnetic field intensity and direction. When applied in the extension direction, the external field induces breakup, whereas it prevents the droplet from breaking up when applied in the other two main directions. The way the droplet initiates a continuous elongation also depends on the external field direction. In the absence of external fields, the curvatures of the xy cross-section and that of the xz cross-section change in sign at the same time, even though the deformation in the respective planes are not equal. When the external field is in the x direction, the

curvatures also change in sign at the same time, but now the deformations approach one another as long as Ca_{mag} increases. When the external field is in the y direction, the curvature of the xz cross-section changes in sign before that of the xy cross-section. The deformation in the xz plane is comparable to when there is no magnetic field. When the external field is in the z direction, the opposite occurs: the change in sign happens first in the xy cross-section, and the deformation in that plane is comparable to the case with no magnetic field. If Ca_{mag} is sufficiently high, the subcritical shape major axis lies in the direction of the external field. Despite these interesting variations, the magnetic field does not change significantly the way Ca_c varies with the viscosity ratio between the phases.

In steady situations, the flow pattern within the droplet, induced by the planar extensional flow outside, is characterized by four recirculation regions in the xy cross-section with a symmetric distribution with respect to the x and y direction. This pattern is also present when the magnetic field is applied in one of the flow main directions since the droplet shape remains symmetric with respect to the referential axes. A topological transformation occurs, however, when the magnetic field is applied in the $x = y$ direction. In that case, the droplet's major axis points in a direction between the x and $x = y$ direction. As a result, the viscous forces promote a merger of two vortices, and the flow pattern is characterized by three recirculation regions.

Another important change occurs when the external field is in a direction different from the flow's main directions. The droplet magnetization lies in the direction of the external field when the latter points in one of the flow main directions. This is due to the symmetric distribution of the droplet shape with respect to that direction. On the other hand, when the external field is not in one of the flow main directions the droplet magnetization direction is no longer parallel to the external field due to a nonsymmetric distribution in that direction. The angle between the magnetization and the external field increases with Ca and is a weak function of Ca_{mag}. In all cases, the magnetization intensity is proportional to the droplet elongation in the direction of the external field.

From the continuum perspective, one can regard the single droplet-continuous phase system as an infinitesimal parcel of a dilute ferrofluid emulsion of corresponding volume fraction. The droplet configuration corresponds to a microstructural unit of the emulsion, and the droplet magnetization to the emulsion magnetization. Under the above conclusions of droplet configuration and magnetization can be extrapolated to the corresponding dilute ferrofluid emulsion. It means that the microstructure can be anisotropic when the emulsion is subjected to planar extensional flows. Further, even though the ferrofluid is superparamagnetic, a dilute ferrofluid emulsion is not. By accounting for the droplet stress, using the procedure of Cunha *et al.* (2020), we have also analyzed the effects of external magnetic fields on the extensional rheology of dilute ferrofluid emulsions.

The extensional rheology is tightly connected with the emulsion's microstructure and magnetization. The dispersed phase contribution to the two conventional extensional viscosities is generally affected by the presence of external magnetic fields. When the

external field is applied in the x direction, the planar extensional viscosity increases with the field intensity, characterizing a field-induced viscous hardening effect. The second extensional viscosity, in this case, remains constant. When the field is in the y direction, both coefficients increase with the field intensity. When the field is in the z direction, the planar extensional viscosity remains constant, while the second extensional viscosity decreases with field intensity, characterizing a field-induced viscous softening effect. This reduction is such that for enough field intensity, the droplet contribution to the second extensional viscosity becomes negative, meaning that the presence of the dispersed phase can facilitate the motion in the yz plane. The manner in which these two coefficients vary with the extension rate can be also modified by the presence of magnetic fields. Changing the external field direction from the x to the y direction, the behavior of the emulsion changes from extensional-thickening to extensional-thinning, with respect to the planar extensional viscosity.

When the external field is in the $x = y$ direction, the two extensional viscosities have field-induced viscous-hardening behavior. The mechanical behavior of the emulsion becomes planar-extensional-thickening and second-extensional-thinning. These two coefficients, however, are not enough to fully characterize the extensional rheology in such a case. Field-induced internal torques appear in the system as the emulsion magnetization is not parallel to the external field anymore. The hydrodynamic response to this torque results in a nonsymmetric stress tensor of the bulk emulsion. To account for these unexpected shear components, we define two new material functions: the shear viscosity and the rotational viscosity in the xy plane. These results clarified the fact that for a general external field direction, which can for instance point in a direction that does not lie in any main flow planes, it would be required eight material functions to fully characterize the extensional rheology. The two usual extensional viscosities, and three pairs of shear and rotational viscosity coefficients.

Overall, this work provided a detailed assessment of the magnetization and extensional rheology of dilute ferrofluid emulsions in the presence of external uniform magnetic fields. In addition, it provides an analysis of the dynamics of suspended ferrofluid droplets in planar extensional flows. We believe these findings contribute to the field-assisted control of dilute ferrofluid emulsions properties and individual ferrofluid droplets. Moreover, they evidence the appearance of shear stresses in a material subjected to an extensional motion, which is of valuable importance to the non-Newtonian fluid mechanics field.

Despite the contributions of this work, many questions regarding the behavior of ferrofluid emulsions still remain. How the extensional rheology and magnetization of dilute ferrofluid emulsions are affected if we consider a more general Langevin regime of magnetization? How the viscosity ratio impacts these properties? How does such emulsion respond to permanent oscillatory extensional flows? And if we consider the case of highly concentrated ferrofluid emulsions? These are some of the questions to be addressed in future works.

Bibliography

Abdo, R. F. *et al.* On the rheology and magnetization of dilute magnetic emulsions under small amplitude oscillatory shear. *Journal of Fluid Mechanics*, Cambridge University Press, v. 955, p. A3, 2023. Quoted 2 times on pages 7 and 25.

Abicalil, V. G. e. *et al.* On the magnetization of dilute ferrofluid emulsions in shear flows. *Physics of Fluids*, AIP Publishing LLC, v. 33, n. 5, p. 053313, 2021. Quoted 4 times on pages 6, 11, 16, and 25.

Acrivos, A.; Lo, T. Deformation and breakup of a single slender drop in an extensional flow. *Journal of Fluid Mechanics*, Cambridge University Press, v. 86, n. 4, p. 641–672, 1978. Quoted on page 6.

Afkhami, S. a. *et al.* Deformation of a hydrophobic ferrofluid droplet suspended in a viscous medium under uniform magnetic fields. *Journal of Fluid Mechanics*, Cambridge University Press, v. 663, p. 358–384, 2010. Quoted 6 times on pages xiii, 6, 11, 35, 36, and 43.

Ahmed, N. *et al.* New oil-in-water magnetic emulsion as contrast agent for in vivo magnetic resonance imaging (mri). *Journal of biomedical nanotechnology*, American Scientific Publishers, v. 9, n. 9, p. 1579–1585, 2013. Quoted on page 5.

Badalassi, V. E. *et al.* Computation of multiphase systems with phase field models. *Journal of computational physics*, Elsevier, v. 190, n. 2, p. 371–397, 2003. Quoted on page 24.

Barthes-Biesel, D.; Acrivos, A. Deformation and burst of a liquid droplet freely suspended in a linear shear field. *Journal of Fluid Mechanics*, Cambridge University Press, v. 61, n. 1, p. 1–22, 1973. Quoted on page 6.

Barthés-Biesel, D.; Acrivos, A. The rheology of suspensions and its relation to phenomenological theories for non-newtonian fluids. *International Journal of Multiphase Flow*, Elsevier, v. 1, n. 1, p. 1–24, 1973. Quoted 2 times on pages 3 and 6.

Batchelor, G. The stress system in a suspension of force-free particles. *Journal of fluid mechanics*, Cambridge University Press, v. 41, n. 3, p. 545–570, 1970. Quoted 4 times on pages 3, 7, 16, and 17.

Bentley, B.; Leal, L. G. An experimental investigation of drop deformation and breakup in steady, two-dimensional linear flows. *Journal of Fluid Mechanics*, Cambridge University Press, v. 167, p. 241–283, 1986. Quoted 5 times on pages xvii, 6, 9, 56, and 57.

Biben, T. *et al.* An advected-field approach to the dynamics of fluid interfaces. *Europhysics letters*, IOP Publishing, v. 63, n. 4, p. 623, 2003. Quoted 3 times on pages xvii, 56, and 57.

Bibette, J. Monodisperse ferrofluid emulsions. *Journal of magnetism and magnetic materials*, Elsevier, v. 122, n. 1-3, p. 37–41, 1993. Quoted on page 4.

Capobianchi, P. *et al.* Deformation of a ferrofluid droplet in a simple shear flow under the effect of a constant magnetic field. *Computers & Fluids*, Elsevier, v. 173, p. 313–323, 2018. Quoted on page 6.

Capobianchi, P. *et al.* Shear rheology of a dilute emulsion of ferrofluid droplets dispersed in a nonmagnetizable carrier fluid under the influence of a uniform magnetic field. *Journal of Rheology*, The Society of Rheology, v. 65, n. 5, p. 925–941, 2021. Quoted 4 times on pages 6, 7, 11, and 25.

Cunha, L. *et al.* Effects of external magnetic fields on the rheology and magnetization of dilute emulsions of ferrofluid droplets in shear flows. *Physics of Fluids*, AIP Publishing LLC, v. 32, n. 7, p. 073306, 2020. Quoted 7 times on pages 4, 6, 7, 11, 16, 25, and 63.

Cunha, L. H. *et al.* Field-induced control of ferrofluid emulsion rheology and droplet break-up in shear flows. *Physics of Fluids*, AIP Publishing LLC, v. 30, n. 12, p. 122110, 2018. Quoted 2 times on pages 6 and 7.

Eshgarf, H. *et al.* An overview on properties and applications of magnetorheological fluids: Dampers, batteries, valves and brakes. *Journal of Energy Storage*, Elsevier, v. 50, p. 104648, 2022. Quoted on page 5.

Flament, C. *et al.* Measurements of ferrofluid surface tension in confined geometry. *Physical Review E*, APS, v. 53, n. 5, p. 4801, 1996. Quoted 4 times on pages xii, 4, 6, and 11.

Gottlieb, S. *et al. Strong stability preserving Runge-Kutta and multistep time discretizations.* : World Scientific, 2011. Quoted on page 30.

Grace, H. P. Dispersion phenomena in high viscosity immiscible fluid systems and application of static mixers as dispersion devices in such systems. *Chemical Engineering Communications*, Taylor & Francis, v. 14, n. 3-6, p. 225–277, 1982. Quoted 5 times on pages xvii, 2, 6, 56, and 57.

Guilherme, A. *et al.* Ferrofluid droplets in planar extensional flows: Droplet shape and magnetization reveal novel rheological signatures of ferrofluid emulsions. *Physical Review Fluids*, APS, v. 8, n. 6, p. 063601, 2023. Quoted 26 times on pages xii, xiii, xiv, xv, xvi, xvii, 8, 10, 17, 35, 36, 37, 38, 39, 40, 41, 42, 43, 46, 47, 49, 50, 51, 52, 53, and 55.

Hassan, M. R. *et al.* Deformation of a ferrofluid droplet in simple shear flows under uniform magnetic fields. *Physics of Fluids*, AIP Publishing LLC, v. 30, n. 9, p. 092002, 2018. Quoted 2 times on pages 6 and 11.

Hsu, A. S.; Leal, L. G. Deformation of a viscoelastic drop in planar extensional flows of a newtonian fluid. *Journal of non-newtonian fluid mechanics*, Elsevier, v. 160, n. 2-3, p. 176–180, 2009. Quoted 5 times on pages xiii, 6, 9, 34, and 35.

Ishida, S.; Matsunaga, D. Rheology of a dilute ferrofluid droplet suspension in shear flow: Viscosity and normal stress differences. *Physical Review Fluids*, APS, v. 5, n. 12, p. 123603, 2020. Quoted 4 times on pages 6, 7, 11, and 25.

Ishida, S. *et al.* Field-controlling patterns of sheared ferrofluid droplets. *Physics of Fluids*, AIP Publishing LLC, v. 34, n. 6, p. 063309, 2022. Quoted 2 times on pages 7 and 25.

Jesus, W. C. *et al.* Deformation of a sheared magnetic droplet in a viscous fluid. *Commun. Comput. Phys*, v. 24, n. 2, p. 332–355, 2018. Quoted on page 6.

Jiang, G.-S.; Peng, D. Weighted eno schemes for hamilton–jacobi equations. *SIAM Journal on Scientific computing*, SIAM, v. 21, n. 6, p. 2126–2143, 2000. Quoted on page 30.

Kennedy, M. R. *et al.* Motion and deformation of liquid drops, and the rheology of dilute emulsions in simple shear flow. *Computers & fluids*, Elsevier, v. 23, n. 2, p. 251–278, 1994. Quoted 2 times on pages 6 and 7.

Kim, J.; Moin, P. Application of a fractional-step method to incompressible navier-stokes equations. *Journal of computational physics*, Elsevier, v. 59, n. 2, p. 308–323, 1985. Quoted on page 23.

Kim, S.; Karrila, S. J. *Microhydrodynamics: principles and selected applications.* : Courier Corporation, 2013. Quoted on page 15.

Kúdelčík, J. *et al.* Measurement of complex permittivity of oil-based ferrofluid in magnetic field. *Acta Physica Polonica A*, v. 131, n. 4, p. 931–933, 2017. Quoted on page 14.

Landau, L. D.; Lifshitz, E. M. *Fluid Mechanics: Landau and Lifshitz: Course of Theoretical Physics, Volume 6.* : Elsevier, 2013. v. 6. Quoted 2 times on pages 12 and 15.

Li, X.; Sarkar, K. Numerical investigation of the rheology of a dilute emulsion of drops in an oscillating extensional flow. *Journal of non-newtonian fluid mechanics*, Elsevier, v. 128, n. 2-3, p. 71–82, 2005. Quoted 2 times on pages 6 and 7.

Liu, Q. *et al.* Optimization of deformable magnetic-sensitive hydrogel-based targeting system in suspension fluid for site-specific drug delivery. *Molecular pharmaceutics*, ACS Publications, v. 15, n. 10, p. 4632–4642, 2018. Quoted on page 5.

Liu, X. *et al.* Electric field mediated droplet spheroidizing in an extensional flow. *Physics of Fluids*, AIP Publishing LLC, v. 33, n. 5, p. 052116, 2021. Quoted on page 40.

Loewenberg, M.; Hinch, E. Numerical simulation of a concentrated emulsion in shear flow. *Journal of Fluid Mechanics*, Cambridge University Press, v. 321, p. 395–419, 1996. Quoted 2 times on pages 6 and 25.

Majidi, M. *et al.* Magnetic field-induced control of a compound ferrofluid droplet deformation and breakup in shear flow using a hybrid lattice boltzmann-finite difference method. *International Journal of Multiphase Flow*, Elsevier, v. 146, p. 103846, 2022. Quoted on page 7.

Mandal, S. *et al.* Drop deformation and emulsion rheology under the combined influence of uniform electric field and linear flow. *Journal of Fluid Mechanics*, Cambridge University Press, v. 841, p. 408–433, 2018. Quoted on page 7.

Oldroyd, J. The elastic and viscous properties of emulsions and suspensions. *Proceedings of the Royal Society of London. Series A. Mathematical and Physical Sciences*, The Royal Society London, v. 218, n. 1132, p. 122–132, 1953. Quoted on page 6.

Oliveira, T.; Cunha, F. A theoretical description of a dilute emulsion of very viscous drops undergoing unsteady simple shear. *Journal of fluids engineering*, American Society of Mechanical Engineers Digital Collection, v. 133, n. 10, 2011. Quoted on page 25.

Oliveira, T.; Cunha, F. Emulsion rheology for steady and oscillatory shear flows at moderate and high viscosity ratio. *Rheologica Acta*, Springer, v. 54, n. 11-12, p. 951–971, 2015. Quoted on page 6.

Osher, S.; Fedkiw, R. P. *Level set methods and dynamic implicit surfaces.* : Springer New York, 2006. v. 153. Quoted 5 times on pages 23, 27, 28, 29, and 30.

Park, J. M. *et al.* A taylor analogy model for droplet dynamics in planar extensional flow. *Chemical Engineering Science*, Elsevier, v. 204, p. 27–34, 2019. Quoted 4 times on pages xiii, 6, 9, and 35.

Patankar, S. *Numerical heat transfer and fluid flow.* : Taylor & Francis, 2018. Quoted on page 23.

Petrie, C. J. Extensional viscosity: A critical discussion. *Journal of Non-Newtonian Fluid Mechanics*, Elsevier, v. 137, n. 1-3, p. 15–23, 2006. Quoted 2 times on pages 3 and 17.

Rosensweig, R. E. *Ferrohydrodynamics.* : Courier Corporation, 2013. Quoted 2 times on pages 4 and 12.

Rumscheidt, F.; Mason, S. Xii. deformation and burst of fluid drops in shear and hyperbolic flow. *J. Colloid Sci*, v. 16, p. 238–261, 1961. Quoted on page 56.

Saad, Y. *Iterative methods for sparse linear systems.* : SIAM, 2003. Quoted on page 31.

Schowalter, W. *et al.* Rheological behavior of a dilute emulsion. *Journal of colloid and interface science*, Elsevier, v. 26, n. 2, p. 152–160, 1968. Quoted 2 times on pages 3 and 6.

Shliomis, M. I. Ferrohydrodynamics: Testing a third magnetization equation. *Physical Review E*, APS, v. 64, n. 6, p. 060501, 2001. Quoted on page 12.

Sussman, M.; Fatemi, E. An efficient, interface-preserving level set redistancing algorithm and its application to interfacial incompressible fluid flow. *SIAM Journal on scientific computing*, SIAM, v. 20, n. 4, p. 1165–1191, 1999. Quoted on page 29.

Sussman, M. *et al.* A level set approach for computing solutions to incompressible two-phase flow. *Journal of Computational physics*, Elsevier, v. 114, n. 1, p. 146–159, 1994. Quoted 3 times on pages 25, 26, and 28.

Taylor, G. I. The viscosity of a fluid containing small drops of another fluid. *Proceedings of the Royal Society of London. Series A, Containing Papers of a Mathematical and Physical Character*, The Royal Society London, v. 138, n. 834, p. 41–48, 1932. Quoted on page 5.

Taylor, G. I. The formation of emulsions in definable fields of flow. *Proceedings of the Royal Society of London. Series A, containing papers of a mathematical and physical character*, The Royal Society London, v. 146, n. 858, p. 501–523, 1934. Quoted 5 times on pages 3, 5, 18, 35, and 56.

Torres-Díaz, I.; Rinaldi, C. Recent progress in ferrofluids research: novel applications of magnetically controllable and tunable fluids. *Soft matter*, Royal Society of Chemistry, v. 10, n. 43, p. 8584–8602, 2014. Quoted on page 5.

Yang, R.-J. *et al.* Micro-magnetofluidics in microfluidic systems: A review. *Sensors and Actuators B: Chemical*, Elsevier, v. 224, p. 1–15, 2016. Quoted on page 5.

Yang, Y. *et al.* Analysis on influence of the magnetorheological fluid microstructure on the mechanical properties of magnetorheological dampers. *Smart Materials and Structures*, IOP Publishing, v. 29, n. 11, p. 115025, 2020. Quoted on page 5.

Yerin, C.; Belykh, S. Magnetic emulsions as prospective magneto-optical media. *IEEE Transactions on Magnetics*, IEEE, v. 58, n. 2, p. 1–4, 2021. Quoted on page 5.

Zhao, S. *et al.* Shape-reconfigurable ferrofluids. *Nano Letters*, ACS Publications, v. 22, n. 13, p. 5538–5543, 2022. Quoted on page 41.

Zhu, T. *et al.* Magnetic-field-assisted fabrication and manipulation of nonspherical polymer particles in ferrofluid-based droplet microfluidics. *Langmuir*, ACS Publications, v. 31, n. 31, p. 8531–8534, 2015. Quoted on page 41.